MODELLING AND ANALYSIS OF HAPTIC MECHANICAL SYSTEMS

Sara Shayan Amin

Department of Mechanical Engineering
McGill University, Montréal

August 2014

A Thesis submitted to the Faculty of Graduate Studies and Research
in partial fulfilment of the requirements for the degree of
Doctor of Philosophy

Abstract

A haptic device is usually a controlled mechanical system. By using such a device a human operator can interact with a virtual environment. In kinesthetic haptic devices, the virtual interaction forces can be determined via the virtual environment model and generated via the actuation of the device. Main problems in haptics come from non-idealities stemming from virtual force representations and the instrumentation of the haptic device. In case of impedance-type haptic devices in applications where rendering a stiff virtual environment is required, these non-idealities can lead to undesired dynamic behaviour and instability problems. The dynamic behaviour of the haptic device can significantly influence the quality and nature of haptic rendering. This dynamics primarily depends on the mechanical properties of the device. Therefore, it is important to understand the effect of the mechanical system properties on haptic dynamics and the virtual contact behaviour.

In this thesis, we outline a systematic framework for the development of parametric mechanical models for the analysis of haptic systems. In this framework, we introduce and discuss models starting from general principles of mechanics applied to haptic devices. Such devices can be seen as articulated mechanical systems possessing several active and passive degrees of freedom. This framework also makes it possible to generate simplified models that allow for analytical investigation. The effective parameters of these simplified models are directly derived and related to the mechanical system parameters of the haptic device and expressed as functions of those parameters. The considerations and effects of structural flexibility are also discussed as an

important element of the framework. Structural flexibility may seriously limit haptic performance and impedance range, and can lead to high-frequency oscillations.

Rendering a virtual wall is used as a sample case to illustrate the concepts. For this case and using the proposed models, closed-form stability conditions are developed in this thesis for a broad range of virtual stiffness and damping values, and the results are compared with those reported in the haptic literature. The results are validated and illustrated experimentally using a five-bar linkage based haptic device. In this analysis, effects of human operator on dynamic behaviour of haptic systems are also investigated.

For further analysis, closed-loop performance measures are developed in terms of the mechanical parameters of the haptic system. These indices represent the range of renderable virtual environment parameters, and the fidelity of the virtual interaction forces. The parametric performance measures are compared with those of traditionally used in design of robotic mechanisms and their properties are discussed for application in haptics.

Résumé

Un dispositif haptique est généralement un système mécanique contrôlé. En utilisant un tel dispositif, l'opérateur humain peut entrer en interaction avec un environnement virtuel. Dans les dispositifs haptiques kinesthésique, les forces d'interactions virtuelles peuvent être déterminées par l'intermédiaire d'un modèle d'environnement virtuel et générées via l'actionnement du dispositif. Les principaux problèmes des systèmes haptiques sont des non-idéalités provenant des représentations de la force virtuelle et l'instrumentation du dispositif haptique. Dans des dispositifs haptique de type impédance et dans les applications où le rendu d'un environnement virtuel rigide est nécessaire, ces non-idéalités peuvent provoquer un comportement dynamique et des problèmes indésirables d'instabilité. Le comportement dynamique d'un dispositif haptique peut avoir une influence significative sur la qualité et la nature du rendu haptique. Cette dynamique dépend principalement des propriétés mécaniques du dispositif. Par conséquent, il est important de comprendre les effets des propriétés mécaniques du système sur la dynamique du dispositif haptique et sur le comportement du contact virtuel.

Dans cette thèse, nous présentons un cadre de travail systématique pour l'élaboration de modèles mécaniques paramétriques pour l'analyse des systèmes haptiques. Dans ce cadre, nous présentons et discutons les modèles en débutant par la présentation des principes généraux de la mécanique appliquée à des dispositifs haptiques. De tels dispositifs peuvent être considérés comme des systèmes mécaniques articulés possédant plusieurs degrés de liberté actifs et passifs. Ce cadre de travail permet également de

générer des modèles simplifiés qui permettent des études analytiques. Les paramètres effectifs de ces modèles simplifiés sont directement dérivés et liés aux paramètres du système mécanique du dispositif haptique et exprimés en fonction de ces paramètres. Les effets de la flexibilité structurelle sont également discutés comme un élément important de ce cadre. La flexibilité structurelle peut sérieusement limiter la performance haptique et la gamme d'impédance, et peut aussi entraner des oscillations de hautes fréquences.

Le rendu d'un mur virtuel est utilisé comme un exemple pour illustrer les concepts. Dans cette thèse, les modèles proposés sont utilisés pour déterminer les conditions de stabilité en forme fermée pour ce cas pour une vaste gamme de rigidité virtuelle et de valeurs d'amortissement. Par la suite les résultats sont comparés à ceux rapportés dans la littérature. Les résultats sont validés et illustrés expérimentalement en utilisant une liaison mécanique à cinq barres à base de dispositif haptique. Dans cette analyse, les effets de l'opérateur humain sur le comportement dynamique des systèmes haptiques sont également étudiés.

Pour une analyse plus en profondeur, des mesures de performance en boucle fermée sont élaborées en fonction des paramètres mécaniques du système haptique. Ces indices représentent la gamme des paramètres d'environnement virtuel réalisables, et la fidélité des forces d'interaction virtuelle. Les mesures de rendement paramétriques sont comparées à celles traditionnellement utilisées dans la conception de mécanismes robotiques et leurs propriétés sont discutées dans les applications haptiques.

Acknowledgements

I would like to express my gratitude to my supervisor, Prof. József Kövecses, for his support and guidance. This thesis would not have been completed without his supports and motivations. I am grateful that he believed in me since the beginning. I appreciate his patience, kindness and being understanding in all the situations.

I also would like to thank Dr. László Kovács for his help and support. I learned a lot from him during our long discussions, even sometimes from long distance.

I would like to thank my friends Nona Nobari, Bahareh Ghotbi, Danial Alizadeh, and Afshin Taghvaeepour, who made these years more enjoyable for me. I also would like to thank Elham Khorshidi, Roohollah Farahani, Soheila Mahdavi and Hadi Mahdavi, who brought lots of excitement and happiness to my life in Canada.

More important, I would like to thank my husband, Hamid Dalir, who was always beside me during this journey. His love and support was always with me.

And at the end, I would like to express my deepest gratitude to my family; my parents for their love and supports, and for thinking of me and praying for me every single day in my absence during these years, my sister Samira and my brother Siamak.

ACKNOWLEDGEMENTS

Claims of Originality

- Development of parametric mechanical models as a tool for the analysis and performance evaluation of the haptic systems.
- Consideration of structural flexibility and its effect on virtual contact dynamic behaviour.
- Validation of the proposed models via experimental analysis, and investigating the applicability of these models in different operational conditions.
- Analysis of the effects of the human operator on the dynamic behaviour of haptic systems.
- Analysis of the effects of time-delay and filtering on the dynamic behaviour of haptic systems.
- Development of closed-form stability conditions for a broad range of virtual environment parameters as functions of mechanical and structural properties of the system.
- Development of quantitative performance measures to characterize the effects of system parameters on the haptic stability and performance.

TABLE OF CONTENTS

LIST OF FIGURES

LIST OF TABLES

CHAPTER 1

Introduction

1.1 Literature Review

Haptics or haptic technology refers to the technology of transmitting the sense of touch from a remote or virtual environment by applying force or vibration to the human user. Haptic technology has many areas of application. One of the main applications is in virtual reality systems, adding the sense of touch to previously visual-only technologies. Another major application of haptics is in medical simulation for training in minimally invasive procedures such as laparoscopy (Panait et al., 2009) and interventional radiology (Ilic et al., 2005) as well as for performing remote surgery.

(a) Haptic Wand (b) Phantom Omni (c) Phantom Premium

FIGURE 1.1. Impedance-type haptic interfaces

A haptic interface or haptic device is usually a controlled mechanical system by which the communication between the human user and the remote or simulated virtual environment is possible. A haptic interface usually includes a force feedback device using which a human operator can experience tactile or kinesthetic sensation. Tactile feedback refers to the sensation of deformations of the skin (Okamura et al., 1998), allowing users to feel the texture of surfaces. A popular method to convey tactile sensation is by applying vibrations feedback (Minsky and Lederman, 1996). Kinesthetic feedback on the other hand directly transmits forces to the human operator and refers to the internal sensing of forces and displacements inside muscles, tendons, and joints (Siciliano and Khatib, 2008). Kinesthetic feedback can be provided via two classes of haptic devices, admittance-type or impedance-type interfaces. An admittance-type interface generates motion in response to the force input from the human operator, while an impedance-type device provides force feedback to the user in relation to the imposed motion. Admittance-type interfaces are generally heavy, stiff and strong devices, such as industrial robots, which can render rigid contact with a virtual environment. Example of these devices can be a high-performance haptic device called HapticMaster (van der Linde et al., 2002). On the other hand, impedance-type haptic interfaces are usually back-drivable and have low inertia and friction. Samples of the commonly used impedance-type haptic devices are shown in Fig. 1.1, which includes Phantom Premium (Massie and Salisbury, 1994), Phantom Omni and Haptic Wand. This class of interfaces are dominant in various haptic applications for variety of reasons, such as cost.

1.1.1 Performance Analysis. An interface device in general allows a human user to interact with computer or other electronic information system. Haptic interfaces have a distinguishing feature among other interface devices by being bi-directional in terms of information flow, while other interfaces, such as joysticks, are uni-directional. Haptic interfaces track the input of the human user and provide force feedback to the user accordingly. Due to this difference, performance evaluation

and comparison of these devices become more difficult and remains an active area of research.

There are several performance requirements for haptic applications which indicate the quality of haptic rendering of virtual environments. Impedance range, transparency and fidelity are among requirements that are usually referred to in the literature. Impedance range refers to the capability of a haptic interface of rendering a range of virtual impedances (Colgate and Brown, 1994), and transparency is associated with the quality of the transmitted feedback to the human user (Moix, 2005; McJunkin, 2007). An ideal transparent haptic interface is a device in which the transmitted feedback force from a virtual environment to an operator is not influenced by the physics of the device. Fidelity is another important haptic requirement, which is associated with the closeness of the sense of the simulated environment to the corresponding physical environment intended to be rendered.

In admittance-type haptic devices, the impedance range is limited by the structural properties of the device only, and they are capable of rendering high impedance (stiff) contact with virtual environments. However, due to their typically high inertia, achieving transparency is a challenging control task. Compared to admittance-type interfaces, impedance-type devices can provide good transparency, but serious limitation can arise in their performance when rendering a rigid contact with a virtual environment.

Several performance measures are listed in (Hayward and Astley, 1996) in relation to haptic applications. This includes traditional robotics performance measures, such as dexterity and manipulability measurements, as well as a set of more specific performance measures, such as peak force and acceleration. Generally the quantitative performance measures in the literature can be categorized in three groups. The first group considers the "uncontrolled system", which refers to pure mechanism and structural design. This group includes traditional robotic performance indices such as indices for dexterity, workspace, singularity, or structural properties of the device, which are discussed in (Hayward et al., 1994). An example of such performance

measures in haptic applications can be the isotropy index which corresponds to the entire workspace proposed in (Stocco et al., 1998), which has been used for the kinematic design of a haptic device for optimum performance in terms of semidextrous workspaces and static force capabilities (Stocco, 2000).

The second group includes the evaluation of the "powered system". This refers to actuation and sensing capabilities of the system. An example of this group is the a performance measure for force optimization of commercially available electric motors for haptic applications proposed in (Salcudean and Stocco, 2000). The third category includes more specific measures evaluating the "closed-loop" performance of haptic systems, incorporating both the effects of the human operator and the virtual environment. These measurements include the measurement of impedance range (Colgate and Brown, 1994; Weir et al., 2008), which is closely related to the stability properties of a given haptic interface.

Most of the proposed work on performance analysis of haptic devices in the literature consists of the evaluation of particular haptic devices (Faulring et al., 2006; Gassert et al., 2006; Peer and Buss, 2008; Samur et al., 2011) , or relates to experimental performance evaluation (Ellis et al., 1996; Ueberle and Buss, 2002; Ueberle, 2006; Salisbury et al., 2011). However, development of closed-loop performance measures as functions of system parameters can be advantageous in haptic system analysis.

1.1.2 An Important Problem in Haptics. A typical representation of haptic interfacing using an impedance-type kinesthetic haptic device is shown in Fig. 1.2. As illustrated in this figure, human operator is in interaction with a virtual environment via manipulating a haptic device. Such haptic devices are generally articulated mechanical systems. These can be modelled as multibody systems, and the physical system model can also be expanded to include the human operator.

Main problems in haptics come from the interaction force between the human user and the virtual environment. If we replaced the virtual environment with its physical counterpart then these interaction forces would normally be developed via physical

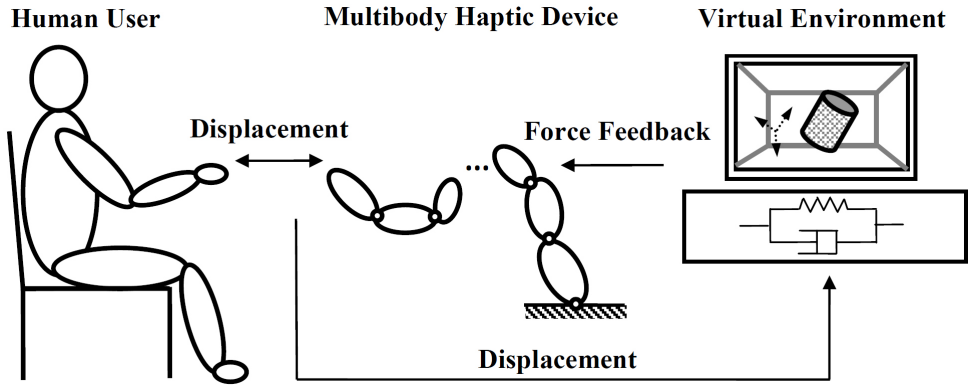

FIGURE 1.2. Schematic of the haptic interaction

contact and the model of the system would take the usual form of a constrained mechanical system. However, in a haptic multibody system the virtual interaction forces are determined via the virtual environment model and generated via the actuation of the haptic device. For instance, in case of using impedance-type haptic devices equipped with encoders for position measurement, the virtual environment reactions are generated via rendering virtual impedances. This is in principle equivalent with the penalty method to represent the effects of interaction forces.

Key problems in such haptic multibody systems stem from non-idealities in the system. These non-idealities are included in the virtual force representations, such as time discretization; as well as the non-ideal effects coming from the instrumentation of the haptic device, such as quantization and the lack of explicit velocity measurement (Janabi-Sharifi et al., 2000; Diolaiti et al., 2006). These are manifested in passivity violations (Colgate and Schenkel, 1997; Adams and Hannaford, 1999) that can lead to undesired dynamic behaviour and instability problems, particularly in impedance-type haptic devices interacting with virtual environments with high impedance. This has been a core problem in haptics in general.

This problem has been looked at from several different aspects. A main line of approach intends to resolve the problems purely at the control, i.e., software, level to restore passivity and increase the impedance range via the introduction of virtual dissipative elements. For example, time-domain passivity control (Hannaford and

Ryu, 2002) is a main example of this group of approaches. For the practical implementation of such control algorithms, velocity estimation from discrete and quantized position data is the bottleneck point (Janabi-Sharifi et al., 2000). Another group of approaches introduce physical dissipative elements to deal with the unwanted dynamics in haptic rendering. These include for example, increasing the physical dissipation via frequency dependent electrical damping (Mehling et al., 2005), or programmable physical damping realized by electromagnetic brakes (Gosline et al., 2006; Tognetti and Book, 2006).

Another approach, which is a main topic in this thesis, is to investigate how the dynamics of the haptic mechanical system influences the core virtual contact dynamics, and implement changes via mechanical design. The dynamic behaviour of haptic devices can fundamentally influence the quality of the feeling of the virtual contact and generally the safety and usability of haptic rendering. By analyzing these effects, an optimum design may be proposed for a device before it is built for a desired task. In addition, further parametric analysis can make it possible to assess the importance of mechanical and control parameters.

1.1.3 Dynamic Analysis of Haptic Systems. In most haptic system analyses, the physical part of the haptic device is modelled as a single degree of freedom (DoF) mass-damper system with viscous damping. Passivity analysis of such models leads to the determination of stability regions, ensuring that energy generated due to the digital realization of the virtual environment is always dominated by the intrinsic dissipation of the device (Colgate and Schenkel, 1997). However, it is shown in (Diolaiti et al., 2006) that in practice most commercially available haptic devices have a larger impedance range than that of dictated by the passivity condition. It was also observed that the dissipation in these devices is dominated by Coulomb friction at low velocities. To take this into consideration, an energetic dissipativity condition is given in (Diolaiti et al., 2006), which can take into consideration both damping and friction. However, this condition limits the maximum (initial) velocity of the system. This is a

strong limitation for haptic applications, since the initial velocity depends on the interaction with the user. Another group of energy-based approaches are motivated by electrical network models, which include a two-port network representation of haptic devices proposed in (Adams and Hannaford, 1999, 2002; Tognetti, 2005). This representation makes it possible to directly apply Raisbeck's passivity criterion and/or the less conservative Llewellyn unconditional stability criterion (Haykin, 1970) to haptic models that describe interactions corresponding to a single direction. Raisbeck's passivity condition corresponds to the positive definiteness of the imittance matrix defined by the relation between the input/output power variables. These variables are the forces and velocities applied by the human operator and transmitted from the simulated virtual environment. An advantage of the two-port network representation is that it provides passivity or unconditional stability based control design for a larger class of systems (including flexible, and multi-DoF models) compared to the single-DoF point-mass model investigated in (Colgate and Schenkel, 1997; Diolaiti et al., 2006). An extension to multiple-port networks is provided in (Mendez and Tavakoli, 2010). By using the two-port network representation of haptic interactions, the stability of the system can be guaranteed for any level of passive human operator and virtual environment impedance by the Llewellyn's stability criterion (Adams et al., 1998). This is achieved by the addition of a virtual coupling network with sufficiently low virtual stiffness and damping.

Internal dissipation and human models are uncertain elements in the analysis of haptic rendering. The practical implementation of energy-based approaches is independent of the uncertain human impedance and the mechanical properties of the system (Hannaford and Ryu, 2002). This is beneficial because the results do not rely on the uncertain system parameters, but the drawback is that they cannot reflect the effect of mechanical design on the virtual contact dynamics. Also these approaches typically result in conservative stability conditions (Hulin et al., 2008). This conservativeness can cause performance limitations, when high impedance virtual environment is required.

The focus of this thesis is on impedance-type haptic devices in contact with stiff virtual environments, where stability of virtual contact dynamics is of great importance. The closed-loop performance of haptic interfaces, which includes the effect of digital control realization, can be quantified via stability conditions (Hayward and Astley, 1996).

The stability properties of the single-DoF point-mass model have been analyzed from various aspects. A point-mass model connected to a viscous damping element is analyzed in (Gil et al., 2004), and a linearized stability condition is proposed which is valid for low virtual damping values. This condition was earlier achieved empirically in (Minsky et al., 1990) as a stability condition for virtual wall implementation. A mass-spring-damper model of a haptic device is analyzed numerically in (Colgate and Schenkel, 1997), where the spring element was used to model the worst case contact with the human operator. The physical stiffness was selected such that the undamped natural frequency matched the Nyquist frequency and the corresponding stable domain is termed as the domain of spring stability. The same model with arbitrary stiffness is used in (Hulin et al., 2008) for further analysis of the human operator effects, and a comparison of the results with passivity and spring stability is provided.

In practice, instability may occur before reaching the stability limits obtained by the simple point-mass model. This is because of the simple representation of the haptic interaction (Hayward and Astley, 1996). Methods for the analysis and performance evaluation of multi-DoF haptic systems and related models represent an open area of research.

1.1.4 Digital Realization. In dynamic analysis of haptic systems, digital realization of virtual environment is similar to mechanical system with digital controller. In case of high sampling frequency and where the end-effector is in contact with soft environments, low effective stiffness and high effective mass, the virtual interaction can be approximated as continuous. If the environment is very stiff, then the digital effects will have significant effect.

Dynamics of a digitally controlled system can be very different from that of an analog system (Kuo, 1981). For instant, stability of a single-DoF mechanical system with a continuous time PD controller, where P and D correspond to the proportional and derivative control gains respectively, results in an asymptotically stable behaviour for any $P > 0$ and $D > 0$ values. However, a digital PD controller and the same mechanical system, shows a completely different behaviour. In this case, the structure of the stability domain in the parameter space is more complex, which requires more detailed analysis. The stability and performance characteristics of a digital PD controller can be determined by the intricate combinations of the control gains, the sampling frequency and the mechanical parameters of the system (Stepan et al., 1990; Stepan, 2001).

The digital PD controller in motion control in robotics is mathematically similar to a haptic device in contact with a commonly used Kelvin-Voigt model based virtual wall. However, there is a fundamental difference. In motion control, the gains can be tuned to obtain a required performance, while in haptics they carry physical meaning, where P and D serve as stiffness and damping properties of a rendered virtual wall. Another important difference is the presence of human in haptic systems. In such a case, for stable rendering of a specific virtual wall, i.e., fixed values of P and D, tuning of the mechanical design properties can be of interest.

1.1.5 Structural Flexibility. Beside the inertial properties of a haptic device and the impedance of the human operator (Colgate and Schenkel, 1997; Hulin et al., 2008), structural flexibility can play an important role in the dynamic behaviour. In impedance-type haptic devices the minimization of inertia, and consequently the effective mass in the rendered direction, can lead to a design where structural flexibility becomes an essential element to consider. Structural flexibility can generally appear in two different ways in robotic and haptic systems: in a localized form such as the flexibility originating from the mechanical elements of the joints, and as distributed flexibility if the structural properties of the main links need to be considered. Often, localized joint flexibility is dominant. For example, cable-driven, capstan-based

joints are quite common in haptic applications. Such design solutions have several advantages, e.g., higher transmission ratio and back-drivability. On the other hand, such joints can also introduce significant, localized sources of structural flexibility.

In general, flexibility is rarely taken into consideration in haptic system analysis and design. A possible explanation for this is that in the range of relatively low virtual impedances, permitted by conservative stability results, the structural vibration modes cannot be excited during haptic interactions. Secondly, the applied low-pass filters may suppress not just the measurement noise, but also the high-frequency structural vibrations. This will also be further discussed.

There are few papers that consider the effect of structural flexibility in haptics, e.g., (Adams et al., 1998) and (Gil and Diaz, 2010). In these approaches, lumped-parameter models have been employed, where the parameter identification is based on the measured frequency response of the system. In (Adams et al., 1998), a two-port network representation is used to investigate the behaviour of haptic systems with structural flexibility. In (Gil and Diaz, 2010) the influence of structural vibration modes on the stability of different haptic devices, PHANToM (Massie and Salisbury, 1994) and LHIfAM (Borro et al., 2004), is investigated, where the effects of a single actuator was considered. The analysis revealed that for some devices, like PHANToM, the worst-case scenario could be effectively described by the simple rigid body model of the device, while, for other devices, like LHIfAM, effects of the structural vibration modes has to be taken into account. For characterizing the importance of structural vibration modes, a practical measure of dynamic response of haptic devices is proposed in (Moreyra and Hannaford, 1998).

The numerical and experimental analysis and identification reported in these studies give useful results but they do not provide parametric models that would directly establish the connection between the observed dynamic behaviour and the mechanical system properties.

In addition to these, indices quantifying free-motion and hard-contact transparency are presented in (Tavakoli and Howe, 2007, 2008), where the effect of flexibility in teleoperation systems has been analysed. This analysis relies on continuous-time system representations. The digital realization is not considered and the detailed stability analysis is left for future work.

1.1.6 Mechanical Design of Haptic Devices. As discussed earlier in this chapter, high impedance range, transparency, and fidelity are considered as fundamental requirements in haptic applications. In addition, kinematic and dynamic considerations such as dexterity, and uniform kinematic/dynamic response in the workspace are important in mechanical design of such robotic systems. These requirements and the corresponding design considerations in haptic applications are discussed in (Hayward et al., 1994; Ellis et al., 1996).

Design optimization of haptic devices in the literature are mostly implemented on pre-selected mechanisms. The selection of these mechanism are usually based on factors such as low inertia, high stiffness, no singularity and backlash, and backdrivability. For example, parallel mechanisms are commonly used in haptic devices with base-mounted motors for high structural stiffness and low inertia. In addition, direct-driven mechanisms are usually selected to eliminate transmission problems such as friction and non-backdrivability.

Kinematic and inertia properties of several manipulators are optimized in the literature considering different objective functions. The architecture of a parallel redundant mechanism is optimized from a kinematical viewpoint in (Kurtz and Hayward, 1992). In this work, the joint redundancy is proposed for minimization of the device dynamics-induced parasitic torques/forces and friction. This is implemented by considering the condition number of the Jacobian matrix as an indicator of the amplification factor of relative errors from joints to the reference point. Joint redundancy is also considered in (M. Ueberle and Buss, 2004). In this approach, dexterity, kinematic uniformity, and actuator forces have been considered as potential objective functions for mechanical design of a 10 actuated-DoF haptic device.

Dexterity, manipulability, force capability, inertia, and response uniformity were considered in design optimizations in several haptic devices in the literature. A two-DOF five-bar linkage based haptic device is optimized in (Hayward et al., 1994) considering the dexterity and manipulability of the interface as objective functions. The kinematic properties of this mechanism are optimized such that the response remains as uniform as possible in the workspace. Dexterity and minimization of the apparent inertia were also the objectives in the design of a five-DOF haptic interface in (Vlachos et al., 2004), while satisfying several kinematic constraints was required. Dimensions of a mechanism are optimized in (A. Frisoli and Salsedo, 2007) via multi-objective optimization of several performance measures, such as minimum required torque at actuators and maximum reachable workspace, with the simultaneous fulfillment of design constraints, such as satisfactory mechanical stiffness at the end effector and the global kinematic isotropy over the workspace. Kinematic isotropy, workspace size, endpoint force, and position accuracy were the objectives in the optimization process in (S. Li and Bergamasco, 2010). A 4DoF mechanism is optimized in (Millman and Colgate, 1991) for haptic applications which requires minimum continuous stall motor torques. In (Gil et al., 2012) mechanical properties of a mechanism have been optimized in order to guarantee a proper workspace, manipulability, force capability, and inertia for the device.

In (Stocco et al., 1998) a new global, configuration independent, isotropy index and a discrete global optimization algorithm are presented, where discrete refers to sampling the area in the workspace. This algorithm is used in (Salcudean and Stocco, 2000) for developing force isotropy optimization algorithm which involves the maximization of a workspace inclusive isotropy measure defined as a function of the haptic interface mechanical parameters. These algorithms are used in (Stocco, 2000) where performance of three 6-DOF robots are compared in terms of their semidextrous workspace and static force capabilities.

A design optimization methodology for haptic applications is developed in (Vlachos and Papadopoulos, 2006) focusing on endpoint fidelity. The objective is to minimize the parasitic terms in the force/torque feedback to the human user.

As can be seen, most of the work on design of haptic devices in the literature focuses on kinematics of the selected mechanism. However, in addition to kinematic related performance measures, considering the closed-loop performance in the design of haptic devices is essential. Effects of mechanical and electrical properties of several haptic devices on closed-loop performance are analyzed experimentally in (Salisbury et al., 2011). It is shown that haptic devices produce perceptible artifacts when rendering vibrations near human detection thresholds. By experimentally finding the source of the deficiencies, it is shown that minor modifications to the haptic hardware were sufficient to make these devices well-suited for haptic applications.

In another work, via an energy-based approach, effects of mechanical and structural properties of a teleoperation system are analyzed in design optimization in (Willaert et al., 2010). The analysis in this work demonstrates that there is a trade-off between requirement of low inertia and high stiffness slave robots.

However, these approaches focus on optimization and performance analysis of specific devices and do not provide general guidelines for mechanical design of haptic systems.

1.2 Motivations

Dynamics of haptic systems can significantly influence the quality and nature of haptic rendering. This dynamics primary depends on the mechanical properties of the physical device and the realization of the virtual environment to be rendered. However, effects of mechanical system properties, compared to other factors such as control realization, are overlooked in the current haptic system analysis literature. This is mostly because the transparency of the interface has been over emphasized such that the inertia is minimized down to a level where the dynamic parameters seem to be less important. Another reason can be the incorporation of low pass filters

to suppress the measurement noise and the high frequency structural vibrations of the interface for fidelity improvement. This can limit the performance to a level where dynamic and structural properties are no more essential to be considered. It is also shown that energy based approaches used in the current literature limits the renderable environment to low virtual impedances. These conservative stability results limit the performance such that dynamic and structural properties seem to be unimportant. This has affected the mechanical design of the current haptic devices.

However, in applications where rendering high impedance virtual environments is of interest, development of a framework for parametric analysis of overall haptic system behaviour is necessary to assess the importance of mechanical and control parameters of the system.

1.3 Objectives

The main goal of this work is to develop tools to characterize the effects of mechanical system properties on virtual contact dynamics behaviour. To this end, parametric mechanical models will be developed for the analysis and performance evaluation of multi-DoF haptic systems. These models should incorporate and reflect the influence of overall system properties in a parametric form, yet being simplified to be used in analytical investigations. Representativeness of the proposed models will be investigated in practical applications, when a human operator is interacting with the device. Effects of structural flexibility and filtering on dynamic behaviour of haptic systems will be discussed via incorporating these models.

Furthermore, parametric dynamic analysis will be implemented with the goal to quantify overall performance of haptic systems. As result of this analysis, representative performance indices will be developed which quantify impedance range and fidelity of haptic interfaces including mechanical properties of the system. The resulting performance indices will be compared to those which has commonly been

used in the design of such devices. This can lead to the development of tools for mechanical design optimization of haptic interfaces considering the closed-loop dynamic behaviour of the system.

1.4 Thesis Outline

In this thesis, a modelling framework is developed in Chapter 2, using the general multibody dynamics. This can lead to simplified models, which reflect the influence of the overall system properties. The proposed models are validated experimentally and numerically in Chapter 3 for practical applications. Effects of human operator and the representativeness of the developed models are also studied in that chapter. Using these models, more detailed dynamic analyses are carried out in Chapter 4 which results in closed-form stability conditions as functions of the mechanical properties of the system. Usability of the proposed stability conditions are discussed for different applications. In Chapter 5, parametric performance indices are developed for quantifying impedance range for stable virtual environments and fidelity of the virtual interaction force. These indices are compared with the usual performance indices used in haptic system design in the literature. Finally, the thesis concludes in Chapter 6 by summarizing the most important elements of the presented work.

CHAPTER 2

Dynamics Formulation and Modelling

The dynamics behaviour of haptic interfacing can significantly depend on the mechanical properties of the haptic device. Any haptic device comes with specific electrical and mechanical properties. The relationship between these properties and the performance requirements is of utmost importance. To investigate theses effects, representative dynamic models are essential. For this purpose, we require to develop dynamic models with effective parameters directly be related to mechanical properties in closed-form. The goal in this chapter is to outline dynamic formulations starting from general multibody dynamics and via systematic derivation, develop parametric models for haptic system analysis. The method we introduce here is also applicable in several other areas of mechanical systems.

2.1 Dynamics Modelling

A haptic system generally includes the haptic device, the human operator, and the virtual environment. These three main components contribute to the dynamics. The haptic device can be modelled as a multibody system. Considering the human operator as articulated mechanical systems makes it possible to model the operator's behaviour as another multibody system. This is shown in Fig. 2.1, where three links were used as an example to illustrate multibody systems. The multibody dynamics of the human operator and the device can be connected by modelling the grasp of

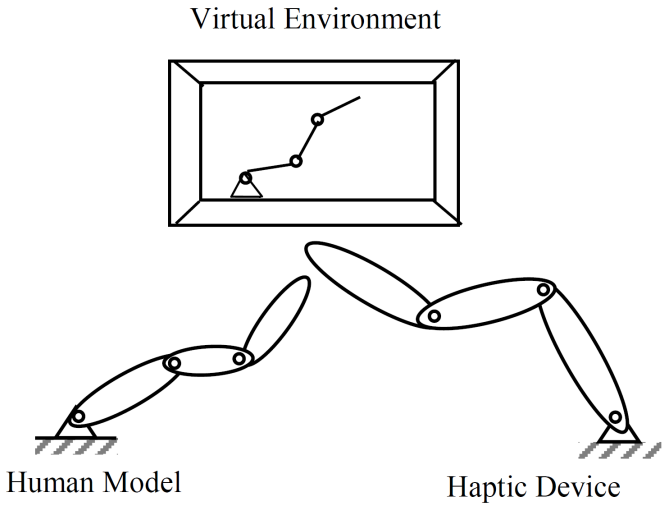

FIGURE 2.1. Multibody haptic system

the device via the operator. This forms a more general multibody dynamic model where the model of the human can add more degrees of freedom to the overall system. As an example if the effect of human operator is modelled via a mass-spring-damper element, for the case of a rigid (firm) grasp, no additional coordinate is needed to represent the human model. However, in the case of a flexible grasp, the model of the human can be connected via another spring-damper element to the device end-point. This model adds one degree of freedom to the multi-DoF mechanical system of the device.

The configuration of a multi-DoF haptic mechanical system can be represented by n generalized coordinates collected in an $n \times 1$ array, $\mathbf{q}$. These coordinates describe the configuration of the haptic device and can also contain representations of degrees of freedom that are associated with the human operator.

The general dynamics model of a haptic mechanical system can be written as

$$\mathbf{H}\ddot{\mathbf{q}} + \mathbf{c} = \mathbf{Q}_p + \mathbf{Q}_v \tag{2.1}$$

where $\mathbf{H}$ is the $n \times n$ mass matrix, $\mathbf{c}$ is the $n \times 1$ array of nonlinear inertia terms, $\mathbf{Q}_p$ represents the generalized forces that arise due to physical sources, and $\mathbf{Q}_v$ includes

the "virtual" generalized forces that represent the virtual interaction forces transmitted from the virtual environment. The physical forces can be further decomposed as

$$\mathbf{Q}_p = \mathbf{Q}_h + \mathbf{Q}_d + \mathbf{Q}_k + \mathbf{Q}_o \tag{2.2}$$

where $\mathbf{Q}_h$ comes from the representation of the human operator force, $\mathbf{Q}_d$ gives the dissipative generalized forces of the haptic device, $\mathbf{Q}_k$ represents the generalized elastic forces that are present only if the structural flexibility of the device is considered, and $\mathbf{Q}_o$ contains other external forces possibly acting on the system.

Typically, the parameterization for the dynamics of the device is selected such that $\dot{\mathbf{q}}$ include joint velocities of the device. In addition, $\dot{\mathbf{q}}$ can also include other velocities that are associated with the human operator representation. In haptic applications the task often corresponds to m distinguished operational-space directions with $m \leq n$. These directions can be seen to form the *rendered subspace*. For example, in interaction with a virtual wall or surface, the single direction perpendicular to the surface is characteristic for haptic rendering and corresponds to the rendered subspace, i.e., $m = 1$. This is illustrated in Fig. 2.2.

The rendered directions at the velocity level can be represented with an $m \times 1$ array, $\mathbf{u}_r$, which can be defined via a linear transformation as

$$\mathbf{A}\dot{\mathbf{q}} = \mathbf{u}_r \tag{2.3}$$

where $\mathbf{A} = \mathbf{A}(\mathbf{q})$ is an $m \times n$ transformation matrix.

Our intention is to develop representations that allow the user to gain information on how the mechanical system of the device is affecting the behaviour of the haptic system. An important element we define here is the concept of *haptic equilibrium*. This concept is a direct extension of the traditional concept of equilibrium in mechanics. The equilibrium configuration is the solution that satisfies the dynamic equations (2.1) with zero velocities and accelerations. Physically, this means the situation where the virtual interaction forces and the human operator forces completely balance each

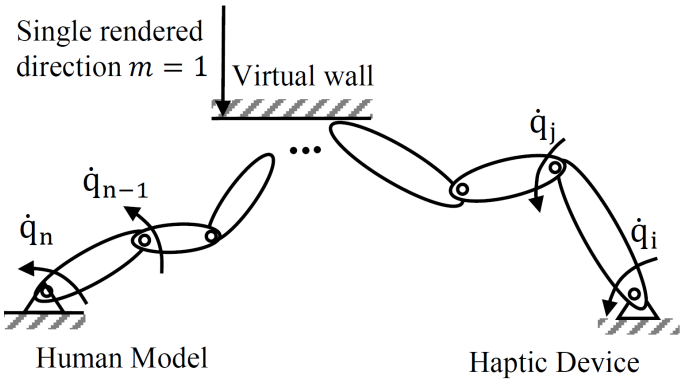

FIGURE 2.2. Haptic equilibrium, interaction with single virtual wall

other via the haptic device, and no motion is involved. This is illustrated in Fig. 2.2 for the case of single rendered direction. For this, (2.1) reduces to the equilibrium equations as

$$\mathbf{0} = \mathbf{Q}_h + \mathbf{Q}_k + \mathbf{Q}_v + \mathbf{Q}_o \tag{2.4}$$

The solution of the dynamic equations in (2.1), which satisfies the above equilibrium condition is $\mathbf{q}_0$. The study of the dynamics representation linearized about this equilibrium configuration can reveal significant information on how the mechanical system parameters influence the haptic dynamic behaviour, the virtual contact dynamics. These linearized equations describe the dynamics associated with small motions about equilibrium. The variables, i.e., coordinates, for small motion can be interpreted as $\mathbf{q}_0 - \mathbf{q} = \boldsymbol{\delta}$. For the sake of simplicity in the following we will reuse $\mathbf{q}$ for the notation of these coordinates. With this the dynamic equations linearized about the haptic equilibrium defined by (2.4) and $\mathbf{q}_0$ can be derived from (2.1) as

$$\mathbf{M}\ddot{\mathbf{q}} = \underbrace{\mathbf{f}_h + \mathbf{f}_d + \mathbf{f}_k}_{\mathbf{f}_p} + \mathbf{f}_v \tag{2.5}$$

where $\mathbf{M} = \mathbf{H}(\mathbf{q}_0)$ is the mass matrix of the linearized system, interpreted for the $\mathbf{q}_0$ configuration; $\mathbf{f}_h$, $\mathbf{f}_d$, $\mathbf{f}_k$, and $\mathbf{f}_v$ are the linearized forms of the different generalized forces, i.e., human force representation, dissipation, structural flexibility and virtual

interaction, respectively, for the perturbations relative to the equilibrium configuration. These force expressions will be expanded and analyzed in more detail in the following. We will see that it will also be easier to discuss these in further detail after the transformation that will be introduced. Here, we assumed that the external forces contained in $\mathbf{Q}_o$ contribute to the development of the equilibrium configuration, but will have negligible effect on the perturbed dynamics. This perturbed dynamics will be primarily influenced by the haptic device properties, the virtual environment, and the human operator.

With the new definition of $\mathbf{q}$ for small motions about equilibrium, the rendered directions can be interpreted with the same formula as $\mathbf{u}_r = \mathbf{A}\dot{\mathbf{q}}$; where now $\mathbf{A} = \mathbf{A}(\mathbf{q}_0)$ has constant elements that are defined for the equilibrium configuration.

Eq. (2.5) with the proper interpretation of the linearized force models on the right-hand side can already serve as basis for analysis. However, for parametric investigations and in order to gain more understanding about the system it can be advantageous to further study the possibilities for decoupling the dynamic equations.

Several techniques for dynamic decoupling of mechanical systems are available in the literature. Modal decomposition (Angeles, 2012) can be used for decoupling linear systems. However, such decomposition requires the introduction of modal coordinates, that do not carry direct physical interpretation. Techniques dealing with dynamic decoupling for the operational space motion/force control of robotic systems and redundant manipulators is proposed and implemented in (Khatib, 1987, 1990; Chang and Khatib, 2000). In these approaches, the intention is to develop operational space control structure in highly redundant manipulators. This approach focuses on decoupling the control torque and does not lead to decoupled dynamic systems.

We take a different approach here, which leads to a level of decoupling of dynamic systems and keeps the physical representation for the rendered directions. For this purpose a transformation is introduced in the following which decomposes the

dynamic equations of (2.5) into equations corresponding to the physical rendered directions and another set of equations that describe the dynamics of motion admissible with the dynamics of the rendered subspace. Via this transformation, a new set of generalized velocities are introduced for the parameterization of the system dynamics so that the two subspaces will be fully or partially decoupled.

For describing the admissible motion, we consider that a complementary set of $n-m$ generalized velocities is introduced in the form

$$\mathbf{B}\dot{\mathbf{q}} = \mathbf{u}_a \tag{2.6}$$

where $\mathbf{u}_a$ is the (n-m)×1 array of these generalized velocities that parameterize the motion admissible with the rendered subspace. There is a significant freedom in the way how $\mathbf{u}_a$ can be selected. This concept has been described in detail in (Kovecses, 2008). The components of $\mathbf{u}_a$ do not necessarily carry direct physical interpretation. The intention here is to keep the original $\mathbf{u})r$ representation for the rendered directions

Considering (2.3) and (2.6) result in the interpretation of a full velocity transformation as

$$\mathbf{u} = \mathbf{R}\dot{\mathbf{q}} \quad \text{, with} \quad \mathbf{R} = \begin{bmatrix} \mathbf{A} \\ \mathbf{B} \end{bmatrix}, \quad \mathbf{u} = \begin{bmatrix} \mathbf{u}_r \\ \mathbf{u}_a \end{bmatrix} \tag{2.7}$$

Both $\mathbf{A}$ and $\mathbf{B}$ here are constant matrices as we deal with the linearized system. Due to this, both $\mathbf{u_r}$ and $\mathbf{u_a}$ can be seen as time derivatives of local coordinate level representations as $\mathbf{u_r} = \dot{\mathbf{x}}$ and $\mathbf{u_a} = \dot{\boldsymbol{\xi}}$, where $\mathbf{x}$ represents small movements along the rendered directions, and $\boldsymbol{\xi}$ give the coordinates for the admissible dynamics.

The fundamental variational form of the dynamics of the system can be represented as

$$\delta\dot{\mathbf{q}}^{\mathrm{T}}(-\mathbf{M}\ddot{\mathbf{q}} + \mathbf{f}_p + \mathbf{f}_v) = \mathbf{0} \tag{2.8}$$

Using the transformation in Eq. (2.7) the dynamic equations in (2.8) can be written as

$$\delta\mathbf{u}^{\mathrm{T}}\mathbf{R}^{-\mathrm{T}}(-\mathbf{M}\mathbf{R}^{-1}\dot{\mathbf{u}} + \mathbf{f}_p + \mathbf{f}_v) = \mathbf{0} \tag{2.9}$$

The only condition for the transformation described in eq. (2.7) is that $\mathbf{R}$ needs to be invertible. As $\mathbf{A}$ is already specified via the distinguished directions of the haptic system, the properties of $\mathbf{R}$ are governed by $\mathbf{B}$. Based on Eq. (2.9) the dynamic equations in terms of new generalized velocities can be written as

$$\underbrace{\mathbf{R}^{-\mathrm{T}}\mathbf{M}\mathbf{R}^{-1}}_{\mathbf{W}}\dot{\mathbf{u}} = \underbrace{\mathbf{R}^{-\mathrm{T}}\mathbf{f}_p}_{\mathbf{h}_p} + \underbrace{\mathbf{R}^{-\mathrm{T}}\mathbf{f}_v}_{\mathbf{h}_v} \tag{2.10}$$

where the new arrays of physical and virtual generalized forces are given by $\mathbf{h}_p$ and $\mathbf{h}_v$ and the transformed mass matrix is represented by $\mathbf{W}$. Let us consider the generalized virtual interaction forces for the rendered directions by an $m \times 1$ array denoted by $\boldsymbol{\lambda}$. Based on the power of forces and the transformation described in Eq. (2.3) between generalized velocities and the rendered directions, it can be shown that,

$$\dot{\mathbf{q}}^{\mathrm{T}}\mathbf{f}_v = \mathbf{u}_r^{\mathrm{T}}\boldsymbol{\lambda} \tag{2.11}$$

which leads to

$$\mathbf{f}_v = \mathbf{A}^{\mathrm{T}}\boldsymbol{\lambda} \tag{2.12}$$

Then considering the transformation between $\mathbf{f}_v$ and $\mathbf{h}_v$ and the full transformation in Eq. (2.7), we can obtain $\mathbf{h}_v = [\boldsymbol{\lambda}^{\mathrm{T}}\ \mathbf{0}^{\mathrm{T}}]^{\mathrm{T}}$.

The transformed dynamic equations in (2.10) can then be further expanded as

$$\begin{bmatrix} \mathbf{W}_{rr} & \mathbf{W}_{ra} \\ \mathbf{W}_{ar} & \mathbf{W}_{aa} \end{bmatrix} \begin{bmatrix} \dot{\mathbf{u}}_r \\ \dot{\mathbf{u}}_a \end{bmatrix} = \begin{bmatrix} \mathbf{s}_r \\ \mathbf{s}_a \end{bmatrix} + \begin{bmatrix} \boldsymbol{\lambda} \\ \mathbf{0} \end{bmatrix} \tag{2.13}$$

where the subscripts "r" and "a" denote partitioning according to the rendered and admissible decomposition, and the physical generalized forces are decomposed as $\mathbf{h}_p = [\mathbf{s}_r^{\mathrm{T}}\ \ \mathbf{s}_a^{\mathrm{T}}]^{\mathrm{T}}$. The virtual interaction forces $\boldsymbol{\lambda}$ are associated with the rendered directions only, but the dynamics in the rendered and admissible directions can still be coupled through the mass matrix, and possibly via the physical applied forces, such as the ones arising from structural flexibility.

The expansion of the inverse of the transformed mass matrix gives

$$\mathbf{W}^{-1} = \mathbf{R}\mathbf{M}^{-1}\mathbf{R}^{\mathrm{T}} = \begin{bmatrix} \mathbf{A}\mathbf{M}^{-1}\mathbf{A}^{\mathrm{T}} & \mathbf{A}\mathbf{M}^{-1}\mathbf{B}^{\mathrm{T}} \\ \mathbf{B}\mathbf{M}^{-1}\mathbf{A}^{\mathrm{T}} & \mathbf{B}\mathbf{M}^{-1}\mathbf{B}^{\mathrm{T}} \end{bmatrix} \tag{2.14}$$

The idea here is to introduce the set of generalized velocities $\mathbf{u}$ for the parameterization of the system dynamics so that the mass matrix is decoupled. If $\mathbf{B}$ is selected such that

$$\mathbf{A}\mathbf{M}^{-1}\mathbf{B}^{\mathrm{T}} = \mathbf{0} \tag{2.15}$$

i.e., $\mathbf{B}$ is an orthogonal complement of $\mathbf{A}\mathbf{M}^{-1}$, then transformed inverse of the mass matrix in (2.14) will be block diagonal. Based on Eq. (2.6), we will require that $\mathbf{u}_a$ is defined so that $\mathbf{B}$ satisfies condition Eq. (2.15). With such a choice for the parametrization of admissible motion, the coupling through the mass matrix can be eliminated, and the dynamic equations take the form

$$\mathbf{W}_{rr}\dot{\mathbf{u}}_r = \mathbf{s}_r + \boldsymbol{\lambda} \tag{2.16}$$

$$\mathbf{W}_{aa}\dot{\mathbf{u}}_a = \mathbf{s}_a \tag{2.17}$$

with $\mathbf{W}_{rr} = \left(\mathbf{A}\mathbf{M}^{-1}\mathbf{A}^{\mathrm{T}}\right)^{-1}$ and $\mathbf{W}_{aa} = \left(\mathbf{B}\mathbf{M}^{-1}\mathbf{B}^{\mathrm{T}}\right)^{-1}$ representing the effective mass matrices for the rendered and admissible dynamics, respectively. Here, the effective mass matrix of the rendered subspace is of primary importance. We note again that in this analysis $\mathbf{u}_r$ carries direct physical interpretation of the rendered directions. On the other hand, the entries of $\mathbf{u}_a$ does not have to be associated with direct physical meaning; they play a role similar to that of modal coordinates. They are defined via specifying a transformation to achieve a desired form of the system model. This is completely compatible with the general principles of analytical mechanics (Papastavridis, 2002).

Dissipative forces are included in $\mathbf{s}_r$ and $\mathbf{s}_a$. Physical dissipation is a phenomenon very difficult to model. The viscous dampers are only very simplistic representations.

We will here follow the general practice of structural engineering to develop the parametric models first and then add dissipation explicitly in the form of so-called modal damping.

The representation derived above is valid for any haptic system. However, we have to elaborate on two important cases: (1) when all physical elements in the system are modelled as rigid bodies with perfect joints, and (2) when structural flexibility is considered. The resulting models will have different numbers of degrees of freedom, but can generally be represented as discussed above. In the following below, we keep the same notation that was used earlier with the understanding that the dimension of the appropriate matrices matches the number of DoFs needed for the particular model.

2.1.1 Rigid-Body Model. In this case, the structural flexibility related generalized forces $\mathbf{f}_k$ in eq. (2.5) and the corresponding terms in $\mathbf{s}_r$ and $\mathbf{s}_a$ in eqs. (2.16) and (2.17) vanish. Each actuated joint is well represented with one single variable, and the generalized coordinates and velocities, $\mathbf{q}$ and $\dot{\mathbf{q}}$, contain these joint variables and their time derivatives. If $\mathbf{J}$ represents the $m \times n$ Jacobian of the system, which connects the joint rates to the rendered operational space directions, then, in this case the transformation to the rendered direction can be defined as

$$\mathbf{A} = \mathbf{J} \tag{2.18}$$

With this the effective mass matrix for the rendered directions can be interpreted. In this rigid-body model, the linearized physical generalized forces, $\mathbf{s}_r$ and $\mathbf{s}_a$, would only originate from the variations of the human operator force about the equilibrium state and the dissipative effects of the device. If it is assumed that the operator primarily develops force/moments associated with the rendered directions, then

$$\begin{aligned} \mathbf{s}_a &= \mathbf{s}_{ad} \\ \mathbf{s}_r &= \mathbf{s}_h + \mathbf{s}_{rd} \end{aligned} \tag{2.19}$$

where $\mathbf{s}_{ad}$ and $\mathbf{s}_{rd}$ contain the dissipative generalized forces for the admissible and rendered directions respectively, and $\mathbf{s}_h$ comes from the human operator force representation. For this case the linearized dynamics equations of the rendered and admissible motions, (2.16) and (2.17) can be seen decoupled, and the haptic system behaviour will be governed by the dynamics of the rendered subspace described with

$$\mathbf{W}_{rr}\dot{\mathbf{u}}_r = \mathbf{s}_h + \mathbf{s}_{dr} + \boldsymbol{\lambda} \tag{2.20}$$

2.1.2 Model with Structural Flexibility. The second case is when structural flexibility can have an important effect on the dynamic behaviour. The main sources of structural flexibility can come from the joints and the links. Localized joint flexibility is typical in many systems. On the other hand, link flexibility may become important in systems with direct driven joints. The full model represented by (2.16) and (2.17) can be used also when structural flexibility is considered. However, if flexibility is present then the rendered and admissible dynamics will stay coupled as the linearized structural terms will add contributions to both $\mathbf{s}_r$ and $\mathbf{s}_a$ in (2.16) and (2.17).

The flexibility of haptic systems can be often associated with the joints drives. In this case, the joint deflections can usually be represented as $\boldsymbol{\varphi} = \boldsymbol{\phi} - \boldsymbol{\theta}$, (Spong, 1987; Luca, 1998), where $\boldsymbol{\phi}$ and $\boldsymbol{\theta}$ are $n\times 1$ arrays corresponding to the link positions and actuator positions, respectively. The actuator positions are reflected through the transmission elements used for the joints and they are interpreted at the joint level. Therefore, the generalized flexible-jointed model can be developed by considering the generalized coordinates defined as $\mathbf{q} = [\boldsymbol{\phi}^{\mathrm{T}}\ \boldsymbol{\theta}^{\mathrm{T}}]^{\mathrm{T}}$. When the transmission ratio is large enough the inertial coupling between the actuators and the links are negligible and the linearized dynamic equations in (2.5) can be written as

$$\begin{aligned} \mathbf{M}_{\phi}\ddot{\boldsymbol{\phi}} &= -\mathbf{K}(\boldsymbol{\phi} - \boldsymbol{\theta}) + \mathbf{f}_h + \mathbf{f}_{d,\phi} \\ \mathbf{M}_{\theta}\ddot{\boldsymbol{\theta}} &= \mathbf{K}(\boldsymbol{\phi} - \boldsymbol{\theta}) + \mathbf{f}_v + \mathbf{f}_{d,\theta} \end{aligned} \tag{2.21}$$

where $\mathbf{M}_\phi$, $\mathbf{M}_\theta$, $\mathbf{f}_{d,\phi}$ and $\mathbf{f}_{d,\theta}$ are inertia matrices and dissipative torques associated with links and actuators, respectively; and $\mathbf{K}$ is the joint-level effective stiffness matrix.

There are several approaches for modelling distributed flexibility, for the case when link flexibility become important in the system. The most common approach is the finite element method (FEM) (Cleghorn et al., 1981). Another approach is the assumed-modes method (AMM) (Book, 1984), which is computationally more efficient compared to FEM, and is based on the dynamic behaviour of the system. In this method, the elastic deflection of the flexible link is described by finite number of modes of the system (Zhang et al., 2007). However, the distributed flexibility can also be modelled by considering the first vibration mode of each link only, where the dominant frequency is captured by this mode (Tavakoli and Howe, 2008; Zhu et al., 1999). Another approach is considering the static deflection of the flexible link by which lumped parameters model can be constructed.

As an example, one can consider a single flexible link modelled as an Euler-Bernoulli beam, while the flexural flexibility is considered only. In this case, with the assumption of small deflections, the end-point deflection of the flexible link, denoted by δ, can be defined as $\delta = L(\phi - \theta)$, where ϕ and θ correspond to the link and joint position. A lumped parameter model can be obtained by considering an equivalent lumped mass, m_e, located at the end-point of the link, and the corresponding flexibility is modelled by a massless linear bending spring k_Φ. The corresponding dynamic equations can be written as

$$\begin{aligned} m_e L\ddot{\phi} &= -k_e L(\phi - \theta) + f_e \\ J_\theta \ddot{\theta} &= k_e L^2(\phi - \theta) + \tau_m \end{aligned} \tag{2.22}$$

f_e is the applied force at the end-point, J_θ is the hub/motor inertia and τ_m is the motor torque. The resulting dynamic equations can be written as

$$\begin{aligned} J_\phi \ddot{\phi} &= -k_\theta(\phi - \theta) + \tau_e \\ J_\theta \ddot{\theta} &= k_\theta(\phi - \theta) + \tau_m \end{aligned} \tag{2.23}$$

where $J_\Phi = L^2 m_e$ is the equivalent joint-level inertia of the lumped mass, $k_\theta = L^2 K_e$ is the equivalent joint-level stiffness, and $\tau_e = L f_e$ is the equivalent joint torque corresponding to the end-point applied force. Dynamic equations in (2.23) is obtained in a form similar to that of a flexible jointed system in (2.21), where the localized structural stiffness representation also embeds effects of link flexibility. This is an example for a single flexible link,which can be extended to consider multi flexible links.

2.1.2.1 *Modelling of haptic systems with structural flexibility.* In the following we consider the dynamic equations in (2.21) as the basis of our investigations for the effects of structural flexibility. The analysis of these coupled dynamic equations is possible via numerical methods, but they do not make it possible to establish closed-form results that explicitly reflect the influence of various parameters. Later in this thesis we will also use the full set of coupled equations for comparison. However, first we will look at the possibility to develop reduced-order representations that can better highlight and capture the essence of the core phenomena.

Some considerations and assumptions may be possible about neglecting the structural coupling depending on the application and the specific device at hand. But, in general, the coupling remains and the model reduction is not possible in the same way as done for the rigid body model. In the following, we present an alternative way to establish simplified parametric models for the consideration of the effects of structural flexibility. The basis of the development of such simplified models will be rooted in the way how the human operator interacts with the virtual environment via the haptic device.

The human operator usually interacts with the device at the physical reference point/frame. However, the virtual environment representation is directly related to the actuators where the driving torques/forces are applied. In other words, the locations of application of the two sets of forces are not the same. Such a problem does not exist in the case where the human interacts with a real physical environment. Also, this does not give much difference if the device is modelled using rigid bodies and perfect joints. On the other hand, for a flexible system it makes a difference as it gives the possibility to view the rendered directions and the way how they are related to the device dynamics from two points of view: from the point of view of the operator, and from the point of view of the virtual environment. Based on the application location, different transformations can be considered for projecting to the rendered directions.

In this case, from the human operator perspective, the relation of the rendered directions to the joints can be interpreted via considering only the transformation of link position to the rendered direction. As was defined earlier, the $2n \times 1$ array of $\mathbf{q}$ contains both sets of generalized coordinates necessary to describe rigid-body motion and deformations. From the kinematics point of view, $m \times n$ Jacobian matrix of the rigid-body model of the device connects the time derivatives of both link and actuators positions to rendered directions. The transformation connecting the link position to the rendered direction, from the virtual environment perspective, can be obtained as

$$\dot{\mathbf{x}}_1 = \mathbf{A}_1 \dot{\mathbf{q}} \tag{2.24}$$

where

$$\mathbf{A}_1 = [\mathbf{J} \;\; \mathbf{0}] \tag{2.25}$$

and another transformation can be considered connecting the actuator position to the rendered directions as

$$\dot{\mathbf{x}}_2 = \mathbf{A}_2 \dot{\mathbf{q}} \tag{2.26}$$

where

$$\mathbf{A}_2 = [\mathbf{0} \;\; \mathbf{J}] \tag{2.27}$$

while both $\mathbf{A}_1$ and $\mathbf{A}_2$ are $m \times 2n$ matrices; and $\mathbf{0}$ represents an $m \times n$ zero matrix. This gives the possibility to interpret the concept of two effective inertia representations for the rendered directions as

$$\begin{aligned} \mathbf{W}_{r1} &= (\mathbf{A}_1 \mathbf{M}^{-1} \mathbf{A}_1^{\mathrm{T}})^{-1} \\ \mathbf{W}_{r2} &= (\mathbf{A}_2 \mathbf{M}^{-1} \mathbf{A}_2^{\mathrm{T}})^{-1} \end{aligned} \tag{2.28}$$

where the variables associated with these are $\mathbf{x}_1$ and $\mathbf{x}_2$. The two effective masses in the rendered directions are connected via massless flexible elements. This concept is illustrated in Fig. 2.3. To illustrate more the physical meaning of $\mathbf{W}_{r1}$ and $\mathbf{W}_{r2}$, let us consider the hypothetical case if the flexible connection connecting the links to the actuators are cut. Then $\mathbf{W}_{r1}$ represents the inertia that would be felt by the human operator, and $\mathbf{W}_{r2}$ is the inertia the actuators would feel.

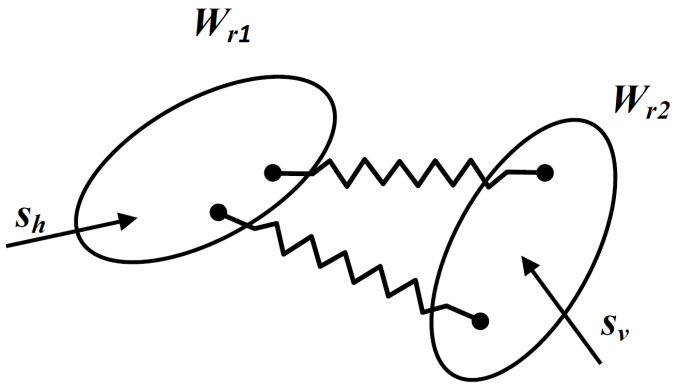

FIGURE 2.3. Modelling Haptic system with structural flexibility

The above interpretation allows us to model the system as the two effective generalized inertia representations connected via the effective stiffness that can be derived considering the static model of the system. For the static model, the joint actuators are considered to be locked and only the pure deflection mode exists for the system, which is represented by $\boldsymbol{\varphi}$, and associated with a $n \times n$ stiffness matrix $\mathbf{K}_{\varphi}$, where n corresponds to the number of actuators. For the static model the mapping

between the joint deflections and the rendered directions can be described via the Jacobian of the rigid-body model of the device as

$$\mathbf{J}\boldsymbol{\varphi} = \mathbf{x} \tag{2.29}$$

where $\mathbf{x}$ is the $m \times 1$ array of end-point deflection in the rendered directions. Considering this transformation and using the principle of virtual work (Greenwood, 2003), we can write

$$\delta\boldsymbol{\varphi}^{\mathrm{T}}\mathbf{f}_k = \delta\mathbf{x}^{\mathrm{T}}\mathbf{h}_k \tag{2.30}$$

where substituting (2.29) to (2.30) leads to

$$\mathbf{f}_k = \mathbf{J}^{\mathrm{T}}\mathbf{h}_k \tag{2.31}$$

Equation (2.31) provides the transformation between the force due to structural flexibility in rendered directions and joint level. Considering this transformation and substituting it in relation $\boldsymbol{\varphi} = \mathbf{K}_{\varphi}^{-1}\mathbf{f}_k$, we can obtain

$$\boldsymbol{\varphi} = \mathbf{K}_{\varphi}^{-1}\mathbf{J}^{\mathrm{T}}\mathbf{h}_k \tag{2.32}$$

Substituting this to the transformation in (2.29) leads to

$$\mathbf{x} = \mathbf{J}\mathbf{K}_{\varphi}^{-1}\mathbf{J}^{\mathrm{T}}\mathbf{h}_k \tag{2.33}$$

Based on this, the effective stiffness matrix for the rendered subspace can be obtained as

$$\mathbf{K}_e = (\mathbf{J}\mathbf{K}_{\varphi}^{-1}\mathbf{J}^{\mathrm{T}})^{-1} \tag{2.34}$$

For the case of m rendered directions, it can be seen that the haptic system can be modelled via two effective inertias represented by $m \times m$ effective mass matrices connected via a spring element with stiffness represented by an $m \times m$ matrix of effective structural stiffness. In this model, the human operator force representation, $\mathbf{s}_h$, is applied to $\mathbf{W}_{r1}$, while the virtual interaction force, $\boldsymbol{\lambda}$, is applied to $\mathbf{W}_{r2}$. This leads to a 2m-DoF model for the dynamics of the haptic rendering. The dynamic

equations for this can be established as

$$\begin{bmatrix} \mathbf{W}_{r1} & \mathbf{0} \\ \mathbf{0} & \mathbf{W}_{r2} \end{bmatrix} \begin{bmatrix} \ddot{\mathbf{x}}_1 \\ \ddot{\mathbf{x}}_2 \end{bmatrix} + \begin{bmatrix} \mathbf{K}_e & -\mathbf{K}_e \\ -\mathbf{K}_e & \mathbf{K}_e \end{bmatrix} \begin{bmatrix} \mathbf{x}_1 \\ \mathbf{x}_2 \end{bmatrix} = \begin{bmatrix} \mathbf{s}_h \\ \boldsymbol{\lambda} \end{bmatrix} + \begin{bmatrix} \mathbf{s}_{dr1} \\ \mathbf{s}_{dr2} \end{bmatrix} \tag{2.35}$$

where $\mathbf{s}_{dr1}$ and $\mathbf{s}_{dr2}$ represent dissipative force terms. The linearized virtual interaction force $\boldsymbol{\lambda}$ can be represented as

$$\boldsymbol{\lambda} = -\mathbf{k}_p \mathbf{x}(t_j) + \mathbf{k}_d \mathbf{v}(t_j) \ , \quad t \in [t_j, t_{j+1}) \tag{2.36}$$

where $\mathbf{k}_p$ and $\mathbf{k}_d$ are virtual stiffness and virtual damping matrices, respectively, $t_j = j\Delta t$, Δt is the sampling time, and $v(t_j) \approx \dot{x}(t_j) = u_r(t_j)$ is the estimated velocity at t_j from the encoder position data. The applied filtering depends on the specific application, but often simple backward differentiation is used.

2.1.3 Further Analysis. The left hand side of (2.35) can be used to determine natural frequencies of the haptic system model where the virtual interaction forces and physical dissipation are not considered. However, the virtual interaction forces, $\boldsymbol{\lambda}$ can significantly influence the dynamic behaviour in haptic systems, and cannot be eliminated in the dynamic analysis. This is one of the core factors in determining the dynamic range of a haptic system (Colgate and Brown, 1994).

The stability and dynamic properties of the rigid-body model in (2.20), and the flexible model in (2.35) can be studied via the construction of a discrete mapping as described in (Kuo, 1981; Stepan, 2001). These continuous-time systems with discrete-time applied force form a system of non-homogeneous ordinary differential equations with piecewise constant right hand side. The general solution of this system can be constructed from sum of the homogeneous part and a particular solution of the non-homogeneous part. The particular solution can be obtained for each subsequent sampling interval. In other words, during each sampling interval, when $t \in [t_j, t_{j+1})$, the applied force is a constant value. In this case, one can apply the usual exponential trial solution as

$$\mathbf{Z}_j = \mathbf{c} e^{s t_j} \tag{2.37}$$

where $\mathbf{Z}_j$ represents the discrete state vector formed based on the generalized coordinates and velocities at time t_j, and the coefficient $\mathbf{c}$ can be obtained using the initial conditions at the beginning of time interval. Then, the general solution at the end of each sampling interval can be determined by considering the solution at the end of previous sampling interval as initial conditions.

Considering this, piecewise solution of the dynamic equations in (2.20) and (2.35) leads to a discrete map which can be established as

$$\mathbf{Z}_{j+1} = \mathbf{L}\mathbf{Z}_j \tag{2.38}$$

where $\mathbf{L}$ is the so-called transition matrix that embeds properties of the system. The dimensions of $\mathbf{Z}$ and $\mathbf{L}$ depends on the states of the discretized dynamic systems and the augmenting states (delayed position sequence) associated with the virtual environment realization.

Convergence of the discrete mapping in (2.38) is equivalent to the asymptotic stability of the piecewise continuous mechanical systems in (2.20) and (2.35) (Stepan, 2001). Therefore, stability of the system can be determined via the eigenvalues of transition matrix $\mathbf{L}$, denoted by z. However, for further analysis of the system, we need to study the vibration frequencies along the stability limits and also the calculation of the exponential decays. Therefore, it is advantageous in the analysis here to formulate the stability in terms of characteristic exponents s. Consider the exponential trial solution in (2.37), the characteristic equation of the system can be written as

$$\det(e^{s\Delta T}\mathbf{I} - \mathbf{L}) = 0 \tag{2.39}$$

This equation has an infinite number of roots s_k, $k = 1, 2, ...$, which can be considered as points along finite number of vertical lines in the left hand side of the complex plane. However consider that an infinite number of characteristic roots belong to a single eigenvalue z. This relation can be written as

$$z = e^s \Delta T \quad \longleftrightarrow \quad s = \frac{lnz}{\Delta T} \tag{2.40}$$

With this transformation, the infinite number of characteristic roots transfer to a finite number of points located inside a unit circle. As a result, the condition for stability of such systems can be written as

$$\det(z\mathbf{I} - \mathbf{L}) = 0 \quad |z_i| < 1 \quad i = 1, 2, ..., n \quad \Leftrightarrow \quad \text{Re } s_k < 0, \quad k = 1, 2, ... \tag{2.41}$$

The eigenvalues of $\mathbf{L}$ whose magnitudes are close to unity tend to dominate the response of the system since their contribution takes a longer time to die out. When the haptic system loses stability, typically the magnitude of one of the complex conjugate pairs of eigenvalues just exceeds unity. The base harmonic frequency associated with this complex conjugate pair will dominate the oscillatory behaviour. This *dominant frequency* of the combined physical-virtual system plays a role similar to the first natural frequency of a purely continuous-time physical system. The determination of the stability boundaries in the space of the parameters of the virtual interaction force representation is a key element in the analysis.

2.2 Single Virtual Wall Interaction

A typical case in haptics is when either force or moment rendered. In that case the rendered subspace for haptic equilibrium reduces to one single direction that is determined by the resultant force or moment to be transmitted. This single rendered direction is considered in the operational space, and $u_r = \dot{x}$ represent the velocity in that direction for force rendering and the angular velocity about the axis of rotation for moment rendering. The most common example is the virtual wall or surface. In the following we will often reference to this. However, the analysis is applicable to more general situations as well. Consider the case when a single rendered direction perpendicular to the virtual wall is implemented in the operational space. A frequently used model to represent the virtual wall interaction forces and establish the virtual coupling relies on the Kelvin-Voigt viscoelastic model, i.e., a spring and damper in parallel. Having a single rendered direction, the effective mass and stiffness representations reduce to scalar quantities. Assuming that the human

operator representation adds no extra DoF in the model, then the representation reduces to a single-DoF model and the corresponding dynamic equations for the rigid-body model with perfect joints can be written based on (2.20) as

$$m_e\ddot{x} = s_h + \lambda + s_{dr} \tag{2.42}$$

where $m_e = (\mathbf{J}\mathbf{M}^{-1}\mathbf{J}^{\mathrm{T}})^{-1}$, while $\mathbf{A} = \mathbf{J}$ is $1 \times n$ row matrix in this case. This model is representative when flexibility is not considered either because of the construction of the device or the operation of the system takes place in the range of low virtual impedances.

Filters are also often employed to reduce the effect of unmodelled dynamics (e.g. structural flexibility), or the noise due to velocity estimation with quantized and sampled position data (Metzger et al., 2012). If the high frequency components are filtered out for such a case then the model in (2.42) can also be used to consider the physical part of the haptic system.

In the presence of structural flexibility the dynamics, in the case of one single rendered direction, and again assuming no extra DoFs for human operator model, can be described based on (2.35) as

$$\begin{aligned} m_{e1}\ddot{x}_1 + k_e(x_1 - x_2) &= s_h + s_{dr1} \\ m_{e2}\ddot{x}_2 + k_e(x_2 - x_1) &= \lambda + s_{dr2} \end{aligned} \tag{2.43}$$

where the effective parameters are in scalar form as $m_{e1} = (\mathbf{A}_1\mathbf{M}^{-1}\mathbf{A}_1^{\mathrm{T}})^{-1}$ and $m_{e2} = (\mathbf{A}_2\mathbf{M}^{-1}\mathbf{A}_2^{\mathrm{T}})^{-1}$ with the interpretation of $\mathbf{A}_1$ and $\mathbf{A}_2$ given before, and are in this case $1 \times 2n$ row matrices. In this case, the human operator representation can consist of a stiffness term and dissipation. We emphasize that the effective parameters of these simplified models embed the mechanical properties of the overall haptic mechanical system.

The human stiffness is usually much lower than structural stiffness. The effective mass m_{e2} is typically small and the characteristic vibrations at high virtual wall impedances take place relative to the larger mass m_{1e}. Therefore, the important

frequency is dominantly influenced by the smaller mass m_{e2}. This can allow for introducing a further simplified single-DoF model considering the dynamics corresponding to m_{e2} in (2.43) in the form

$$m_{e2}\ddot{x}_2 + k_e x_2 = \lambda + s_{dr2} \tag{2.44}$$

As discussed before the human operator can also be modelled as articulated mechanical systems. Equation (2.35) can be used for a more general representation of the human operator effects. However, the human operator is often characterized by series of linear impedance elements along the rendered direction (Hogan, 1989; Speich et al., 2005). With this assumption, (2.42) and (2.43) can be used to further investigate the effect of human operator models. In the presence of structural flexibility, the higher frequency structural modes of the system will govern the dynamics, and one can use the one-DoF flexible model of (2.44). By considering this simplified model, the human model does not directly enter into the analysis. This corresponds to the worst-case scenario where the potentially stabilizing and dissipative effects of the human operator are not present (Diolaiti et al., 2006).

CHAPTER 3

Experimental Evaluation

This chapter investigates the validity of the models developed in Chapter 2. For this purpose, a five-bar linkage based haptic device is used for the experimental evaluation. Two types of experiments were carried out. First, interaction with a bilateral virtual wall is considered, without human operator's sustained touch; and second when a human operator interacts with a unilateral virtual wall via the haptic device. The experimentally measured stability boundaries are compared to that obtained numerically using the models developed.

Due to the capstan drive mechanisms used in this device, structural flexibility can become an important factor. In this case, the validity of the flexible model can be studied. On the other hand, the usability of the rigid-body model can be investigated while the device is used for interaction with low-stiffness virtual environment, or when filtering is employed in the system. This is investigated by incorporating a 2nd-order Butterworth filter as an example.

3.1 Experimental Device

For the analysis in this chapter, we consider the haptic device shown in Fig. 3.1 The device is based on a five-bar mechanism with two actuated joints at the base. The driving mechanisms of the joints are based on capstan drives, where the motor pulleys are connected with a single cable. This device can be modelled based on the kinematic

diagram of the five-bar linkage as shown in Fig. 3.2. The ground link has zero length, and the axes (A and C) of the actuated links, (link 1 and link 3), are collinear. The corresponding CAD model of these links together with the attached motor is shown in Fig. 3.3. Links 2 and 4 are the distal links, which are called as passive arms. The passive arms are lightweight compared to the driven arms which carry the driving motors. The links are modelled as rigid-bodies with a slender beam-like shape.

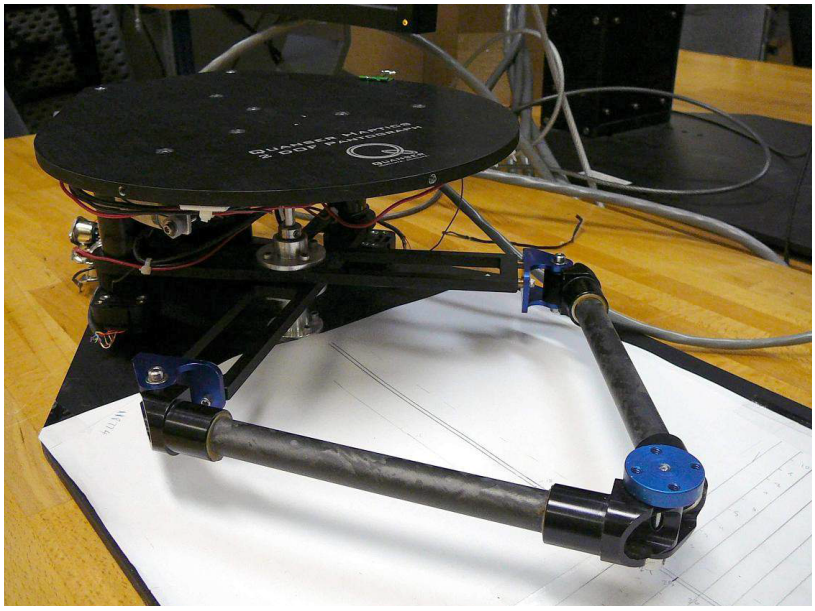

FIGURE 3.1. Experimental device

3.1.1 Model Parameters. The device in Fig. 3.1 is actuated by two Maxon 118774 brushed DC motors. Inertia properties and other data of the motors at nominal voltage are listed in Table 3.1. It has to be noted that the operation range is limited to ±10 V by the processor used for these experiments.

The distance between the axes of the motors and the driven joints is 96 mm, and the diameter of the cable pulley is approximately 9.9 mm. According to these dimensions, the transmission ratio of the driving mechanism can be approximately calculated as $K_g = (96 - 4.95)/4.95 = 18.6$. Using this transmission ratio, the motor inertia I_{mot} at the joint axis level can be calculated as $K_g^2 I_{mot} = 1.186 \times 10^{-4}\ kgm^2$. Table 3.2 lists the geometry and inertia properties of the haptic device. The locations

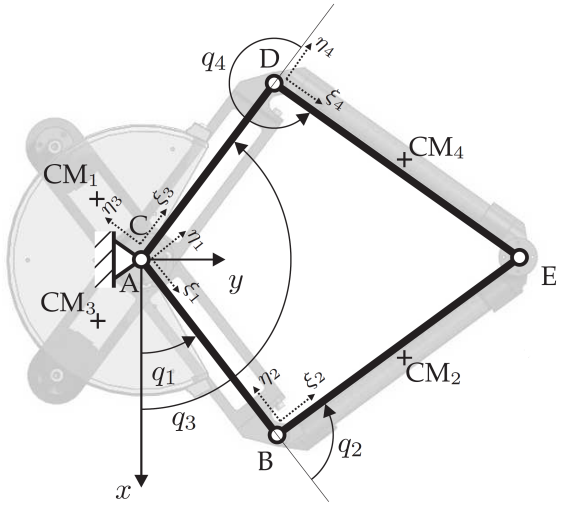

FIGURE 3.2. Five-bar linkage, modelling of haptic device

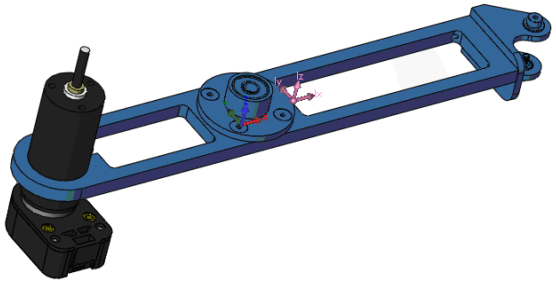

FIGURE 3.3. CAD model of the driven arm

of the centres of mass of the individual links are given in the local frames with axes ξ_i, η_i and ζ_i as shown in Fig. 3.2. These axes are aligned as ξ_i points toward the output joint of the i^{th} link, ζ_i is directed upwards and it is perpendicular to the plane of the mechanism, while η_i is such that they form a right-handed system. By comparing motor inertia at the joint level and the inertia properties of the linkage, it can be

TABLE 3.1. Maxon motor properties

Nominal voltage	48 V
Nominal current	0.659 A
Torque constant	50.2 mNm/A
Rotor inertia	12.1 gcm^2

TABLE 3.2. Multibody model parameters

Geometry data			
l_1	0.147 m	l_2	0.199 m
l_3	0.147 m	l_4	0.199 m
ξ_{CM1}	-0.04565 m	η_{CM1}	-0.0001 m
ξ_{CM2}	0.0902 m	η_{CM2}	-0.0075 m
ξ_{CM3}	-0.04565 m	η_{CM3}	0.0001 m
ξ_{CM4}	0.0902 m	η_{CM4}	0.0075 m
Inertia properties			
m_1	0.282 kg	m_2	0.05427 kg
m_3	0.282 kg	m_4	0.05427 kg
I_{CM1}	0.0024 kgm^2	I_{CM2}	0.000341 kgm^2
I_{CM3}	0.0024 kgm^2	I_{CM4}	0.000341 kgm^2

seen that the inertia of the rotor has to be considered in the mechanical model. The kinematic and dynamic models of the device are described in detail in Appendix B.

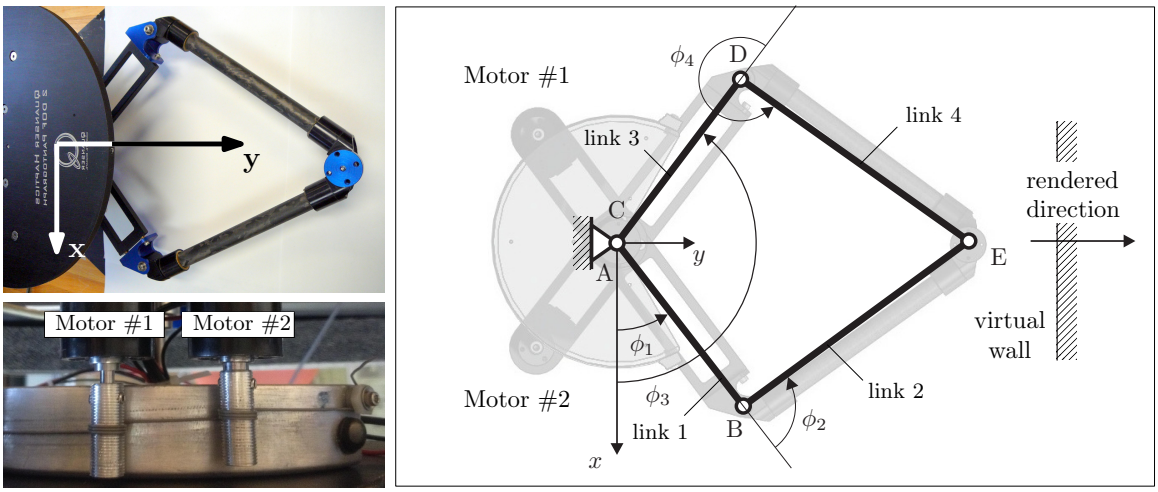

FIGURE 3.4. Left: experimental device and its capstan drive, right: mechanical model

3.1.2 Dynamic Modelling. Capstan drive mechanism has been considered in many available haptic devices (Massie and Salisbury, 1994). This driving system avoids the use of gears, and makes it possible to amplify the torque of small DC motors, and still keeps the system back-drivable. However the tension in the cable

can bend the motor pulleys and twist the driven links connected to the motors (see Fig. 3.4). This results in the need to consider the structural flexibility in the capstan drive, which can be modelled as localized joint flexibility. With ideal, rigid joints, this five-bar linkage would have two-DoFs. The flexibility of the driven joints can introduce two additional DoFs. Therefore, this system can be parameterized with four absolute coordinates as a minimum set specified by $\mathbf{q} = [\boldsymbol{\phi}^{\mathrm{T}}\ \boldsymbol{\theta}^{\mathrm{T}}]^{\mathrm{T}}$, where $\boldsymbol{\phi} = [\phi_1\ \phi_3]^{\mathrm{T}}$ are the angles representing the configuration of the links, and $\boldsymbol{\theta} = [\theta_1\ \theta_3]^{\mathrm{T}}$ is the array of joint level motor angles. Then the linearized minimum set of dynamic equations in (2.21) for the four-DoF flexible-joint model of this device can be written in matrix form as

$$\begin{bmatrix} \mathbf{M}_\phi & 0 \\ 0 & \mathbf{M}_\theta \end{bmatrix} \begin{bmatrix} \ddot{\boldsymbol{\phi}} \\ \ddot{\boldsymbol{\theta}} \end{bmatrix} + \begin{bmatrix} \mathbf{K} & -\mathbf{K} \\ -\mathbf{K} & \mathbf{K} \end{bmatrix} \begin{bmatrix} \boldsymbol{\phi} \\ \boldsymbol{\theta} \end{bmatrix} = \begin{bmatrix} \mathbf{f}_h \\ \mathbf{f}_v \end{bmatrix} + \begin{bmatrix} \mathbf{f}_{d,\phi} \\ \mathbf{f}_{d,\theta} \end{bmatrix} \tag{3.1}$$

where $\mathbf{M}_\phi$ is the inertia matrix of the two-DoF rigid-body model described with independent joint coordinates ϕ_1 and ϕ_3 (Appendix B). The motor inertia matrix is $\mathbf{M}_\theta = \mathrm{diag}(I_{mot1}, I_{mot2})$, while $\mathbf{K} = k_g^2 \times \mathrm{diag}(k_1, k_2)$ is the stiffness matrix with the transmission ratio k_g, and k_1 and k_2 are the corresponding joint stiffness values. Arrays of $\mathbf{f}_h$, $\mathbf{f}_v$ and $\mathbf{f}_d$ linearized forms of the different generalized forces as defined in Chapter 2. This model will be referred to as the four-DoF flexible model in the following.

3.1.3 Stiffness Evaluation. For the analysis in this chapter, we selected the end-point position at $x_E = 0$ m, $y_E = 0.25$ m as a reference configuration (Fig. 3.4 interprets the coordinate system).

The stiffness corresponding to the flexible joints were determined via a series of experiments at the reference configuration. The driven links were blocked in this configuration, while the motors were loaded in different directions and their angular deflections were recorded. The corresponding measurements of motor torque versus motor deflection are shown in Fig. 3.5. The measurements show that the system has

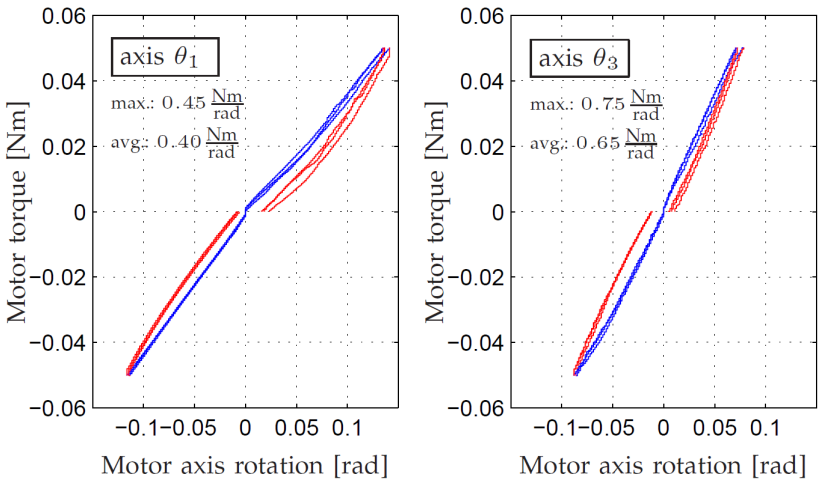

(a) Motor 1 (b) Motor 2

FIGURE 3.5. Measured joint stiffness

non-symmetric stiffness properties. The maximum and average measured stiffness values at the joint level are presented in Table 3.3.

By using the four-DoF flexible model, the non-zero natural frequencies of the system can be obtained as 101 Hz and 131 Hz, when using the maximum measured stiffness value; and 95 Hz and 120 Hz by considering the average measured stiffness values. In our analysis, for providing sufficiently conservative results, we consider the effective model parameters that correspond to the maximum stiffness values.

A second set of measurements is conducted to confirm the validity of the different joint stiffness values. In these experiments a sweeping sinusoidal input torque signal was applied with target frequency of 200 Hz and duration 20 s, and the y-directional displacement of the tip of the device was recorded as output. These experiments were conducted both with and without the human operator grasping the end point.

The measured frequency responses are shown in Fig. 3.6. Within the excitation bandwidth, the chart on the top shows the two natural frequencies of the device

TABLE 3.3. Experimentally measured stiffness values

$k_{1,\text{max}}$	0.45 Nm/rad	$k_{2,\text{max}}$	0.75 Nm/rad
$k_{1,\text{avg}}$	0.40 Nm/rad	$k_{2,\text{avg}}$	0.65 Nm/rad

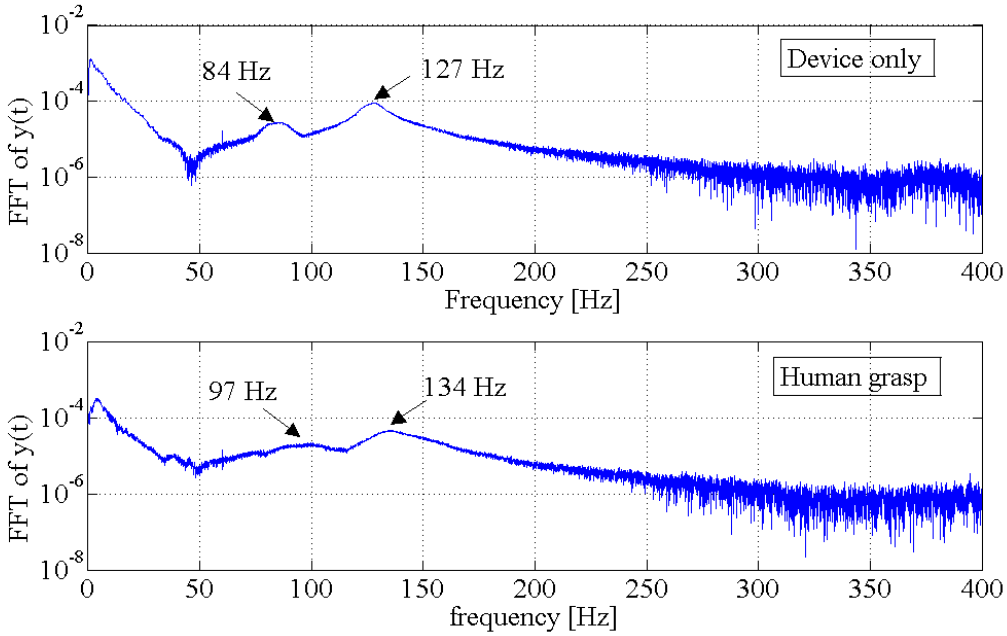

FIGURE 3.6. Measured frequency response of the system, without and with human operator

measured without the human operator interacting with the device. This confirms the localized consideration of stiffness capturing the structural properties of the device. The frequency chart on the bottom shows the effect of the human operator. The measurements without the human operator are in good agreement with the results that can be obtained using the four-DoF model of the system. By firmly grasping the tip of the device, a slight increase could be observed in the characteristic frequencies.

For experimental validation the sampling frequency has to be chosen such that it is sufficiently larger than the lower bound required by the sampling theorem. Based on the measured frequencies it was possible to conclude that the spectral components above 200 Hz in both cases, with or without human operator are negligible. The typical 1 kHz sampling frequency is five times higher. Here we select a slightly lower sampling frequency $f_s = 800$ Hz, which introduces less noise when the velocity of the endpoint is calculated from quantized and sampled position data. Also, the lower the sampling frequency is the smaller the stable domain becomes, and the experimental results are less influenced by temporary saturation of the actuators.

It can be shown that the highest vibration frequency of the controlled system is about 200 Hz (see later in Fig. 3.8), which is half of the Nyquist frequency, which is equal to 400 Hz, proving that the corresponding signal can be properly sampled.

3.2 Bilateral Virtual Wall

For validation of the models proposed in Chapter 2, first we consider interaction with a single bilateral virtual wall. This case corresponds to the situation where the device is in sustained contact with the virtual wall and the wall is already deformed. For such a case, the dynamic behaviour of the proposed two-DoF flexible model in (2.43) can be compared with behaviour of the described haptic device.

3.2.1 Analysis of the Two-DoF Flexible Model. Interacting with a bilateral virtual wall without the human operator's sustained touch can create a worst-case scenario for stability investigation of haptic systems (Diolaiti et al., 2006). Consider dynamic equations in (2.43). In this case $s_h = 0$, and the dissipation due to the device damping is considered. To approximate the device damping, modal damping (Angeles, 2012) can be considered here, which makes it possible to apply modal transformation for further analysis of this model. Then for this case, the dynamic equations in (2.43) can be written as

$$\begin{aligned} &\mathbf{W}_r\ddot{\mathbf{x}} + \mathbf{B}\dot{\mathbf{x}} + \mathbf{K}\mathbf{x} = \mathbf{s}_\nu \;\text{ with }\; \mathbf{B} = r_m\mathbf{W}_r + r_k\mathbf{K}, \\ &\mathbf{W}_r = \begin{bmatrix} m_{e1} & 0 \\ 0 & m_{e2} \end{bmatrix},\; \mathbf{K} = \begin{bmatrix} k_e & -k_e \\ -k_e & k_e \end{bmatrix},\; \mathbf{x} = \begin{bmatrix} x_1 \\ x_2 \end{bmatrix},\; \mathbf{s}_\nu = \begin{bmatrix} 0 \\ \lambda \end{bmatrix}, \end{aligned} \tag{3.2}$$

where the effective masses m_{e1} and m_{e2}, and the effective structural stiffness k_e were defined in Chapter 2; and r_m and r_k corresponding to the coefficients of effective mass and stiffness matrices, respectively. Finally, force $\mathbf{s}_\nu$ describes the discrete-time virtual contact realization. Incorporating the Kelvin-Voigt model in (2.36) for the virtual wall modelling and using the frequently applied backward difference approximation

for velocity estimation, the virtual environment force can be written as

$$\mathbf{s}_\nu = \mathbf{D}\mathbf{X}_j \tag{3.3}$$

where

$$\mathbf{D} = \begin{bmatrix} 0 & 0 & 0 & 0 \\ 0 & -k_p - \frac{k_d}{\Delta t} & 0 & \frac{k_d}{\Delta t} \end{bmatrix}, \text{ and } \mathbf{X}_j = \begin{bmatrix} x_{1j} \\ x_{2j} \\ x_{1_{j-1}} \\ x_{2_{j-1}} \end{bmatrix} \tag{3.4}$$

where $\mathbf{x}_j = \mathbf{x}(t_j)$.

For stability analysis of this system, we construct the discrete map in (2.38) for this model. For this purpose, first modal transformation can be applied to simplify the equations. The two eigenvalues of the undamped system can be obtained as $\lambda_1 = 0$ and $\lambda_2 = k_e \frac{m_{e1}+m_{e2}}{m_{e1}m_{e2}}$. Using these, the corresponding mass normalized eigenvectors can be determined as

$$\mathbf{U} = \begin{bmatrix} \boldsymbol{\nu}_1 & \boldsymbol{\nu}_2 \end{bmatrix} = \begin{bmatrix} \alpha_1 & \frac{\alpha_1}{\alpha_2} \\ \alpha_2 & -\alpha_1\alpha_2 \end{bmatrix} \tag{3.5}$$

where

$$\alpha_1 = \frac{1}{\sqrt{m_{e1} + m_{e2}}}, \quad \text{and} \quad \alpha_2 = \sqrt{\frac{m_{e1}}{m_{e2}}} \tag{3.6}$$

Applying the modal transformation, and denoting the non-zero natural frequency of the model by $\omega_n^2 = \lambda_2$, the dynamic equations in modal coordinates take the form

$$\begin{aligned} \ddot{\xi}_1 + r_m\dot{\xi}_1 &= F_{\xi 1} \\ \ddot{\xi}_2 + (r_m + r_k\omega_n^2)\dot{\xi}_2 + \omega_n^2\xi_2 &= F_{\xi 2} \end{aligned} \tag{3.7}$$

where ξ_1 and ξ_2 are the modal coordinates, and $F_{\xi 1}$ and $F_{\xi 2}$ are the virtual interaction force components associated with these coordinates. In order to form the discrete mapping, as discussed in Chapter 2, the solution at $t = t_{j+1}$ can be obtained in the

piecewise linear form based on the solution at $t = t_j$ as

$$\begin{aligned}
\xi_{1_{j+1}} =& \xi_{1_j} - \frac{1 - e^{-r_m \Delta t}}{r_m} \dot{\xi}_{1_j} + (\frac{e^{r_m \Delta t} - 1}{r_m^2} + \frac{1}{r_m}) F_{\xi 1} \\
\xi_{2_{j+1}} =& (e^{-\zeta \Omega_n} \cos \Omega_d + \frac{\zeta \omega_n e^{-\zeta \Omega_n}}{\omega_d} \sin \Omega_d) \xi_{2_j} + \frac{e^{-\zeta \Omega_n} \sin \Omega_d}{\omega_d} \dot{\xi}_{2_j} + \\
& (\frac{e^{-\zeta \Omega_n} \cos \Omega_d}{\omega_n^2} - \frac{\zeta e^{-\zeta \Omega_n} \sin \Omega_d}{\omega_n \omega_d} + \frac{1}{\omega_n^2}) F_{\xi 2}
\end{aligned} \tag{3.8}$$

where $\Omega_d = \omega_n \Delta t \sqrt{1 - \zeta^2}$, $\zeta = \frac{r_m}{2\omega_n} + \frac{r_k \omega_n}{2}$, and

$$\begin{bmatrix} F_{\xi 1} \\ F_{\xi 2} \end{bmatrix} = \begin{bmatrix} \alpha_1 \alpha_2 (-p - \frac{d}{\Delta t}) & -\alpha_1^2 \alpha_2 (-p - \frac{d}{\Delta t}) & \alpha_2 \alpha_2 \frac{d}{\Delta t} & \alpha_1^2 \alpha_2 \frac{d}{\Delta t} \\ \alpha_1 (-p - \frac{d}{\Delta t}) & -\alpha_1^2 (-p - \frac{d}{\Delta t}) & \alpha_1 \frac{d}{\Delta t} & -\alpha_1^2 \frac{d}{\Delta t} \end{bmatrix} \begin{bmatrix} \xi_{1_j} \\ \xi_{2_j} \\ \xi_{1_{j-1}} \\ \xi_{2_{j-1}} \end{bmatrix} \tag{3.9}$$

Substituting (3.9) in (3.8) forms a decoupled set of equations with constant right-hand-side within consecutive sampling periods. Following the process described in Chapter 2, the transition matrix of the system, $\mathbf{L}$, can be constructed, while the discrete state of the system in terms of modal variables is $\mathbf{Z}_j = [\dot{\xi}_{1_j} \Delta t,\ \dot{\xi}_{2_j} \Delta t,\ \xi_{1_j},\ \xi_{2_j},\ \xi_{1_{j-1}},\ \xi_{2_{j-1}}]^{\mathrm{T}}$. The resulting 6×6 transition matrix $\mathbf{L}$ has five non-zero and one zero eigenvalues. The zero eigenvalue corresponds to the redundant element in the state vector which is added due to the modal transformation. The transition matrix in this case is relatively complex and cannot be presented in parametric form here. However, based on the process explained in Chapter 2, the transition matrix can be constructed numerically.

The eigenvalues of this mapping must lie within the unit disk of the complex plane to ensure stability. The magnitude of the largest real or complex eigenvalue primarily characterizes the decaying of the transients. Stability boundary of the system in (3.2) can be numerically obtained by plotting the boundary where magnitude of the largest eigenvalue of the transition matrix $\mathbf{L}$ must be equal or less than unity.

Consider the reference configuration described in Sec.3.1.3. At this configuration, the effective parameters of the two-DoF flexible model in (3.2) are listed in Table 3.4. We assume that the structural damping of the device is proportional to the stiffness matrix of the system only, i.e., $r_m = 0$. For the case where $r_k = 0.0012$, which corresponds to the damping ratio of $\zeta = 0.5$, the stability boundary can be obtained as shown in Fig. 3.7 by the bold solid line.

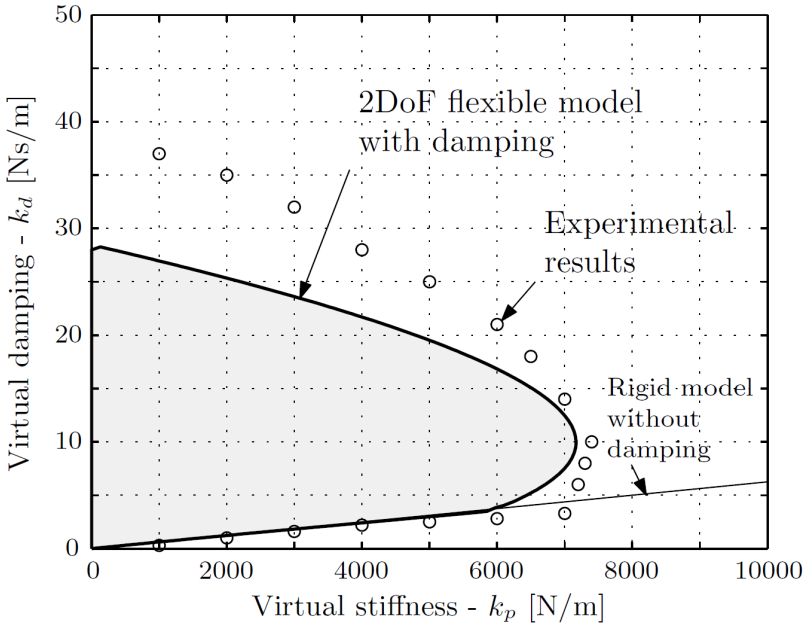

FIGURE 3.7. Bilateral wall without the human operator

3.2.2 Experimental Analysis. Experimental stability analysis is conducted for the validation of the numerical results. The experimental device together with the virtual wall is shown in Fig. 3.4. In this experiment, the virtual wall was located at the reference location. For each experiment, a small perturbation was applied to the end-point of the device to overcome the effect of dry friction and deviate the

TABLE 3.4. Effective model parameters

m_{e1}	0.2616 kg	m_{e2}	0.0254 kg
k_e	15620 N/m	Δt	0.0025 sec

end-point from equilibrium. At each measurement point, the virtual stiffness was selected and the stability boundary was measured by changing the virtual damping values. For each selected virtual stiffness, two values for virtual damping were used which correspond to the lower and upper stability boundaries. The behaviour of the system in the regions corresponding to the low and high values of virtual damping was different. The resultant measured stability boundary in the space of virtual environment parameters is shown in Fig. 3.7 via indicating the measurement points by circles. Measuring the points on the tip of the boundary were more challenging. For virtual stiffness values higher than 7000 N/m, the stability boundary were measured via recording the stable virtual stiffness corresponding to a selected values of virtual damping.

Comparing the experimentally measured stability boundary with the one obtained via the two-DoF flexible model, it can be seen that they are in good agreement in the domain of low virtual damping. However, in the high virtual damping region the boundary obtained based on the model does not follow the experimental measurements and the stable domain is smaller.

To understand the behaviour of the system in this region, the characteristic vibration frequency of the system along the stability boundary can be investigated using the two-DoF flexible model. This frequency can be obtained via the angle α of the complex conjugate pairs corresponding to the eigenvalues of the transition matrix $\mathbf{L}$ with largest magnitude that leaves the unit disk on the complex plane (Kuo, 1981; Stepan, 2001). This frequency is equal to $\alpha/\Delta t$. There are also higher frequency components due to periodicity of the eigenvalues with 2π. Due to this, there are higher components having the same frequencies plus the integer multiple of the sampling frequency. These higher components are usually damped out by the internal damping of the mechanism.

The resulting characteristic vibration frequency of the system along the stability boundary are shown in Fig. 3.8. This reveals that in the domain of low virtual damping, the lose of stability is accompanied with low-frequency vibrations, while in the

high virtual damping region, this frequency increases drastically. At the intersection of the boundaries there are two dominant frequencies which are indicated by circles on the frequency chart.

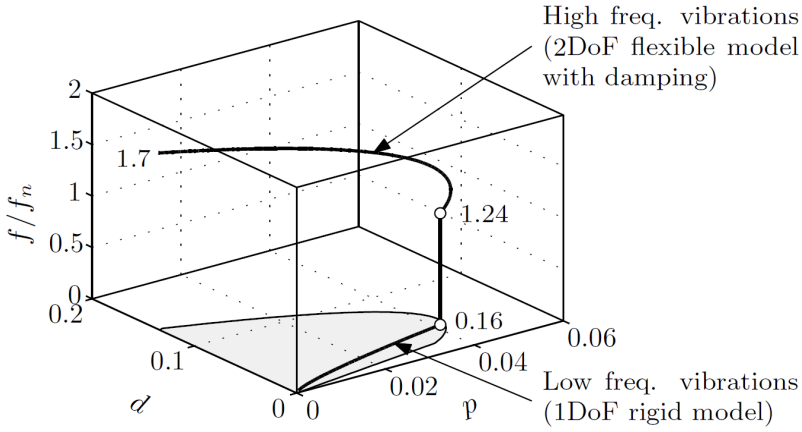

FIGURE 3.8. Vibration frequencies at lose of stability

We note that the structural dissipation is a function of the characteristic vibration frequency of the system. This study of characteristic frequency of this system shows that the modelling of dissipation is not trivial, and the employed modal damping cannot capture the complex and nonlinear behaviour of the structural damping. This can explain the difference between the experimental and numerical stability boundaries in Fig. 3.7 in the domain of high virtual damping.

As shown in Fig. 3.8 the characteristic vibration frequency along the stability boundary in the low virtual damping domain has small values. The behaviour of the system in the experimental analysis also confirms the low frequency vibration of the system in this region. Based on this observation, it can be considered that the system can be well representative with rigid-body model in this domain and the structural flexibility of the device cannot be excited. For more detailed investigation, the stability analysis incorporating the rigid-body model in (2.42) will be conducted, and the results can be compared with the experimental measurements.

3.2.3 Analysis of the Single-DoF Rigid-Body Model. As discussed in Chapter 2, when structural flexibility is not excited, dynamic behaviour of a haptic

system may be described via the single-DoF rigid-body model in (2.42). For the analysis of this model, interaction with a bilateral virtual wall is considered without human operator's sustained touch, where $s_h = 0$. For this model, the physical dissipation due to device damping can be approximated via considering a linear viscoelastic damping element b in the rendered direction, where $s_{dr} = -b\dot{x}$. Employing the same model described earlier in this chapter for the realization of the virtual wall, the dynamic equation in (2.42) can be written in the piecewise linear form as

$$\begin{aligned} & m_e\ddot{x}(t) + b\dot{x}(t) = \lambda \ , \quad t \in [t_j, t_{j+1}) \\ & \text{with} \quad \lambda = (-k_p - \frac{k_d}{\Delta t})\ x_j + \frac{k_d}{\Delta t}\ x_{j-1} \end{aligned} \tag{3.10}$$

For stability analysis of this model, constructing the discrete map in (2.38) can be implemented in closed-form. For this purpose dynamic equations in (3.10) can be represented with dimensionless coefficients as

$$x''(T) + \beta x'(T) = (-p - d)x_j + d\ x_{j-1} \tag{3.11}$$

where the prime denotes differentiation with respect to the dimensionless time $T = t/\Delta t$. The dimensionless virtual stiffness and damping $p = k_p\Delta t^2/m_e$ and $d = k_d\Delta t/m_e$, arise naturally also in the piecewise solution of (3.10). To construct the solution of (3.11) for the given generic sampling interval, one can consider the state space representation of (3.11) as

$$\mathbf{X}'(T) = \mathbf{C}\mathbf{X}(T) + \mathbf{D}\mathbf{u}_j, \quad T \in [T_j, T_{j+1}), \quad n = 0, 1, 2, ... \tag{3.12}$$

where $T_j = j\Delta(t)$, and

$$\mathbf{X}(T) = \begin{bmatrix} x(T) \\ x'(T) \end{bmatrix}, \quad \mathbf{u}_j = \begin{bmatrix} x_j \\ x_{j-1} \end{bmatrix} \tag{3.13}$$

and the coefficient matrices are

$$\mathbf{C} = \begin{bmatrix} 0 & 1 \\ 0 & -\beta \end{bmatrix}, \quad \mathbf{D} = \begin{bmatrix} 0 & 0 \\ (-p-d) & d \end{bmatrix} \tag{3.14}$$

Considering the solution at $T = T_j$ as an initial condition, the general solution at the end of time interval $T = T_{j+1}$ can be written in the form

$$\mathbf{X}_{j+1} = e^{\mathbf{C}\Delta T}\mathbf{X}_j + \int_0^T e^{\mathbf{C}\tau} d\tau \mathbf{D}\mathbf{u}_j \tag{3.15}$$

Then, by selecting the discrete state vector $\mathbf{z}_j = [x'_j,\, x_j,\, x_{j-1}]^{\mathrm{T}}$ and using the shorthand notation $\varepsilon = (1 - e^{-\beta})/\beta$, the discrete mapping can be obtained as

$$\mathbf{z}_{j+1} = \mathbf{L}\,\mathbf{z}_j \quad \text{with}$$

$$\mathbf{L} = \begin{bmatrix} 1-\varepsilon\beta & -\varepsilon(p+d) & \varepsilon d \\ \varepsilon & 1 - \dfrac{1-\varepsilon}{\beta}(p+d) & \dfrac{1-\varepsilon}{\beta} d \\ 0 & 1 & 0 \end{bmatrix} \tag{3.16}$$

Using this transition matrix, the stability boundaries can be obtained for any value of β. The stability boundary associated with $\beta \to 0$ is shown in Fig. 3.9. Stability boundary corresponding to the two-DoF flexible model in (3.2) can also be obtained for the case with zero structural damping, i.e., $r_m = 0$, $r_k = 0$. The resulting boundary is also illustrated in Fig. 3.9.

It is illustrated in this figure that in the case of the flexible model, the system can lose its stability well inside the stable domain that is obtained based on the rigid-body model. The lower bound of the stable domain obtained using the rigid-body model is also shown in Fig. 3.7 by a thin solid line. It is interesting to see that in the low virtual damping domain, both the experimental measurements and the numerical results using the two-DoF flexible model follow this line. This can also be explained via the low characteristic vibration frequency of the system in this region. Therefore, in this range of virtual environment parameters, the structural flexibility of the physical device is not excited and the system can be approximated by the single-Dof rigid-body model.

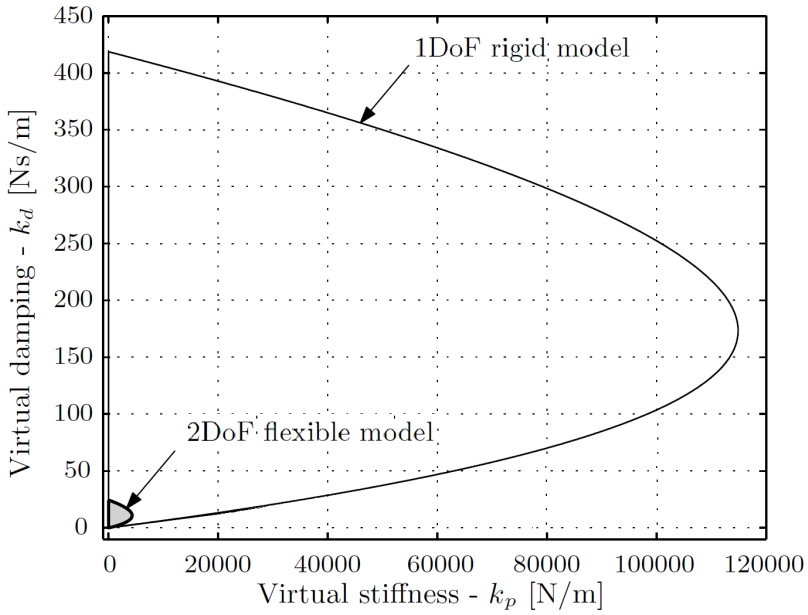

FIGURE 3.9. Numerical stability boundaries corresponding to the rigid-body and flexible models

We can further investigate the characteristic dynamics of the system in different regions of the space of virtual environment parameters. For this purpose, the behaviour of the system at different points of this parameter space is simulated via the two-DoF flexible model. These pints are shown in the first chart in Fig. 3.10. The resulting behaviours are presented in the second chart of Fig. 3.10. In these charts, x_1 and x_2 correspond to the coordinates associated with the effective masses. Several points are selected inside and outside of the resulting stable domain. It can be seen that from point B to A (inside to outside of the stable domain in high virtual damping region), the smaller mass oscillates relative to the larger mass with an increasing amplitude. To show high-frequency oscillation of m_{e2} at point B, a magnification factor of five was applied. The behaviour of the system at points C and D located in the low virtual damping domain is different. In this region, both x_1 and x_2 show oscillatory motion at the same frequency and the behaviour of the system can be described by a rigid-body model. Point E is located at the point corresponding to the lowest spectral radius of the transition matrix, which represents the fastest decaying oscillation. This can be an optimum operational point of the system for highest fidelity.

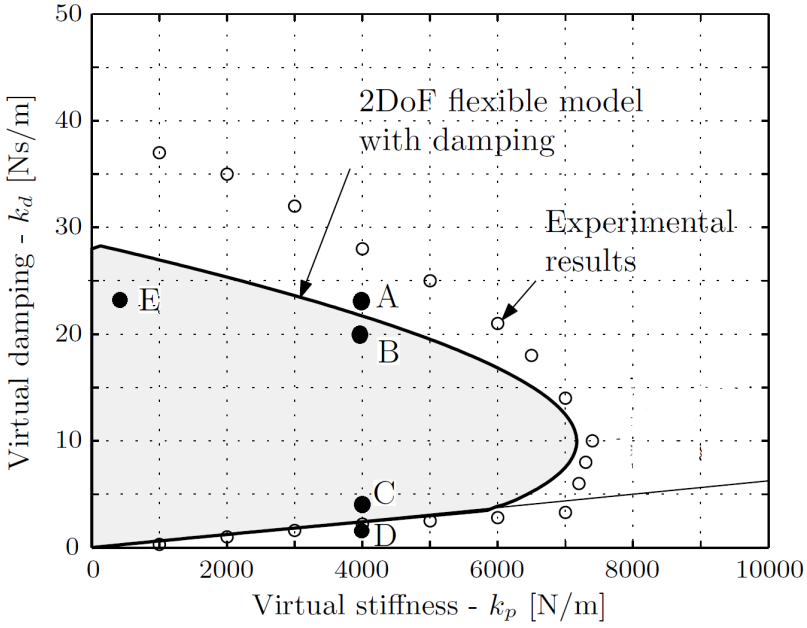

(a) Experimental measurements

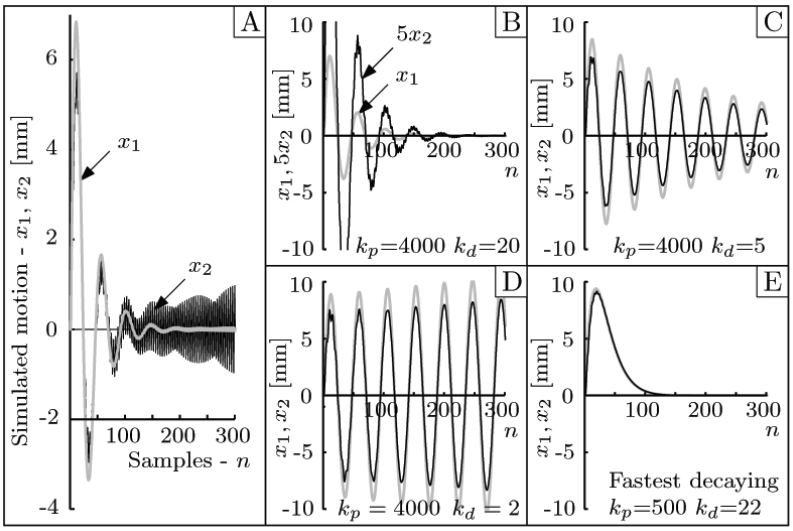

(b) Simulated model behaviour

FIGURE 3.10. Characteristic dynamics at different points of the stability chart

3.2.4 Filtering. It is common in haptic applications to filter the measured quantized and sampled signals. This, however, can also seriously limit the performance. Filtering can also be used to reduce the effects of structural flexibility. In this

case, the rigid-body model presented in Chapter 2 can be representative for dynamic behaviour.

To investigate the effect of filtering, we applied a 2nd-order Butterworth filter with 20 Hz cutoff frequency as a classical low-pass filter. To minimize the introduced time delay the filter is only used in the velocity estimation, while the position feedback is left unfiltered.

The normalized transfer function of the second-order Butterworth filter is

$$G(s) = G_0/B_n(\frac{s}{\omega_c}), \text{ with } B_n(s) = s^2 + \sqrt{2}s + 1 \tag{3.17}$$

where G_0 is the steady state gain and ω_c is the cut-off frequency. In order to use the filter in the digital controller it has to be discretized. This is often carried out by using the Tustin transformation $s = \frac{2}{\Delta t}(z-1)/(z+1)$ which leads to the discrete time filter

$$G_d(z) = \frac{n_0 z^2 + n_1 z + n_2}{d_0 z^2 + d_1 z + d_2} \tag{3.18}$$

where,

$$\begin{gathered} 2n_0 = n_1 = 2n_2 = G_0 \frac{\Omega_c^2}{\Omega_c^2 + 4\zeta\Omega_c + 4} \\ d_0 = 1\,,\ d_1 = \frac{2\,(\Omega_c^2 - 4)}{\Omega_c^2 + 4\zeta\Omega_c + 4}\,,\ d_2 = \frac{\Omega_c^2 - 4\zeta\Omega_c + 4}{\Omega_c^2 + 4\zeta\Omega_c + 4}\,. \end{gathered} \tag{3.19}$$

and $\Omega_c = \omega_c \Delta t$ and $\zeta = 1/\sqrt{2}$. This filter is applied to the measured position in the rendered direction and the corresponding velocity is calculated via backward differentiation subsequently. The force feedback of the virtual spring is based on the unfiltered position. In order to focus on the effects of filtering, effects of physical damping is eliminated in this model. With these assumptions, the dynamic equation in (3.11) can be written as

$$x''(T) = -px_j - d(\varsigma_j - \varsigma_{j-1})\,, \quad T \in [j, j+1)\,, \tag{3.20}$$

where ς denotes the filtered position. The solution and the filtered position at $T = j+1$ is given by

$$\begin{aligned} x'_{j+1} &= -px_j - d(\varsigma_j - \varsigma_{j-1}) + x'_j \\ x_{j+1} &= \frac{1}{2}\left(-px_j - d(\varsigma_j - \varsigma_{j-1})\right) + x'_j + x_j \\ d_0\,\varsigma_{j+1} &= n_0\,x_{j+1} + n_1 x_j + n_2 x_{j-1} - d_1\varsigma_j - d_2\varsigma_{j-1} \end{aligned} \tag{3.21}$$

Considering that $d_0 = 1$ and introducing the discrete state vector as $\mathbf{z}_j = [x'_j,\ x_j,\ x_{j-1},\ \varsigma_j,\ \varsigma_{j-1}]^{\mathrm{T}}$, the transition matrix corresponding to the discreet mapping in (2.38) has the form

$$\mathbf{L} = \begin{bmatrix} 1 & -p & 0 & -d & d \\ 1 & 1-\frac{p}{2} & 0 & -\frac{d}{2} & \frac{d}{2} \\ 0 & 1 & 0 & 0 & 0 \\ n_0 & n_0\left(1-\frac{p}{2}\right)+n_1 & n_2 & -n_0\frac{d}{2}-d_1 & \frac{d}{2}n_0-d_2 \\ 0 & 0 & 0 & 1 & 0 \end{bmatrix}. \tag{3.22}$$

The resultant stability boundary is shown in Fig. 3.11 by solid line. Incorporating the same filter, the stability boundary can be measured experimentally as it is illustrated in Fig. 3.11. It can be seen that the proposed rigid-body model is representative in this case. However, since the effects of physical damping are not considered in the analysis, the stable domain is smaller than the one measured experimentally. Compared to the unfiltered results (see in Fig. 3.7) it can readily be seen that the stable domain of virtual environment parameters is considerably smaller. Filtering made it possible to achieve higher virtual damping at low-stiffness values, but it decreased the maximum stable virtual stiffness.

3.2.5 Effect of Quantization. Quantization can limit the haptic performance. It is important to note that the presented experimental results are not corrupted by the effect of quantization. For the experimental device considered in this work, the quantization limit can be estimated as $k_{p\,max} = 2C/\Delta_p \approx 26700\,\mathrm{N/m}$ based on (Diolaiti et al., 2006). Comparing this limit with the maximum stable virtual stiffness achieved based on the flexible model of the device in Fig. 3.7, it can be seen

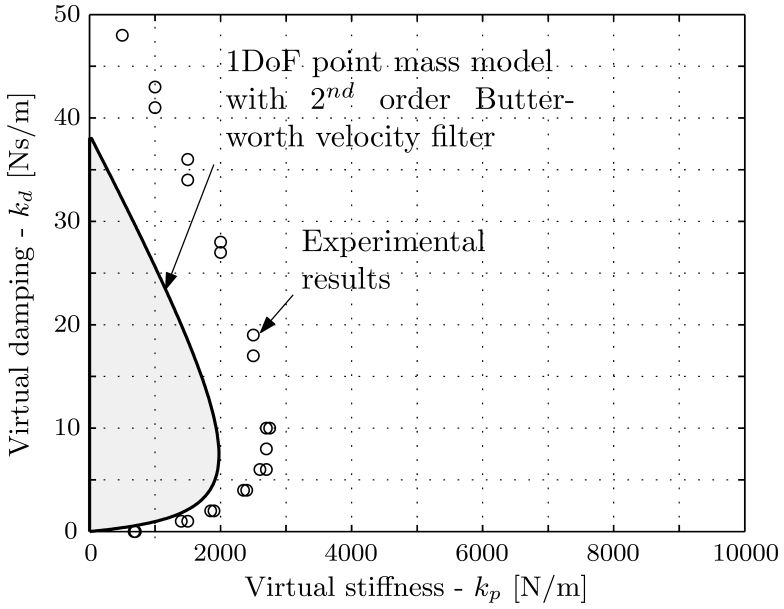

FIGURE 3.11. Effect of filtering

that the system is expected to lose stability well before quantization effects could be observed. In practice, quantization limit can only be reached when a higher sampling frequency is considered, in order to prevent actuator saturation. To experimentally verify this observation, we increased the sampling frequency to 10 kHz which made it possible to set higher virtual stiffness values than in the experiments reported above. With this, the maximum renderable stiffness before experiencing limit cycle oscillations due to quantization was found at $k_p = 50$ KN/m. This limit is clearly outside of the reachable impedance range in our experiments due to the presence of structural flexibility.

3.3 Unilateral Wall

Understanding the effect of the human operator is important in experimental validation with real operating conditions. Another set of experiments were conducted to study effects of human operator on haptic system dynamics in more detail. In this case, a unilateral virtual wall is considered in the experiments. A human operator was interacting with this virtual wall by touching the wall and trying to keep the

contact sustained. Whenever this was not possible the measurements were considered unstable. These experiments are summarized and compared to the previous results in Fig. 3.12. The points of the measured stability boundary are shown by solid squares. In this set of experiments two subjects participated. Each experimental measurement point was obtained via $4-5$ trials. The deviations due to different subjects and their strength of grasp are indicated by bars around these points.

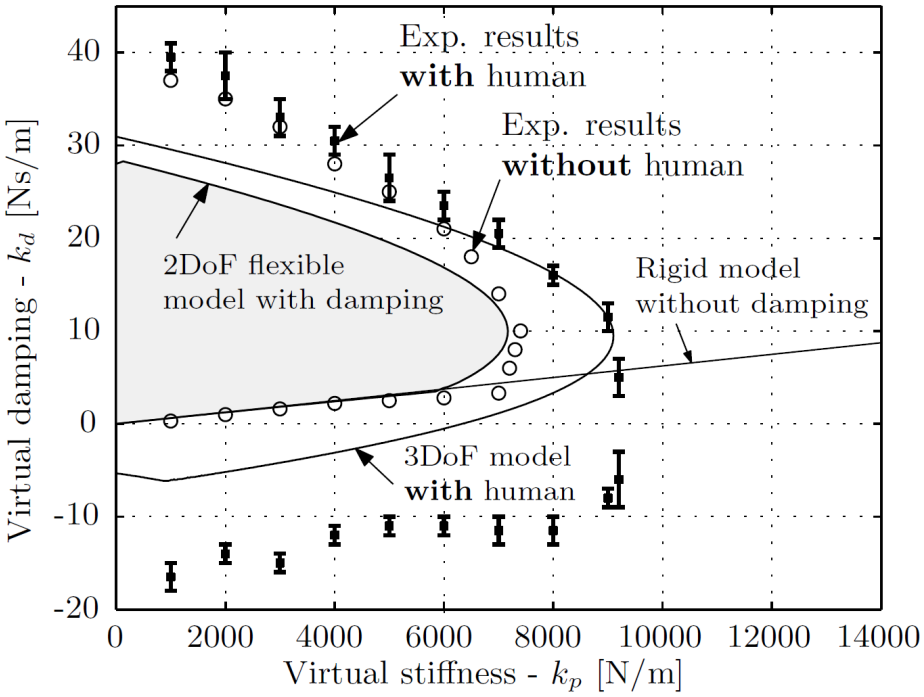

FIGURE 3.12. Effect of the human operator

It can be seen, that the human operator can stabilize the virtual contact. The experimentally obtained stability chart is considerably larger compared to the case without human. A significant qualitative difference is that the lower bound is located in the negative virtual damping domain and it is no longer linear. However, we can also see that the nature of the dynamic behaviour is reasonably well-captured by the two-DoF flexible model. The shapes of the two areas are very similar. Also, the two-DoF model gives more conservative results as the human operator enlarges the stable domain via adding more damping and also probably actively compensating for

instabilities. To study these effects, a simple model of human operator will be defined here and the resulting stability chart will be compared to the experimental results.

3.3.1 Human Model. The force exerted by the human operator is often characterized by series of linear impedance elements in the rendered direction (Hogan, 1989; Haddadi, 2011; Speich et al., 2005). To include the effect of human operator in the model, an inertia element is considered representing the hand/arm model which is attached to the inertia reference frame through the stiffness and damping representation of the hand/arm. This model is linked to the reference point of the haptic device via stiffness and damping elements representing the grasp properties. This five parameter arm/hand linear impedance model together with the two-DoF flexible model of the device is shown in Fig. 3.13. This model of the human operator's hand/arm introduces one additional DoF which together with the device leads to a three-DoF haptic system model. The dynamic equations of this model can be written as

$$\mathbf{W}_r\ddot{\mathbf{x}} + \mathbf{B}\dot{\mathbf{x}} + \mathbf{K}\mathbf{x} = \mathbf{s}_\nu \tag{3.23}$$

where,

$$\mathbf{W}_r = \begin{bmatrix} m_{e1} & 0 & 0 \\ 0 & m_{e2} & 0 \\ 0 & 0 & m_h \end{bmatrix}, \ \mathbf{B} = \begin{bmatrix} b+b_c & -b & -b_c \\ -b & b & 0 \\ -b_c & 0 & b_c+b_h \end{bmatrix}, \ \mathbf{K} = \begin{bmatrix} k_e+k_c & -k_e & -k_c \\ -k_e & k_e & 0 \\ -k_c & 0 & k_c+k_h \end{bmatrix} \tag{3.24}$$

and $\mathbf{x} = [x_1, x_2, x_h]^{\mathrm{T}}$, $\mathbf{s}_\nu = [0, \lambda, 0]^{\mathrm{T}}$, and m_h, k_h and b_h correspond to the human hand/arm mass, stiffness and damping properties, k_c and b_c are associated with the stiffness and damping properties of the grasp. The damping effect of the device is represented by b. Stability analysis of this model can be carried out similar to what was explained for the two-DoF flexible model in (3.2). The parameters of the arm are considered as $m_h = 0.8$ kg, $k_h = 580$ N/m and $b_h = 5.5$ Ns/m. these parameters give typical representation of human hand/arm impedance as reported in (Hogan, 1989). The parameters of the firm grasp of human in this experiment

is selected as $k_c = 10000$ N/m and $bc = 5$ Ns/m. Ref. (Fu and Cavusoglu, 2012) provides similar human model parameters for the grasp except the grip stiffness k_c. The value selected here for k_c is based on the study reported in (Perez-Gonzalez et al., 2013), where the grip stiffness is directly measured at the phalanges of the human hand at grip forces in the range of $6 - 7$N. The grip stiffness is proportional to the grip force (at the distal phalanges) and has intrinsic and reflexive components, where the reflexive part involves the time delay of the human sensory system (Perez-Gonzalez et al., 2013). These additional time delay effects are not included in the model here, but they can also have important influence on the dynamics of the haptic system. In addition to these passive impedance parameters of the human-machine interconnection, a damping coefficient of 7.5% is assumed for modelling the effect of the damping of the structural dynamics of the haptic device.

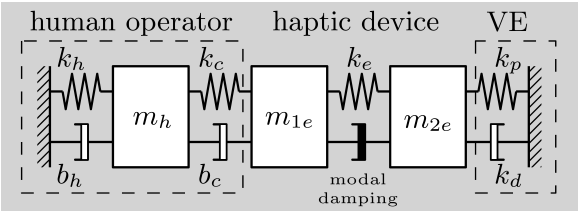

FIGURE 3.13. Illustration of a haptic system model using a one-DoF human operator representation

The resulting stability chart is shown in Fig. 3.12 and referred to as the three-DoF model with human grasp.

The results presented suggest that the passive arm and grasp dynamics of the human operator has a relatively small effect on the stability of the haptic device in the presence of structural flexibility.

The larger stable domain is mainly the consequence of the assumed increased structural dissipation and the active human operator behaviour to compensate for instabilities. In case of high virtual damping, the experimental results with and without the human operator are very close. For low virtual damping values the difference is significant. This is an indication that the human operator has different dynamics

in these regions. The subjects in the experiments could shape their impedance characteristics such that they stabilized the interaction with an otherwise highly unstable virtual wall. This is the case when a human is interacting with low-frequency instabilities. However, human cannot react to the vibrations at high frequency. In the high-frequency region, the difference between the numerical results and experimental measurements can be due to the damping model used to represent the physical dissipation of the haptic device. It is important to note that in this high-frequency region, nonlinear models for damping may better match the experimental measurements. Based on these observations one may conclude that the human operator is not necessarily passive in all the possible interaction scenarios, which is also supported by observations in (Diolaiti et al., 2006). In the lower frequency range, the human can actively compensate for instabilities and have variable and/or non-linear impedance. While the passive physical damping of the operator is important, it cannot explain the stable operation at high negative virtual damping values. The operator must compensate actively in that range. By analyzing the effect of human grasp on two different haptic devices, it was found in (Speich et al., 2005) that the human-machine interconnection might change the system dynamics. It is concluded that some devices are not sensitive to the human effects, while in other cases an extra resonant peak may appear in the system response. In our experiments we could observe a similar behaviour when out-of-plane forces were applied by the human operator which pre-stressed the elements of the capstan drive. This may indicate nonlinear spring characteristics and/or unmodelled, out-of-plane flexibility which cannot be directly measured until the device is built.

(Hulin et al., 2008) concludes that all the three elements of a linear mass-spring-damper human model has stabilizing effects in impedance type haptic devices. In fact, as it will be shown later, the stiffness of the operator slightly reduces the physically meaningful (positive) domain of virtual wall parameters. This reduction of stable domain is compensated by the damping and the added effective mass of the human operator.

As we can also conclude from the analyses in this chapter, the human operator can have different dynamics in the space of virtual environment parameters. The human operator can be active and change his/her impedance to stabilize an unstable virtual interaction, while cannot react to high-frequency vibration.

Therefore, new devices require proper structural design, and sufficient conservatism is required in the analysis to avoid unexpected instability due to interaction with the human operator.

CHAPTER 4

Haptic System Analysis

Two simplified single-DoF models were developed in Chapter 2 for haptic interaction with a single rendered direction. One when rigid-body model is considered and the other when structural flexibility is considered. In this chapter, these simplified models are used for more detailed parametric analysis. Closed-form conditions are defined for the stability of the haptic systems as functions of the system parameters. Stability results in the literature of haptic rendering are then reviewed for comparison with the conditions derived in this chapter.

4.1 Rigid-Body Model

The dynamic equation of the rigid-body model was developed in Chapter 2 as

$$m_e\ddot{x} = s_h + s_{dr} + \lambda \tag{4.1}$$

As mentioned before in Chapter 3, considering the case where the human operator is not in sustained touch with the virtual environment brings conservativeness into the results, which corresponds to the worst-case scenario. In this model one can consider only the dissipation from the human force representation, which can be lumped together with the representation of the device damping. Considering viscous damping leads to

$$s_h + s_{dr} = -b\dot{x} \tag{4.2}$$

With this assumption, the model in (4.1) forms a mass-damper model. This is the model most investigated in the literature. For example, (Colgate and Schenkel, 1997) provides analytical conditions for the passivity of such a model and compares them to numerically obtained stability results. We note that here we obtained the model as a subcase of the general model framework. The terms of this simple model are connected to the physical parameters of the overall haptic system. Employing representation (2.36) for the virtual interaction force, the dynamic equation in the rendered direction can be written in the piecewise linear form

$$\begin{aligned} m_e\ddot{x} + b\dot{x} = \lambda, \ , \quad t \in [t_j, t_{j+1}) \\ \text{with} \quad \lambda = (-k_p - \frac{k_d}{\Delta t})\, x_j + \frac{k_d}{\Delta t}\, x_{j-1} \end{aligned} \tag{4.3}$$

This model was analyzed in Chapter 3. The transition matrix $\mathbf{L}$ corresponding to the discrete mapping is developed in (3.16). To ensure stability, as discussed in Chapter 2, the spectral radius of the transition matrix must be equal or less than unity, i.e., all the eigenvalues must lie inside the unit disk of the complex plane. To obtain stability conditions in closed-form, it is advantageous to map the unit disk into the left half of the complex plane via the Moebius (bilinear) transformation. This way the Routh-Hurwitz criterion (Appendix A) can be directly applied to the transformed characteristic polynomial to analyze stability. Based on that and by using the Moebius transformation, the transformed characteristic polynomial of the transition matrix $\mathbf{L}$ can be obtained as

$$p_3(\sigma) = \sum_{i=0}^{3} \mu_i \sigma^i \tag{4.4}$$

where,

$$\begin{aligned} \mu_3 &= \varepsilon\beta p \\ \mu_2 &= 2\varepsilon\beta d - 2\varepsilon p - \varepsilon\beta p + 2p + 2\varepsilon\beta^2 \\ \mu_1 &= 4d - \varepsilon\beta p + 4\beta - 4\varepsilon\beta d - 4\varepsilon d \\ \mu_0 &= 2\varepsilon p - 2\varepsilon\beta^2 + 2\varepsilon\beta d + \varepsilon\beta p + 4\varepsilon d + 4\beta - 4d - 2p \end{aligned} \tag{4.5}$$

The Routh-Hurwitz criterion can be directly applied to this polynomial. Based on that to ensure stability, several conditions have to be simultaneously satisfied as

$$\mu_i > 0, \quad i = 1, 2, 3, \text{ and } \Delta_2 = \mu_1\mu_2 - \mu_3\mu_0 > 0 \tag{4.6}$$

which results in the requirement of the dimensionless virtual stiffness to be positive, and the stable region of virtual wall parameters are bounded by a domain which in the $p - d$ plane can be described in the form

$$(1-\varepsilon)pd + \varepsilon\beta d^2 + \beta p + \frac{\varepsilon\beta^2(\varepsilon + \varepsilon\beta - 2)}{\varepsilon + \varepsilon\beta - 1}d - \frac{\varepsilon\beta^3}{\varepsilon + \varepsilon\beta - 1} = 0 \tag{4.7}$$

Considering the $p-d$ plane, the general equation of a conic section can be written as

$$a_{pp}p^2 + 2a_{pd}pd + a_{dd}d^2 + 2b_pp + 2b_dd + c = 0 \tag{4.8}$$

and if condition $a_{pd}^2 - a_{pp}a_{dd} > 0$ is satisfied, then (4.8) is a hyperbola. For the equation in (4.7), where $a_{pp} = 0$, this condition is true for any a_{pd} values. This shows that the domain bounded by (4.7) is a hyperbola. Based in (4.7) and by expressing p, after some simplifications, one can arrive to

$$0 < p < \frac{\varepsilon\beta(d+\beta)(\beta + d(1-\varepsilon+\varepsilon\beta))}{(\varepsilon d - d - \beta)(1-\varepsilon+\varepsilon\beta)} \tag{4.9}$$

and the maximum point of this hyperbola boundary is at

$$p_{max} = \frac{(1+\beta)^2\beta^2\varepsilon^2/(\varepsilon+\varepsilon\beta-1)}{\varepsilon+\varepsilon\beta-1+2\sqrt{\beta(\varepsilon+\varepsilon\beta-1)}} \tag{4.10}$$

$$d(p_{max}) = \frac{\beta(1-\varepsilon\beta)}{\varepsilon+\varepsilon\beta-1+\varepsilon\sqrt{\beta(\varepsilon+\varepsilon\beta-1)}} \tag{4.11}$$

For low virtual wall impedances the stable domain is approximately bounded from below by a tangent line at $p = 0$ as

$$d = \frac{\varepsilon\beta(1+\beta)}{(\varepsilon+\varepsilon\beta-1)p - \beta} \tag{4.12}$$

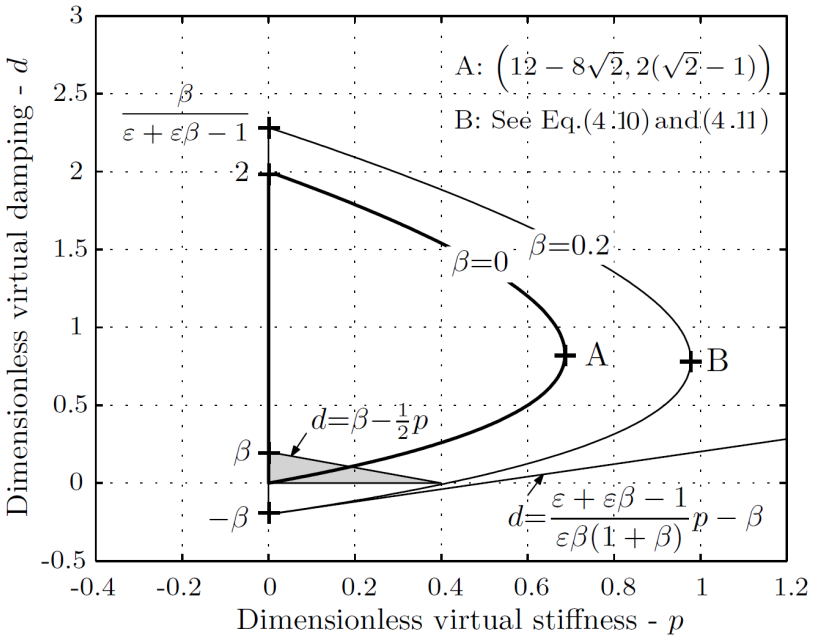

FIGURE 4.1. Stability charts: lumped mass model with damping

As an example, the corresponding stability chart with $\beta = 0$ and $\beta = 0.2$ are given in Fig. 4.1. For the case of $\beta = 0.2$, the rightmost point of this boundary, indicated by point B, and the tangent line at low impedances is also shown in the figure.

When β tends to zero, the corresponding transition matrix can be obtained by applying the limit cases as

$$\lim_{\beta\to 0}\varepsilon = 1 \text{ and } \lim_{\beta\to 0}\frac{1-\varepsilon}{\beta} = \frac{1}{2} \tag{4.13}$$

in (3.16). This leads to the derivation of the condition corresponding to the physically undamped model in (2.42) with $s_{dr} = 0$, as

$$0 < p < \frac{2d}{d+2}(2-d) \tag{4.14}$$

Searching for the rightmost point of this boundary one can obtain the maximum dimensionless virtual stiffness as $p_{max} = 12 - 8\sqrt{2}$ at $d(p_{max}) = 2(\sqrt{2}-1)$ (see point A in Fig. 4.1), and for $p = 0$, the maximum virtual damping as $d_{max} = 2$.

It should be noted that the stability conditions and the critical points of the stability boundaries derived above in equations (4.9) to (4.14) are in terms of dimensionless parameters of the virtual wall. However, for practical application, these conditions can be obtained in terms of physical parameters by substituting he definition of these dimensionless parameters described in Chapter 3. The resulting stability conditions embed mechanical properties of the haptic system, which are obtained from the overall dynamics representation of the whole system.

One can compare the resulting stability conditions with the passivity condition in the haptic system literature. Consider the passivity condition proposed in (Colgate and Schenkel, 1997) as

$$d < \beta - \frac{1}{2}p \quad \Leftrightarrow \quad k_d < b - \frac{k_p \Delta t}{2} \tag{4.15}$$

This domain, where the passivity requirement is satisfied, is shown in light gray area in Fig. 4.1. Compared to the presented maximums at points A and B, the rightmost point of the shaded domain i.e., $p = 2\beta$, $d = 0$, indicates the maximum virtual stiffness satisfying the passivity condition. This can illustrate the conservativeness of the proposed passivity condition compared to the stability conditions developed above.

We can consider the tangent line of the stability boundary for low virtual stiffness (and damping) values in (4.12). One can take the limit as

$$\lim_{\beta \to 0} \frac{\varepsilon\beta(1+\beta)}{(\varepsilon + \varepsilon\beta - 1)} = \frac{1}{2} \tag{4.16}$$

In this case, the slop of the tangent can be approximated with a constant value of $1/2$, which results in the simple, linearized stability condition as

$$d + \beta > \frac{p}{2} \quad \Leftrightarrow \quad k_d + b > \frac{k_p \Delta t}{2} \tag{4.17}$$

Condition (4.17) was also reported earlier in (Gil et al., 2004). However, this condition is only valid for a limited range of virtual stiffness and damping, and does not provide any information on the characteristic points of the stability boundary for

higher virtual wall stiffness and damping. Compare to the stability conditions presented in equations (4.9) to (4.14), the linearized condition in (4.17) is a conservative stability condition. This condition has been the focus of the analysis in (Gil et al., 2004; Minsky et al., 1990) because considering the physical parameters of available haptic devices and the usual 1 ms sampling time, actuator saturation would occur before one would need to consider the actual, non-linear stability boundary.

The general results provided here can give important insight for the design of new devices, and have theoretical importance in comparing the stability of the mass-damper model to other models. Later it will be shown that when filtering and/or flexibility need to be considered linearized conditions only hold for a limited range of virtual wall parameters, and the effective mass and stiffness play an important role in system stability.

4.1.1 Effect of Computational Delays. Time-delay is generally an important phenomena that significantly affects haptic systems. For example, filters can usually introduce considerable delay effects. To investigate the effects of time-delay we consider again the rigid body model which is interacting with a single virtual wall without sustained human touch. In the following analysis we neglect the physical damping and focus on the destabilizing effect of computational delays.

To consider the time delay, a new state variable can be introduced which corresponds to the state of the system at the delayed time instant. However, this increases the size of calculation. Another way to account for the time delay is to consider a unit delay z^{-1}, which ensures uniformly timed actuation. When the time delay is longer (e.g. due to communication channel) it is usually just approximated as an integer multiple of the sampling time, i.e., $t_{delay} = l\Delta t,\ \ l = 0, 1, \ldots$, where l is the delay parameter. Employing representation (2.36) for the virtual interaction force, the dynamic equation of the rigid-body model described in (2.42) with the above

assumptions can be written as

$$\begin{gathered} m_e\ddot{x} = \lambda, \ , \quad t \in [t_j, t_{j+1}) \\ \text{with} \quad \lambda = (-k_p - \frac{k_d}{\Delta t})\, x_{j-l} + \frac{k_d}{\Delta t}\, x_{j-l-1} \end{gathered} \tag{4.18}$$

Stability conditions of this model can be developed by constructing the discrete mapping in closed-form following the process described in Sec. 3.2.3. For this purpose, dynamic equation (4.18) can be written with dimensionless coefficients as

$$x''(T) = (-p-d)x_{j-l} + d\, x_{j-l-1}\ , \quad T \in [j, j+1)\,. \tag{4.19}$$

The coefficient matrices in state-space representation of (4.19) take the form

$$\mathbf{C} = \begin{bmatrix} 0 & 1 \\ 0 & 0 \end{bmatrix}, \quad \mathbf{D} = \begin{bmatrix} 0 & 0 \\ (-p-d) & d \end{bmatrix} \tag{4.20}$$

In order to keep track the delayed positions during the piecewise solution of (4.19), one has to introduce an extended discrete state vector as $\mathbf{z} = [x'_j,\, x_j,\, x_{j-1}\,, \ldots\,, x_{j-l-1}]^{\mathrm{T}}$. With this, the transition matrix $\mathbf{L}$ can be obtained in the form

$$\mathbf{L} = \left[\begin{array}{cc|ccccccc} 1 & 0 & 0 & 0 & \ldots & 0 & 0 & -p-d & d \\ 1 & 1 & 0 & 0 & \ldots & 0 & 0 & -\dfrac{p+d}{2} & \dfrac{d}{2} \\ \hline 0 & 1 & 0 & 0 & \ldots & 0 & 0 & 0 & 0 \\ 0 & 0 & 1 & 0 & \ldots & 0 & 0 & 0 & 0 \\ 0 & 0 & 0 & 1 & \ldots & 0 & 0 & 0 & 0 \\ \vdots & \vdots & \vdots & & \ddots & & \vdots & \vdots & \vdots \\ 0 & 0 & 0 & 0 & \ldots & 1 & 0 & 0 & 0 \\ 0 & 0 & 0 & 0 & \ldots & 0 & 1 & 0 & 0 \\ 0 & 0 & 0 & 0 & \ldots & 0 & 0 & 1 & 0 \end{array}\right] \tag{4.21}$$

To ensure stability, as explained in Chapter 2, the eigenvalues of this matrix must lie inside the unit disk of the complex plane. To obtain stability conditions in closed-form, it is advantageous to first construct the characteristic polynomial

of the transition matrix $\mathbf{L}$. For this purpose, with the indicated partitioning, the characteristic polynomial can be expressed as

$$\begin{aligned}\det(\mathbf{L}-\mathbf{I}\lambda) &= \det\left(\begin{bmatrix}\mathbf{L}_1 & \mathbf{L}_2\\ \mathbf{L}_3 & \mathbf{L}_4\end{bmatrix} - \lambda\mathbf{I}\right) = \\ &\det(\mathbf{L}_4-\lambda\mathbf{I}) \times \det\left((\mathbf{L}_1-\lambda\mathbf{I}) - \mathbf{L}_2(\mathbf{L}_4-\lambda\mathbf{I})^{-1}\mathbf{L}_3\right)\end{aligned} \tag{4.22}$$

where $\mathbf{I}$ denotes different, appropriately sized identity matrices. By considering the special structure of $\mathbf{L}$, it can be shown that

$$\det(\mathbf{L}_4-\lambda\mathbf{I}) = (-\lambda)^{l+1} \tag{4.23}$$

$$(\mathbf{L}_4-\lambda\mathbf{I})^{-1}\mathbf{L}_3 = \begin{bmatrix} 0 & 1/\lambda \\ 0 & 1/\lambda^2 \\ \vdots & \vdots \\ 0 & 1/\lambda^{l+1} \end{bmatrix} \tag{4.24}$$

$$(\mathbf{L}_1-\lambda\mathbf{I})(-\mathbf{L}_2(\mathbf{L}_4-\lambda\mathbf{I})^{-1}\mathbf{L}_3) = \begin{bmatrix} 1-\lambda & \dfrac{d}{\lambda^{l+1}} - \dfrac{p+d}{\lambda^l} \\ 1 & \dfrac{d}{2\lambda^{l+1}} - \dfrac{p+d}{2\lambda^l} \end{bmatrix} \tag{4.25}$$

Then substituting these results into (4.22), the generic characteristic polynomial reads

$$p_l(z) = z^{l+3} - 2z^{l+2} + z^{l+1} + \frac{p+d}{2}z^2 + \frac{p}{2}z - \frac{d}{2} \tag{4.26}$$

For analyzing the effect of delay, two cases will be considered below. First the case without delay ($l=0$) is briefly summarized, then the stability of the model with one sampling time delay ($l=1$) is discussed.

For the case when there is no delay in the system, the polynomial in (4.26) is considered for $l = 0$. By applying the Moebius transformation, the transformed characteristic polynomial can be obtained as

$$p_{l=0}(\sigma) = p\sigma^3 + 2d\sigma^2 + (4-p-2d)\sigma + 4 \tag{4.27}$$

Then the Routh-Hurwitz criterion (Appendix A) can directly be applied to this polynomial to analyze its stability, which results in satisfying conditions as

$$\begin{aligned} &p > 0,\ d > 0, \text{ and } p < 4 - 2d \\ &D_2 = \begin{vmatrix} 2d & 4 \\ p & 4-p-2d \end{vmatrix} = -2(d+2)p + 4d(2-d) > 0 \end{aligned} \tag{4.28}$$

which implies the condition

$$p < \frac{2d}{d+2}(2-d) \tag{4.29}$$

This is the same condition as in (4.14) which was derived for the analysis of rigid-body model when β tends to zero. This boundary is shown in Fig.4.2.

When the processing delay is one sampling period the transformed characteristic polynomial is

$$p_{l=1}(\sigma) = p\,\sigma^4 + (2d-p)\sigma^3 - (4d+p-4)\sigma^2 + (2d+p+8)\sigma + 4 \tag{4.30}$$

The application of the Routh-Hurwitz stability criterion shows that the virtual stiffness has to be positive and the stability is limited by the positiveness of the third Hurwitz determinant as

$$\begin{aligned} \Delta_3 = &\begin{vmatrix} 2d-p & 2d+p+8 & 0 \\ p & -4d-p+4 & 4 \\ 0 & 2d-p & 2d+p+8 \end{vmatrix} = \\ &-16p^2 - 8(d^2+12)p - 16(d^3+4d^2-4d) \end{aligned} \tag{4.31}$$

Thus the stability boundary for physically meaningful (positive) virtual stiffness values reads

$$p < \frac{1}{4}\left(-12 - d^2 + (2+d)\sqrt{36 - 20d + d^2}\right)\ . \tag{4.32}$$

The resulting dimensionless stability boundary corresponding to this model is shown in Fig.4.2 and compared to that of obtained for the case without time delay. The analysis of this boundary gives the maximum virtual wall impedances as $p_{max} \approx 0.686$,

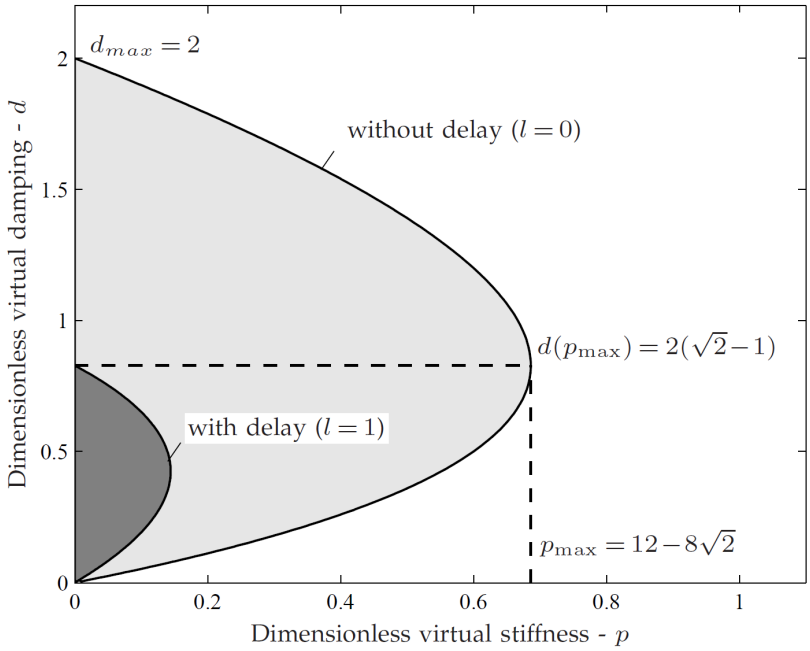

FIGURE 4.2. Dimensionless stability charts

$d(p_{max}) \approx 0.828$, and $d_{max} = 2$. The maximum renderable stiffness is considerably smaller than that of without delay.

4.2 Model with Structural Flexibility

As was discussed before the rigid-body model cannot be representative in the entire parameter region. In many cases, the structural flexibility of the device needs to be considered.

Let us consider the two-DoF model in (2.43) which was developed in Chapter 2, and validated experimentally in Chapter 3. As was discussed in Chapter 2, this model can be approximated with a single-DoF flexible model considering the dominant characteristic frequency of the system. This model is used in this section for derivation of closed-form parametric stability conditions. The usability of such conditions will be discussed later in this chapter.

We note that such a flexible model can also represent the human impedance. Using a single-DoF model, a detailed semi-analytical study on the effect of the importance of the human operator is presented in (Hulin et al., 2008). In that work, it is concluded that the stiffness of the human operator is generally in a range that does not influence much the stable domain. Here, the stiffness is associated with structural flexibility and the interpretation of the model is different. We focus on the effect of flexible components with relatively high stiffness, and provide new analytical results that are valid for both cases, when flexibility originates from structural elements or the human operator.

Let us consider the model in (2.44). Employing the representation in (2.36) for virtual interaction forces and using the backward differentiation formula for velocity approximation the dynamic equation of this model becomes

$$\begin{aligned} & m_{e2}\ddot{x}_2(t) + k_e x(t) = \lambda, \ , \quad t \in [t_j, t_{j+1}) \\ & \text{with} \quad \lambda = (-k_p - \frac{k_d}{\Delta t})\, x_{j-l} + \frac{k_d}{\Delta t}\, x_{j-l-1} \end{aligned} \tag{4.33}$$

where parameters m_{e2}, k_e are effective mass and stiffness, which were interpreted in more detail in Chapter 2. For development of closed-form stability conditions, constructing the discrete mapping in closed-form is required. For this purpose the process described in Section 4.1 is followed here for this model. Scaling the time by the sampling frequency, equation (4.33) can be rewritten with dimensionless coefficients as

$$x''(T) + \Omega_n x'(T) = (-p - d)x_j + d\, x_{j-1} \tag{4.34}$$

where $\Omega_{\mathrm{n}} = \sqrt{\frac{k_e}{me2}}\Delta t$ is the dimensionless natural frequency of the system.

The coefficient matrices in state-space representation of (4.34) can be obtained as

$$\mathbf{C} = \begin{bmatrix} 0 & 1 \\ -\Omega_{\mathrm{n}}^2 & 0 \end{bmatrix}, \ \mathbf{D} = \begin{bmatrix} 0 & 0 \\ -p-d & d \end{bmatrix} \tag{4.35}$$

In this case, the discrete state of the system can be characterized by the higher dimensional state vector $\mathbf{z}_j = [x'_j,\, x_j,\, x_{j-1}]^{\mathrm{T}}$. With this, the mapping $\mathbf{z}_{j+1} = \mathbf{L}\mathbf{z}_j$ has

the form

$$\mathbf{L} = \begin{bmatrix} \cos\Omega_\mathrm{n} & -\dfrac{(d+p+\Omega_\mathrm{n}^2)\sin\Omega_\mathrm{n}}{\Omega_\mathrm{n}} & \dfrac{d\sin\Omega_\mathrm{n}}{\Omega_\mathrm{n}} \\ \dfrac{\sin\Omega_\mathrm{n}}{\Omega_\mathrm{n}} & \cos\Omega_\mathrm{n} - \dfrac{(d+p)\,(1-\cos\Omega_\mathrm{n})}{\Omega_\mathrm{n}^2} & \dfrac{d(1-\cos\Omega_\mathrm{n})}{\Omega_\mathrm{n}^2} \\ 0 & 1 & 0 \end{bmatrix}. \tag{4.36}$$

The same transition matrix can be obtained using the two-Dof flexible model in (3.2), if $r_m = r_k \to 0$ and $m_{e1} \to \infty$.

The characteristic polynomial of (4.36) can be given by

$$p_z = -z^3 - \frac{d+p-(d+p+2\Omega_\mathrm{n}^2)\cos\Omega_\mathrm{n}}{\Omega_\mathrm{n}^2} z^2 - \frac{p+\Omega_\mathrm{n}^2 - p\cos\Omega_\mathrm{n}]}{\Omega_\mathrm{n}^2} z + \frac{d\,(1-\cos\Omega_\mathrm{n})}{\Omega_\mathrm{n}^2}, \tag{4.37}$$

and using the transformation $z = (\sigma+1)/(\sigma-1)$, it can be rewritten as

$$p_\sigma = \mu_3\sigma^3 + \mu_2\sigma^2 + \mu_1\sigma + \mu_0 \tag{4.38}$$

where

$$\begin{aligned} \mu_3 &= \frac{2\,(p+\Omega_\mathrm{n}^2)\,(1-\cos\Omega_\mathrm{n})}{\Omega_\mathrm{n}^2}, \\ \mu_2 &= \frac{2\,(2d+\Omega_\mathrm{n}^2)\,(1-\cos\Omega_\mathrm{n})}{\Omega_\mathrm{n}^2}, \\ \mu_1 &= \frac{2\,(-2d-p+\Omega_\mathrm{n}^2+(2d+p+\Omega_\mathrm{n}^2)\cos\Omega_\mathrm{n})}{\Omega_\mathrm{n}^2}, \\ \mu_0 &= 2(1+\cos\Omega_\mathrm{n})\,. \end{aligned} \tag{4.39}$$

To ensure stability, based on the Routh-Hurwitz criterion, conditions $\mu_i > 0,\ i = 0,1,2,3$ and $\Delta_2 = \mu_1\mu_2 - \mu_3\mu_0 > 0$ has to be simultaneously satisfied. From $\mu_3 > 0$ it follows that $p > -\Omega_\mathrm{n}^2$ for any value of d, which boundary is a vertical line in Fig. 4.3. Similarly, $\mu_2 > 0$ implies that $d > -\Omega_\mathrm{n}^2/2$, and $\mu_1 > 0$ results in

$$d < -1/2\,\left(p - \Omega_\mathrm{n}^2/\tan\left(\Omega_\mathrm{n}/2\right)^2\right) \tag{4.40}$$

And finally condition $\Delta_2 > 0$ can be written as

$$\Delta_2 = \frac{16 \sin\left(\frac{\Omega_\mathrm{n}}{2}\right)^2}{\Omega_\mathrm{n}^4} \left(-2d^2 - d\,p - \Omega_\mathrm{n}^2\,p + d\left(2d + p + 2\Omega_\mathrm{n}^2\right)\cos\Omega_\mathrm{n}\right) > 0 \qquad (4.41)$$

Based on (4.8) and the definition described for the equation of a hyperbola, it can

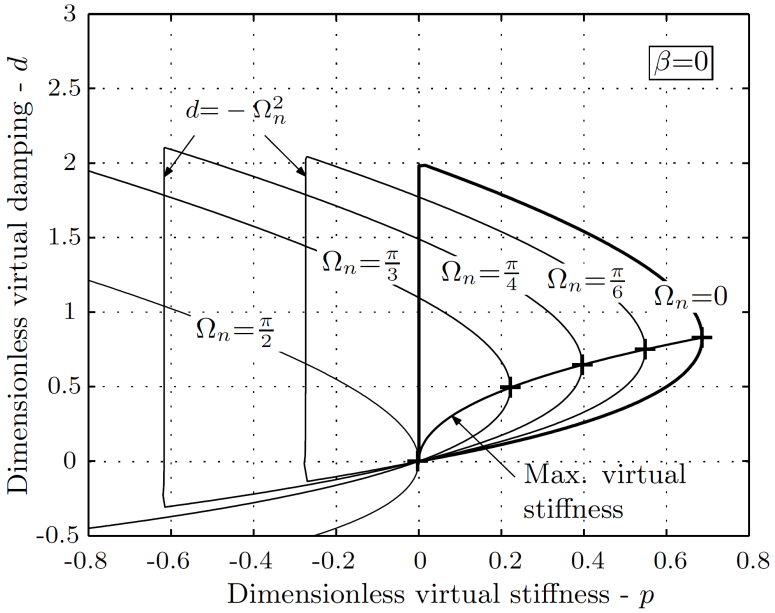

FIGURE 4.3. Stability charts: mass-spring model without damping

be seen that the equation in (4.41) is a hyperbola. The solution of $\Delta_2 = 0$ for $p > 0$ gives a limit as

$$p < \frac{-2d^2(1 - \cos\Omega_\mathrm{n}) + 2d\Omega_\mathrm{n}^2 \cos\Omega_\mathrm{n}}{d(1 - \cos\Omega_\mathrm{n}) + \Omega_\mathrm{n}^2}\,. \qquad (4.42)$$

The corresponding boundaries described above intersect the line $p = -\Omega_\mathrm{n}^2$ at the same point as the hyperbola in (4.41), and result in the stability boundary as

$$-\Omega_\mathrm{n}^2 < p < \frac{-2d^2(1 - \cos\Omega_\mathrm{n}) + 2d\Omega_\mathrm{n}^2 \cos\Omega_\mathrm{n}}{d(1 - \cos\Omega_\mathrm{n}) + \Omega_\mathrm{n}^2}\,. \qquad (4.43)$$

By searching for the maximum dimensionless virtual stiffness value that satisfies this condition one can obtain

$$p_{max} = \frac{4\Omega_{\mathrm{n}}^2 \left(1 - \sqrt{2}\cos\left(\frac{\Omega_{\mathrm{n}}}{2}\right)\right) + 2\Omega_{\mathrm{n}}^2 \cos\left(\Omega_{\mathrm{n}}\right)}{1 - \cos\left(\Omega_{\mathrm{n}}\right)} \tag{4.44}$$

$$d(p_{max}) = \frac{-\Omega_{\mathrm{n}}^2 \left(1 - \sqrt{2}\cos\left(\frac{\Omega_{\mathrm{n}}}{2}\right)\right)}{1 - \cos\left(\Omega_{\mathrm{n}}\right)} \tag{4.45}$$

In addition, the maximum dimensionless virtual damping can be obtained by substitution of $p = -\Omega_{\mathrm{n}}^2$ into (4.40) which results in

$$d_{max} = \Omega_{\mathrm{n}}^2 / (1 - \cos\Omega_{\mathrm{n}}) \tag{4.46}$$

The closed-form stability conditions in equations (4.43) to (4.46) make it possible to investigate the effects of structural flexibility on the performance of haptic devices. For values of the dimensionless frequency parameter $\Omega_{\mathrm{n}} \in [0,\ \pi/2]$, the stable domains are presented in Fig. 4.3. In this figure, the points with maximum stiffness are also shown by crosses for different values of Ω_n. The connecting continuous line is plotted by using (4.44) and (4.45). It can be seen that for increasing values of Ω_{n} the maximum renderable stiffness is gradually decreasing, while at $\Omega_{\mathrm{n}} = \pi/2$ (half of the Nyquist frequency) the stable domain of physically meaningful virtual wall parameters disappears. This shows that at frequencies higher than half of Nyquist frequency, stable rendering of virtual environments is not possible. It can be seen from this that the selection of physical stiffness such that the undamped natural frequency matched the Nyquist frequency in (Colgate and Schenkel, 1997) is very conservative and far from practical applications.

This analysis illustrates that the structural flexibility can seriously limit the stability of haptic systems. However, for the case when the flexibility corresponds to the human representation, in the range of human impedance parameters, the Ω_n is very small and the stability boundary is close to the case $\Omega_n = 0$.

By limiting the further investigation to the physically meaningful positive domain of virtual stiffness and damping and substituting the cosine function by its second

order truncated Taylor series, the condition in (4.43) simplifies to

$$0 < p < \frac{2d}{d+2}(2 - d - \Omega_{\mathrm{n}}^2) \tag{4.47}$$

Note that (4.47) with $\Omega_{\mathrm{n}} = 0$ reduces to the stability condition for the rigid-body model presented in (4.14). Based on (4.47) the stability condition for small virtual damping values,i.e., $d \ll 2$ can be given as

$$d > \frac{p}{2 - \Omega_{\mathrm{n}}^2} \quad \Leftrightarrow \quad k_d > \frac{k_p \Delta t}{2 - \Omega_{\mathrm{n}}^2} \tag{4.48}$$

This linear stability condition is an important extension of (4.17) for the case when structural flexibility needs to be considered. Note that in the derivation of this linear condition, the effect of physical dissipation is neglected. Although its use is limited to low virtual impedances, it shows that higher virtual damping is required to achieve stability compared to the rigid-body case with perfect joints. It can be concluded that the achievable maximum stiffness, and therefore the performance of haptic devices with structural flexibility depends on the dimensionless frequency Ω_{n}, which is analytic function of system inertia, stiffness properties and the sampling time.

4.3 Practical Usability of Different Models

As we have seen, two simplified models allow for the derivation of closed-form results and formulas that are analytic functions of the parameters of the system. Such formulas can generally be helpful in several different aspects of haptic system analysis and design. However, the practical usability, validity, and role of the supporting simplified models need further consideration. Besides the representativeness of the simplified models, another more fundamental question is whether a rigid body model or a model with structural flexibility is the right representation for a haptic system. Overall, we will consider that a haptic system representation that incorporates the structural properties of the mechanical elements gives a more accurate description. However, the rigid-body model results in a simpler representation, has its own validity, and can also be applicable in some situations. We also note here that most haptic

analysis studies use a simple point-mass model, which, as was shown earlier, can be derived with the assumption of a rigid body model.

The full, flexible model can be represented with (2.16) and (2.17) for haptic equilibrium. As discussed, the modified model based on the two generalized inertia representation (2.35) can represent the dynamics and may be used to replace the full flexible model. If we have pure force or moment rendering only then this leads to the two-dof model of (2.43).

For further illustration here, where needed, we will also use the parameters of the experimental system used in Chapter 3. The various models lead to the stability charts shown in Fig. 4.4. This figure includes results from four models: the 2DoF flexible model with physical damping, the 1DoF flexible model (2.44) with physical damping, the 1DoF flexible model without damping, and the 1DoF rigid-body model without damping. For the latter two models the closed-form analytical results were obtained in this chapter. For the first two models with physical damping the analysis was carried out numerically in Chapter 3. The applicability of different models primarily depends on the dominant vibration frequency of the device-virtual environment system. When this frequency is far below the first natural frequency of the device then the rigid body model approximates well the physical system. For higher virtual impedances, however, the dominant frequency may be close to the first natural frequency of the haptic device. In these cases structural flexibility has to be considered. This is illustrated in Figs. 4.4 for a representative set of parameters. This can also be illustrated via Fig. 3.8 in Chapter 3, which shows how the ratio between the dominant vibration frequency and the natural frequency changes. This separates the stability boundary into two parts. The part of the stability boundary with low dominant vibration frequencies is represented by the curve that can be obtained based on the rigid body model with no damping (see Fig. 3.8). As was discussed in Chapter 3, this part is very close to a straight line. For the other part of the stability boundary characterized by high dominant vibration frequencies, the curve obtained using the single-DoF flexible model with damping gives good representation. The

overall behaviour for the entire stability domain is well-captured by the 2DoF flexible model with damping that was obtained considering the model reduction described in Chapter 2.

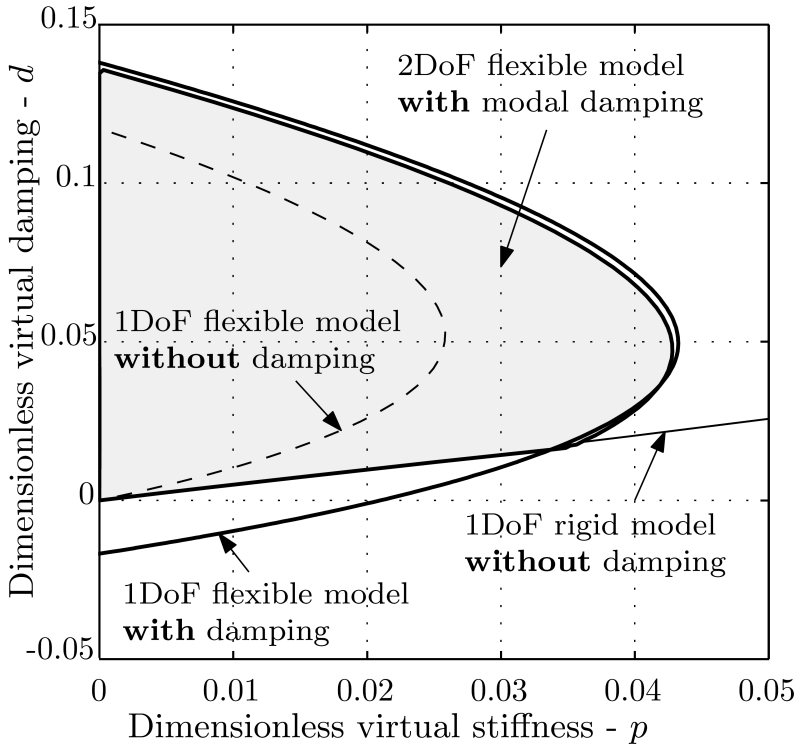

FIGURE 4.4. Stability charts: mass-spring model without damping

As can be seen in Fig. 4.4, the single-DoF flexible model with no damping, which was analyzed to obtain closed-form formulas, gives more conservative results for the stable area. However, this can give a useful representation for designing haptic systems as conservativeness may also be desirable. Generally, it can be required to have settings and parameters that ensure functioning inside this area. The way how parameter changes influence this domain can give important information for design and operation. On the other hand, for lower values of virtual damping the rigid-body model can also be used.

CHAPTER 5

Performance Measures in Haptics and Effects of Design Parameters

Design and performance evaluation of haptic devices are more challenging compared to other robotic manipulators. In this chapter, closed-loop performance measures are developed in terms of mechanical design parameters of the system for haptic application. These indices measure the renderable virtual environment impedance range and the fidelity of the force feedback. These parametric performance measures are compared with those of traditionally used in design of robotic mechanisms and their properties are discussed for applications in haptics.

5.1 Common Performance Measures in Robotic Mechanisms

Mechanical design of a haptic interface is a challenging problem in general. This is because it is important for a haptic device to be light-weight, and stiff at the same time, while being stable in interaction with stiff virtual environments. Initial design of a haptic device includes the basic requirements which are typically considered in design of robotic systems. However, optimization of mechanism parameters can be done based on requirements of haptic application, such as workspace size, static and dynamic load requirements. There are several studies in the literature dedicated to the optimization of mechanism parameters of haptic devices (Hayward et al., 1994;

Vlachos et al., 2004; A. Frisoli and Salsedo, 2007; S. Li and Bergamasco, 2010; Khan et al., 2011; Gil et al., 2012). This was discussed in more detail in Chapter 1. Most of the performance indices in these studies are related to kinematic and dynamic dexterity considering the Jacobian and inertia matrices of the mechanism, which depend on the mechanical design parameters of the system.

A frequently used performance index in robotic mechanisms is the manipulability. Manipulability is proposed in (Yoshikawa, 1985) as a measure of easiness of changing arbitrarily the position and orientation of the end-effector, and it can be defined as

$$w = \sqrt{det(\mathbf{J}\mathbf{J}^{\mathrm{T}})} \tag{5.1}$$

where $\mathbf{J}$ is the Jacobian matrix of the mechanism, and w is proportional to the volume of the manipulability ellipsoid. It is shown in (Yoshikawa, 1985) that the volume of the force ellipsoid is inversely proportional to w. It can be shown that the manipulability and force ellipsoids have the same principal axes and their radii in each principal axis are inversely proportional. This implies that the direction in which a large force can be generated at the end-point via joint torques is the one along which manipulability is low. In haptic applications, this corresponds to the case of rendering virtual environments with high stiffness.

Another frequently used performance measure is the kinematic isotropy. It is argued that the concept of kinematic isotropy over a given workspace is a good measure of design quality for many applications where high accuracy at low velocity is required (Stocco et al., 1997), this is the case in haptic applications.

When the condition number of the Jacobian matrix reaches the minimum value of unity, the manipulator is called isotropic (Salisbury and Craig, 1982), and it can be defined as

$$\kappa(\mathbf{J}) = \|\mathbf{J}\|\|\mathbf{J}^{-1}\| \tag{5.2}$$

where using the 2-norm results in the ratio between the largest and the smallest singular values of the Jacobian matrix. However, the Frobenius norm has the advantage of

resulting in an analytic function. The kinematic isotropy of serial and parallel manipulators are studied in (Angeles and Lopez-Cajun, 1992) and (Zanganeh and Angeles, 1997), respectively. The index for kinematic isotropy has been considered in haptic device design for position accuracy, and minimization of joint torque distortions when transferred from actuators to the human operator at the end point (A. Frisoli and Salsedo, 2007; S. Li and Bergamasco, 2010; Khan et al., 2011).

For higher precision manipulation like in haptic applications it is also necessary to consider the dynamics of the device in the design. Several measures of the dynamic performance of robotic systems have been introduced in the literature. Dynamic manipulability was introduced originally in (Yoshikawa, 1985) to measure the capability of the device in changing acceleration in different directions in the workspace via joint actuators. By considering the realizable end point accelerations, the dynamic manipulability can be defined as

$$w_d = \sqrt{det(\mathbf{J}(\mathbf{M}^{\mathrm{T}}\mathbf{M})^{-1}\mathbf{J}^{\mathrm{T}})} \tag{5.3}$$

where $\mathbf{M}$ is the inertia matrix of the device represented in the joint-space. In haptic applications, the dynamic manipulability measure can be related to the capability of the haptic device of rendering virtual environments through joint actuators.

The concept of dynamic isotropy (Ma and Angeles, 1993) may also be applied. A mechanism is said to be dynamically isotropic in a configuration at which the generalized inertia matrix of the device is isotropic. This can be quantified by measuring the condition number of the inertia matrix represented in a coordinate system which can be defined based on the analysis. Isotropy of the inertia matrix of the device has advantages such as possible decoupling of the dynamics of the system. This can result in decoupled inertia torques, and weak joint coupling, which may be advantageous in terms of control and dynamic analysis of the system.

The performance indices discussed so far are local measures of kinematic and dynamic performance. Therefore, they are configuration dependent. Global measures are presented in the literature to describe the behaviour throughout the workspace.

An example of this is shown in (Gosselin and Angeles, 1991) by integrating the local performance measure over the workspace. Another approach is presented in (Stocco et al., 1997) which defines a global isotropy index. In such approaches, normalization of the design matrix is necessary to make the different entries homogeneous in physical units.

5.2 Closed-Loop Performance Measures in Haptics

In haptic applications, considering the closed-loop performance of the system is of great importance. There is no agreement on which performance measure is most appropriate to be considered for haptic applications (Hayward and Astley, 1996). As discussed in Chapter 1, most of the closed-loop haptic performance indices are measurement based rather than being model based. However, the relation between mechanical parameters and haptic performance is important for design of new haptic devices or optimizing the existing interfaces.

The results of the dynamic modelling and parametric analysis conducted in the previous chapters are employed here to develop closed-loop performance measures reflecting the effects of mechanical design parameters. Quantitative measures of the stable virtual impedance range and fidelity of the virtual interaction force are developed for both rigid-body and flexible models.

5.2.1 A Measure for the Range of Stable Virtual Impedances. The closed-loop performance of haptic interfaces, which includes the effect of digital control realization, can be quantified via stability conditions. We place emphasis on the characterization of the maximum achievable stiffness in the view of stability of the digitally controlled system. As discussed before, the interaction with a virtual wall can be considered as a typical example for haptic system analysis. It was shown in Chapter 2 that different models can be representative depending on the operating conditions.

When the rigid-body model in (2.42) is employed, by eliminating the effect of physical damping and without the human operator's sustained touch, i.e., $f_d = 0$

and $f_h = 0$, equation (4.14) gives a representative yet slightly conservative stability condition. It was also shown in Chapter 3 that the physical damping and the human operator can contribute to the stabilization of the system. However, the focus here is to investigate the effects of mechanical design parameters of the device on the performance. Conservativeness on the other hand may be desirable in the design of haptic devices.

The condition in (4.14) results in a boundary in the space of dimensionless virtual environment parameters p and d, where $p_{max} = 0.686$ and $d_{max} = 2$. Considering these, the maximum stable virtual stiffness and damping in terms of physical parameters can be obtained as

$$k_{p,max} = 0.686\frac{m_{e1}}{\Delta t^2}, \quad \text{and} \quad k_{dmax} = 2\frac{m_{e1}}{\Delta t} \tag{5.4}$$

where m_{e1} is the effective mass of the device interpreted for the rendered directions as described in Chapter 2. This shows that for the case when the rigid-body model is representative, the maximum stable virtual environment parameters have relation with the effective mass, and the sampling time of the system. The effective mass, as can be seen in (2.28), is obtained via considering the inertia and Jacobian matrices of the system. Therefore, the maximum renderable virtual environment parameter can be changed based on the selected architecture of the mechanism, dimensions, and material used for the device.

The stable area of dimensionless virtual environment parameters can be obtained by integrating the area bounded by (4.14), with integration limit $d = 0$ to $d = 2$. This area can specify the range of all stable virtual environment parameters which can be rendered by a haptic device, when the rigid-body model is representative. This can be considered as a performance indicator containing information similar to that of the z-width (Colgate and Brown, 1994). The resulting index in terms of physical parameters of the system can be obtained as

$$w_s = 0.91\frac{m_{e1}^2}{\Delta t^3} \tag{5.5}$$

For low virtual damping, the linear condition in (4.17) can be used. In this case, the maximum achievable stiffness is limited by the physical and virtual damping, and the actuator saturation. The inertia of the system has little or no influence on the stability. Based on this, mechanical design parameters cannot influence the stability of the haptic system in this range of applications.

In the case when filters are employed in haptic rendering, as shown in Chapter 3, the delay introduced by filters can considerably decrease the stable domain of virtual environment parameters. The dynamics of the system in that case can be studied by modelling the filter as an additional dynamic subsystem. However, this is not the intention in this chapter, since the focus is on investigating effects of mechanical design parameters. As a simplified solution, one can consider the model in (4.19) for the case when rigid-body model with time delay is considered. For this case, one sampling time delay is considered, as a very specific example of time delay, and the stability condition was obtained in (4.32). This results in a stability boundary in p-d plane with $p_{max} = 0.144$ and $d_{max} = 0.828$. These can be extended in terms of physical parameters which results in

$$k_{p,max} = 0.144\frac{m_{e1}}{\Delta t^2}, \quad \text{and} \quad k_{d,max} = 0.828\frac{m_{e1}}{\Delta t} \tag{5.6}$$

This is similar to (5.4) with different coefficients, where the coefficients depend on the time-delay. Although the stable domain in this case is much smaller than the case with no delay, but still the maximum achievable virtual stiffness is governed by the effective mass of the system at the point of contact with the virtual environment and the sampling time.

When the structural flexibility of the device is taken into consideration, condition in (4.43) has to be considered for positive virtual stiffness values. This condition forms a hyperbola in the space of virtual environment parameters, while the maximum

virtual stiffness and damping can be obtained as

$$\begin{aligned} k_{p,max} &= k_e \left[\frac{4(1-\sqrt{2}\cos\frac{\Omega_n}{2}) + 2\cos\Omega_n}{1-\cos\Omega_n} \right] \\ k_{d,max} &= k_e \Delta t \left[\frac{\cos\Omega_n}{1-\cos\Omega_n} \right] \end{aligned} \tag{5.7}$$

The corresponding area of the stable domain can be obtained as

$$w_s = \frac{m_{e2}^2}{\Delta t^3} \frac{\Omega_n^4}{\sin(\frac{\Omega_n}{2})} \left[1 + 4\cos\Omega_n + \cos 2\Omega_n - 4(1+\cos\Omega_n)\ln(1-\cos\Omega_n)\right] \tag{5.8}$$

where m_{e2} is the smaller effective mass of the model as defined in Chapter 2. The conditions in (5.7) and (5.8) show that the closed-loop performance in cases where the flexible model is considered can be specified via the dimensionless natural frequency Ω_n. As described in Chapter 4, the Ω_n depends on the smaller effective mass of the system, m_{e2}, the effective stiffness, k_e, and the sampling time, Δt. In case of the experimental haptic device described in Chapter 3, the inertia and stiffness properties of the actuator mechanisms define the smaller effective mass and the effective stiffness. Therefore, the selection of the actuator systems can have significant effects. It is important to note that the Jacobian matrix of the device still appears in interpretation of the effective parameters. This means that the kinematic parameters of the device are still important in the design, where the Jacobian depends on the physical dimensions and the configuration of the system.

5.2.2 A Measure for Fidelity. In this section, we look at the system from a different perspective. Consider the common Kelvin-Voigt model based virtual wall as a simple virtual environment. In terms of the mathematical formulation, this is similar to a PD controller in motion control in robotics. However, there is a fundamental difference. In motion control, the gains can be tuned to obtain a required performance, while in haptics they carry physical meaning and refer to stiffness and damping of a virtual wall or environment. In such a case, for stable rendering of a specific virtual wall parameters, i.e., fixed values of P and D, tuning of the mechanical design properties can be of interest.

For the case when structural flexibility plays an important role in the behaviour of a haptic device, the fidelity of the perceived force at the end point can become a critical issue. This is because the vibration of the flexible parts can significantly influence the force sensation. For this case, we can consider the single-DoF flexible model represented in (2.44). The corresponding stability analysis is presented in Chapter 4. It is shown that, to ensure stability, all the roots of the characteristic polynomial of the transition matrix (4.36) must lie within the unit disk of the complex plane. It was discussed in Chapter 2 that in this case the system loses its stability when the magnitude of one of the complex conjugate pairs of eigenvalues exceeds unity. Therefore, the system loses stability with oscillatory behaviour. It is of interest to identify how fast these oscillations decay. The fastest decaying transient vibration can be obtained by the minimum spectral radius of the characteristic multiplier z in (2.40). For this purpose, we can consider transformation $z = \rho\tilde{z}$, where $\rho \in [0, 1]$ is the spectral radius. This transformation maps the unit disk to a unit circle in the complex plane, which leads to

$$|z| < \rho \longleftrightarrow |\tilde{z}| < 1 \tag{5.9}$$

and the characteristic polynomial in (4.37) can be rewritten as

$$p_3(z) = \sum_{i=0}^{3} \lambda_i (\rho\tilde{z})^i = \sum_{i=0}^{3} (\lambda_i \rho^i)\tilde{z}^i \tag{5.10}$$

As described in Chapter 2, applying the Moebius transformation of $\tilde{z} = \frac{\tilde{\sigma}+1}{\tilde{\sigma}-1}$ makes it possible to apply the Routh-Hurwitz stability criterion, using which one can make sure that the roots of the original characteristic polynomial are within a specific spectral radius. In this case, the transformed characteristic polynomial can be written as

$$p_3(\tilde{\sigma}) = (\tilde{\sigma}-1)^3 \sum_{i=0}^{3} (\rho^i \lambda_i)(\frac{\tilde{\sigma}+1}{\tilde{\sigma}-1})^i = \sum_{i=0}^{3} \tilde{\mu}_i \tilde{\sigma}^i \tag{5.11}$$

where the coefficients $\tilde{\mu}_i$ depend on the system parameters and the spectral radius. By factoring $1/\Omega_n$ for simplification purpose, these coefficients can be written as

$$\begin{aligned}
\tilde{\mu}_3 &= [\rho\Omega_n^2(1+\rho) + (1-\rho)(d(\rho-1)+p\rho) - (d(\rho^2-1)+\rho(p+\rho p+2\rho\Omega_n^2))\cos(\Omega_n)] \\
\tilde{\mu}_2 &= [3\rho^3\Omega_n^2 - 3d(\cos(\Omega_n)-1) - \rho(p+\Omega_n^2-\rho\cos(\Omega_n)) + \rho^2(d+p-(d+p=2\Omega_n^2)\cos(\Omega_n))] \\
\tilde{\mu}_1 &= [-d(3+\rho^2) - \rho(p+p\rho+\Omega_n^2+3\rho^2\Omega_n^2) + (d(3+\rho^2)+\rho(p+p\rho+2\rho\Omega_n))\cos(\Omega_n)] \\
\tilde{\mu}_0 &= [d+p\rho-\rho^2(d+p)+\rho\Omega_n^2(1+\rho^2) + ((\rho-1)(d+(d+p)\rho)+2\rho^2\Omega_n^2)\cos(\Omega_n)]
\end{aligned} \tag{5.12}$$

Based on the Routh-Hurwitz criterion, satisfying conditions $\tilde{\mu}_i > 0$, $i = 0, ..., 3$, and $\Delta_2 > 0$ result in a boundary in $p - d$ plane, which can be described in terms of physical parameters as

$$c_2x^2 + c_1x + c_0 = 0 \quad \text{with} \quad x = \cos\left(\sqrt{k/m_{e2}}\Delta t\right)$$

$$\begin{aligned}
c_0 &= k_dk_p\Delta t\rho^2 + k_d^2(1+\rho^2) + k\Delta t^2\rho^4(k+k_p-k\rho^2) \\
c_1 &= -2k_d^2 - 2k_d(k_d+(k+k_d)\Delta t)\rho^2 - k\,k_p\Delta t^2\rho^4 \\
c_2 &= k_d(k_d+(kd+(2k+k_p)\Delta t)\rho^2)
\end{aligned} \tag{5.13}$$

where, with a fixed virtual stiffness and damping value, the design parameters are m_{e2} and k_e. Then considering the case when the effective mass can be changed independently of the effective stiffness by design, m_{e2} can be expressed as

$$m_2 = \frac{k_e\Delta t^2}{\arccos\left(\dfrac{c1 \pm \sqrt{c_1^2-4c_0c_2}}{2c_2}\right)} \tag{5.14}$$

In order to obtain the fastest decaying vibration at the border of the sability domain, spectral radius ρ should be minimized. Using (5.14) results in the definition of the optimal spectral radius as

$$\rho_{opt} = \frac{2\sqrt{2}\sqrt{k_ek_d\Delta t + k_dk_p\Delta t}}{\sqrt{4k_d^2+8k_ek_d\Delta t+4k_dk_p\Delta t+k_p^2\Delta t^2}} \tag{5.15}$$

Substituting the optimum spectral radius (5.15) in (5.14) results in the determination of $m_{e2,opt}$ at which the high frequency components optimally decay. This index may be used as a measure for fidelity improvement of the force feedback. This can also has positive effect on the accuracy of the velocity estimation.

5.3 Example of the Five-Bar Linkage Based Haptic Device

The experimental haptic device described in Chapter 3 (Fig. 3.1) is considered for further analysis in this section. The parameters of the device are given in Table 3.2. This device was originally developed to satisfy global dexterity requirements in the workspace. The intention here is to investigate effects of mechanical design parameters on the performance indices described earlier.

The kinematic and dynamic manipulability, and the kinematic isotropy representations can be obtained for this device. For the case of rigid-body modelling, $\mathbf{M}$ and $\mathbf{J}$ are 2×2 joint-space inertia and Jacobian matrices of the device as described in Appendix B. These indices are determined for the entire workspace of the haptic device, and are presented in Fig. 5.1. It can be seen in this figure that the kinematic isotropy is almost constant and close to unity in most of the workspace, where the kinematic and dynamic manipulability are maximum. Dexterity of the device is low at locations close to the workspace boundary.

In addition to these indices, the proposed closed-loop performance in terms of impedance range for both rigid-body and the flexible models can be interpreted for this device. The maximum virtual stiffness, $k_{p,max}$, in (5.4) and (5.7); and the range of stable virtual parameters, w_s, in (5.5) and (5.8) can be used for the rigid-body and flexible models, respectively. The resultant measures over the workspace of the device are shown in Figs. 5.2 and 5.3 for rigid-body and flexible models, respectively. It can be seen in these figures that changes of indices show similar characteristics for both rigid-body and flexible models. However, these changes are in contrast with dexterity measures as shown in Fig. 5.1. We discussed earlier that for the directions along which the kinematic manipulability is higher, smaller end-point force can be

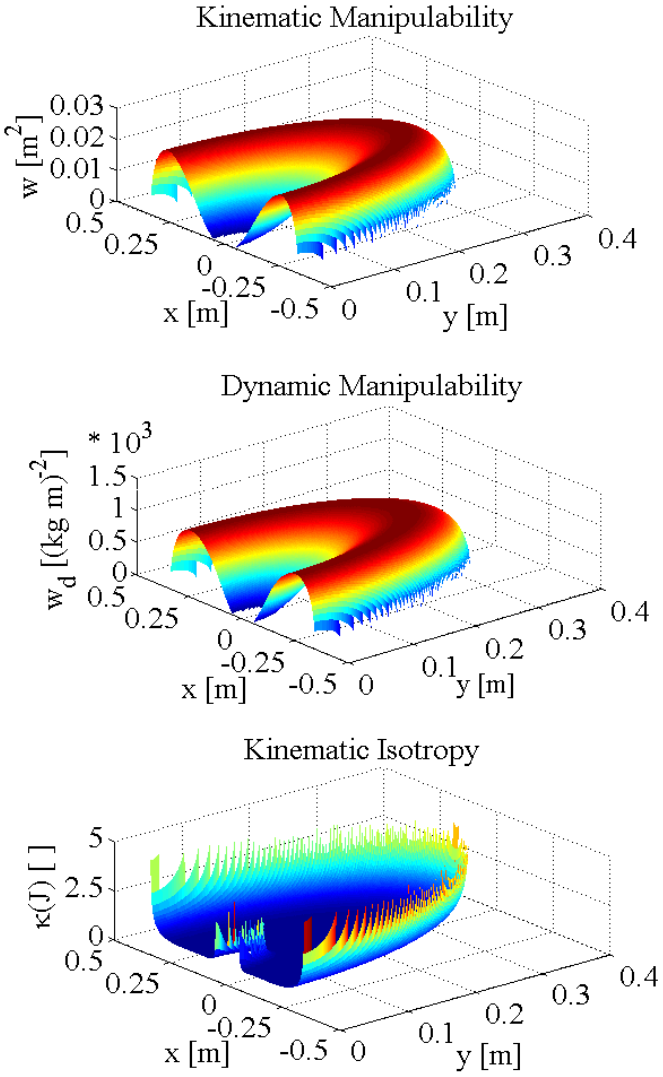

FIGURE 5.1. Kinematic manipulability, w, dynamic manipulability, w_d, and kinematic isotropy, $\kappa(\mathbf{J})$, over the workspace of the two-DoF experimental haptic device

achieved via a set of constant joint torques. It can be seen that best performance in terms of impedance range can be achieved at locations where the condition number and manipulability are low. However, in design of haptic devices, higher dexterity of the device is also of interest. In applications where rendering stiff virtual environment is required, achieving both dexterity and high stable virtual stiffness is in contrast; therefore, there should be a compromise between these performance requirements.

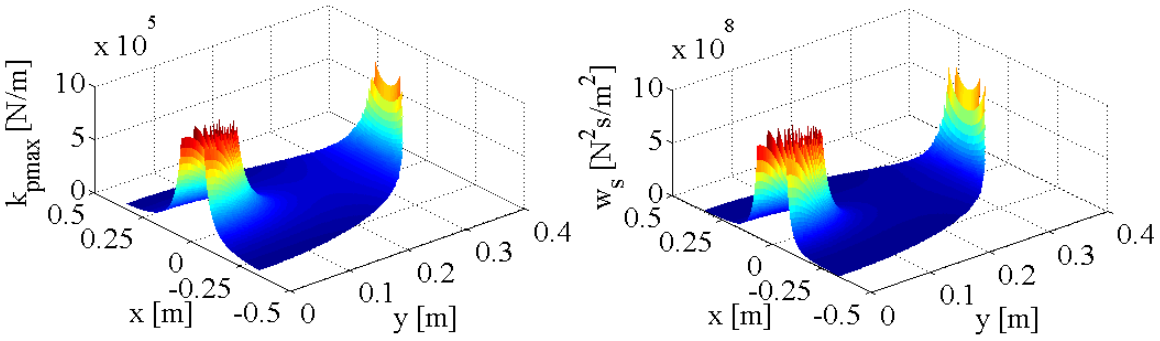

FIGURE 5.2. Maximum virtual stiffness, $k_{p,max}$, and stable area of virtual parameters, w_s, over the workspace of the rigid-body model of the haptic device

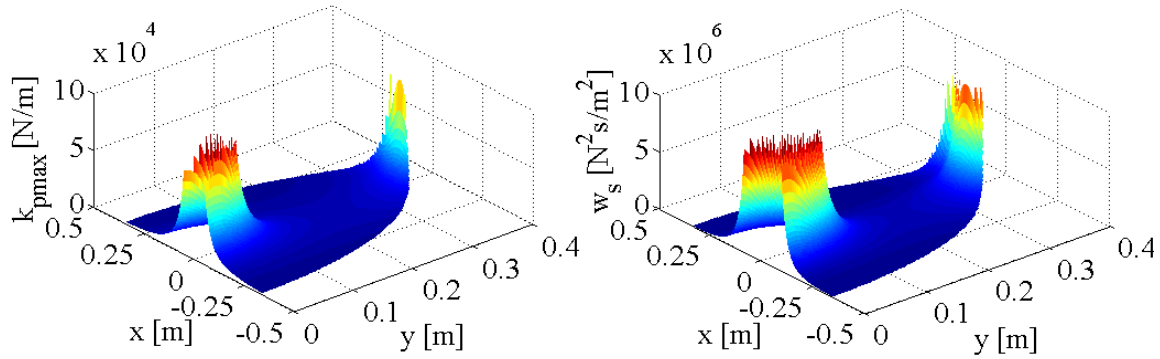

FIGURE 5.3. Maximum virtual stiffness, $k_{p,max}$, and stable area of virtual parameters, w_s, over the workspace of the flexible model of the haptic device

For better comparison of these measures, contour plots corresponding to the manipulability, condition number of the Jacobian matrix and maximum renderable virtual stiffness for the rigid-body model are shown in Fig. 5.4. In this figure, manipulability at $w = 0.015\ m^2$, kinematic condition number at $\kappa = 1.3$, and effective mass $m_{e1} = 0.2$ kg, which is an indicator of the maximum renderable stiffness in rigid-body model (5.4), are selected for the contour plots. These values were selected for the illustration purpose, and they correspond to the locations in the workspace close to the reference configuration of the device as described in Chapter 3. The area in the workspace satisfying the selected value of kinematic manipulability and condition number are shown via a light gray area with dash-dotted line, and dashed line,

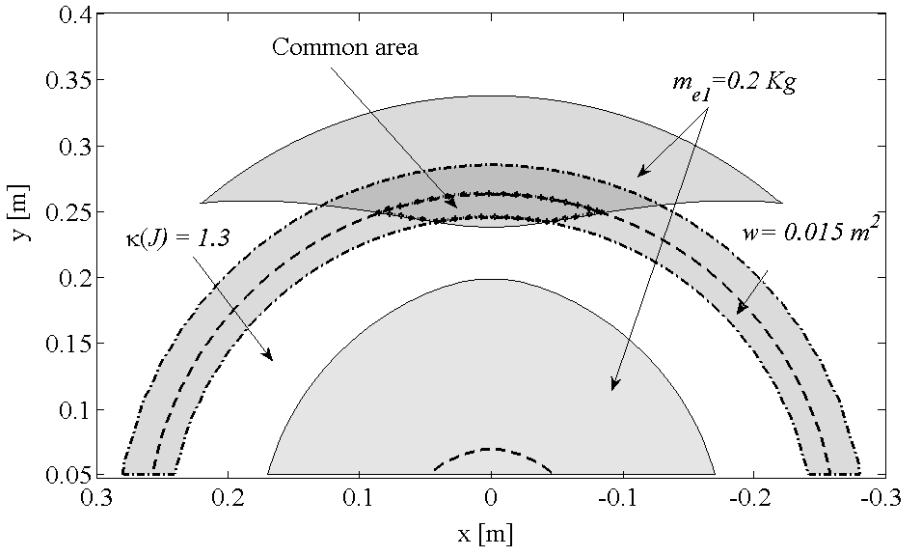

FIGURE 5.4. Contour plots of performance indices over the workspace

respectively. The area corresponding to the selected effective mass for the rigid-body model is indicated via the dark-gray area with solid line. The area in the workspace simultaneously satisfying the selected value of manipulability, condition number, and the effective mass is shown by bold dotted line and is indicated as "common area" in the figure. This area of the workspace corresponds to locations where high dexterity and rendering stiff environment can be achieved at the same time. However, if a stiff virtual wall is the main requirement, then maximizing the effective mass in the rendered direction can be the main objective. This can be achieved either by design optimization, or in case of a redundant/reconfigurable mechanism, by changing the configuration of the mechanism for a certain workspace position.

5.3.1 Effects of Mechanical Design Parameters on the Impendence Range. In the current design of the device, the distance between the axes of the two driven joints is zero and cannot be changed (Fig. 3.2). We can consider a modified design that is reconfigurable for different applications. This can be achieved by introducing one more kinematic pair to assess the capability of changing the distance between the driven joints, indicated by parameter d in Fig. 5.5(a). For various values of parameter d, the range of $k_{p,max}$ for the rigid-body and flexible models are

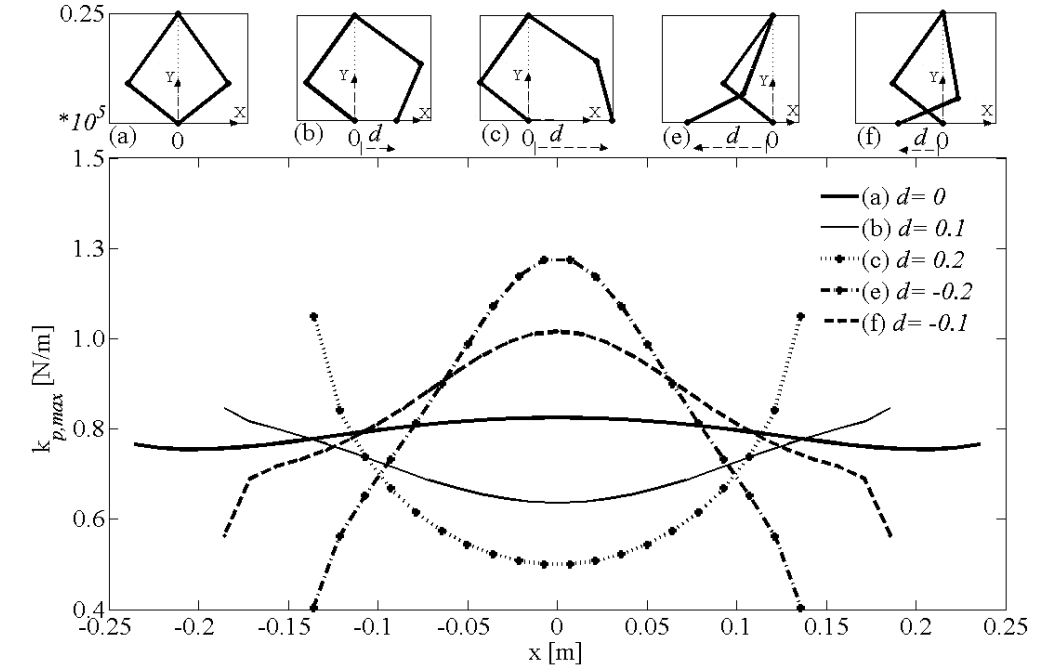

(a)

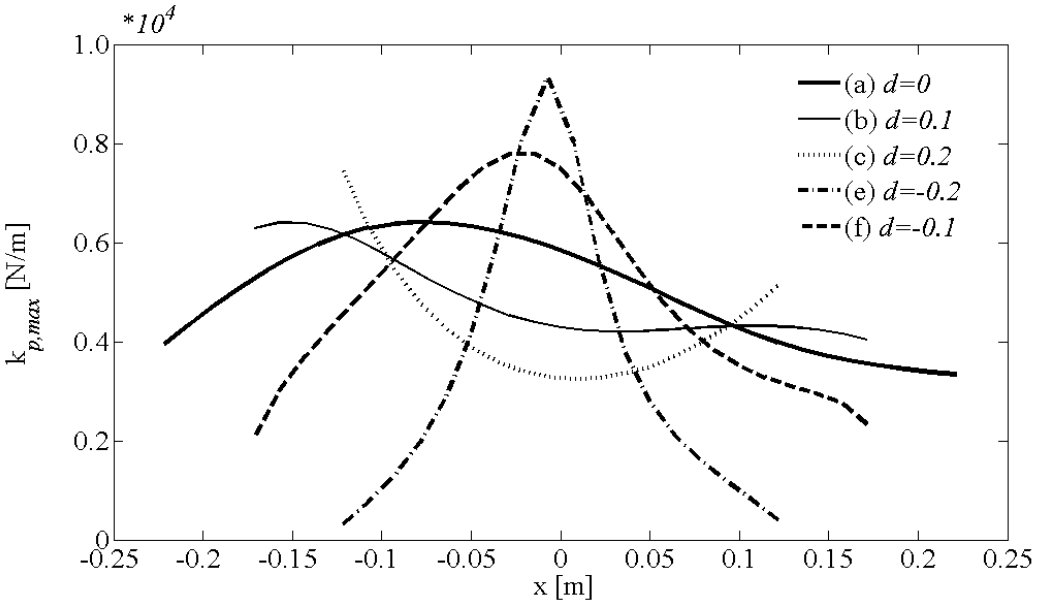

(b)

FIGURE 5.5. Maximum virtual stiffness, $k_{p,max}$, versus x for different values of parameter d, (a) rigid-body and (b) flexible model

shown in Fig. 5.5. For this purpose, values of $d = -0.2m$ to $d = 0.2m$ are considered. The sign of parameter d corresponds to the direction in which the axis of the driven joints are located with respect to each other (see Fig. 5.5(a)). For each case, the indices are determined at workspace points where -0.25 m $< x <$ 0.25 m with a fixed y-position at $y = 0.25m$. The configuration of the device corresponding to each selected value of parameter d is given on top of the fig. 5.5(a) for the case where the end-point is located at ($x = 0$ m, $y = 0.25$ m).

It should be indicated that for comparison reasons each curve is shifted by $d/2$ to the centre in the x direction. The range of $k_{p,max}$ in the rigid-body model is symmetric, while in the case of the flexible model is asymmetric. This is because the structural properties of the device also show an asymmetric character, as discussed in Chapter 3. This investigation shows that with the ability to change the operating configuration of the device, we are able to achieve different values for maximum renderable virtual stiffness, which can lead to different haptic performance in terms of impedance range. This can also affect the uniformity of the performance over the workspace. As can be seen, in both models, the case of $d = 0m$ provides the most uniform behaviour, but limited performance in terms of maximum renderable virtual stiffness. As the distance d increases, the uniformity in behaviour decreases. However, this can make it possible to achieve higher performance at certain locations in the workspace. In the case when $d = -0.2m$, the maximum virtual stiffness increases to three times of the minimum value that can be archived in this case. This clearly shows that the renderable virtual stiffness and the stability of the haptic interface can be considerably influenced by the reconfiguration of the device.

It should be noted that by the ability to change the parameter d, we are able to change the configuration of the device, while keeping the reference point in the workspace at the same location. To further investigate the effect of parameter d on the maximum renderable virtual stiffness, $k_{p,max}$, and the range of renderable virtual environment parameters, w_s, these indices are determined for a range of $-2m < d < 2m$ at a fixed end-point location in the workspace ($x = 0$ m, $y = 0.25$ m). The results

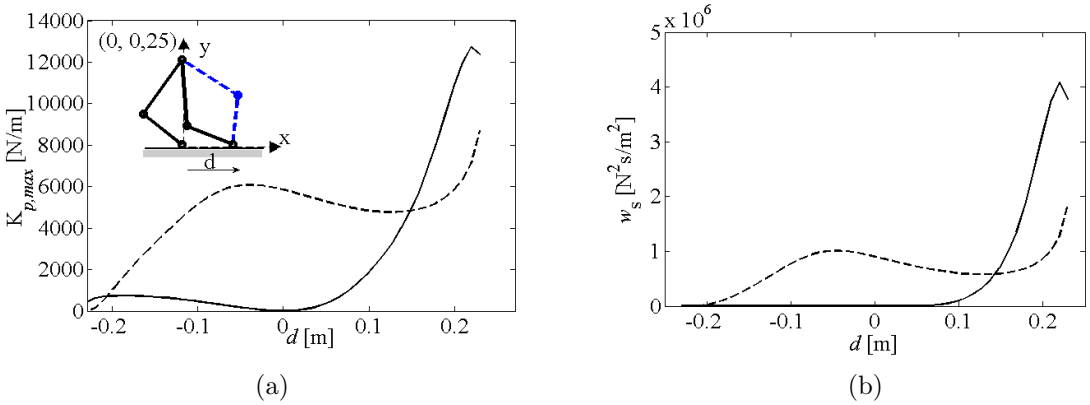

(a) (b)

FIGURE 5.6. Maximum virtual stiffness, $k_{p,max}$, (a) and range of stable virtual parameters, w_s, (b) versus parameter d, for the flexible model, elbow up (dash line) and elbow down (solid line)

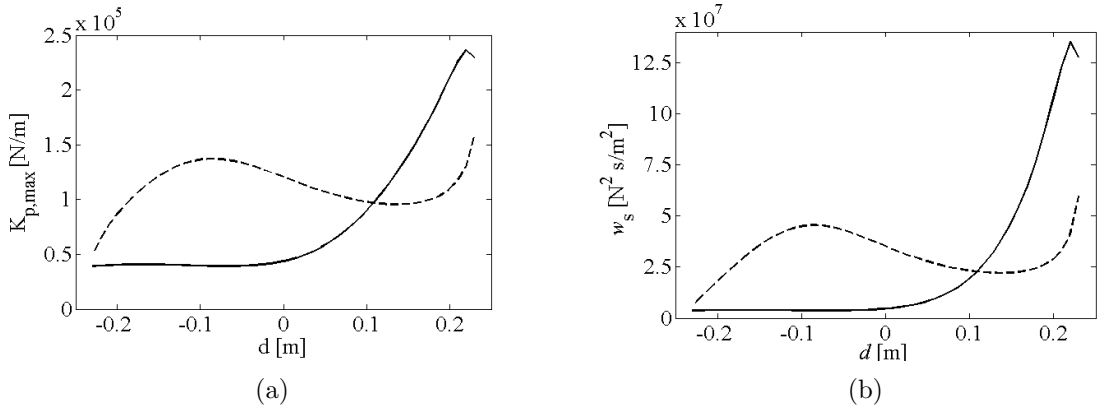

(a) (b)

FIGURE 5.7. Maximum virtual stiffness, $k_{p,max}$, (a) and range of stable virtual parameters, w_s, (b) versus parameter d, for rigid-body model, elbow up (dash line) and elbow down (solid line)

are shown in Fig. 5.6 and 5.7 for the flexible and rigid-body models, respectively. The solid and dashed lines indicate the elbow-down and elbow-up configurations as shown in 5.6(a). These figures show that the impedance range can be influenced considerably for different configurations of the device at the same operational position in the workspace.

As another example, the maximum virtual stiffness for both rigid and flexible models versus changes in length of the first link, L_1, are shown in Fig. 5.8. The five-bar linkage is shown in this figure for different values of parameter L_1, where the end-point

is located at the reference location in the workspace. It is interesting to mention that for the elbow-down configuration with the value of $L_1 = 0.146m$, which is equal to the current value of L_1 for the experimental device, the minimum value for virtual stiffness can be achieved. This indicates that the current design of the device provides the minimum renderable virtual stiffness. Therefore, for higher virtual stiffness, larger value of L_1 can be considered. It is important to note that changes in the inertia

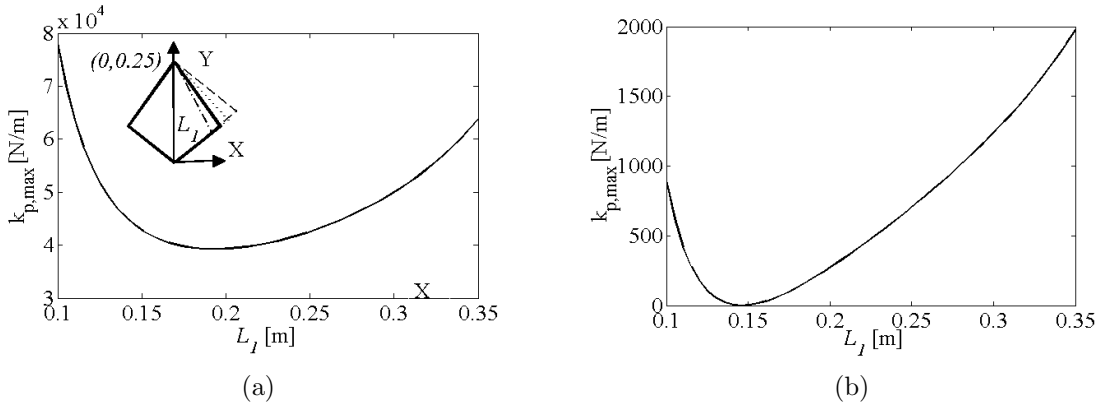

FIGURE 5.8. Maximum virtual stiffness, $k_{p,max}$, versus length of the first link of the device, L_1, for the rigid-body (a) and flexible model (b), in elbow down configuration

and flexility of the driving mechanism can have significant effect on the performance in applications where structural flexibility is considered. The dimensionless natural frequency Ω_n which is function of m_{e2}, k_e and Δt can represent these effects. Effects of the change of Ω_n on the dimensionless virtual stiffness is shown in Fig. 5.9(a). This figure shows that the maximum virtual stiffness can considerably change with respect to change of Ω_n. For more detailed investigation, the change of the driving mechanism parameters can also be studied by investigating the change in $k_{p,max}$ when one of the motor inertias, I_{m1} is modified. This is illustrated in Fig. 5.9(b).

5.3.2 Effects of Mechanical Design Parameters on the Fidelity. Another closed-loop performance measure proposed earlier was the optimum spectral radius to provide a tool for haptic rendering fidelity, and how mechanical design parameters can affect that. To illustrate this, we consider the two-DoF flexible model

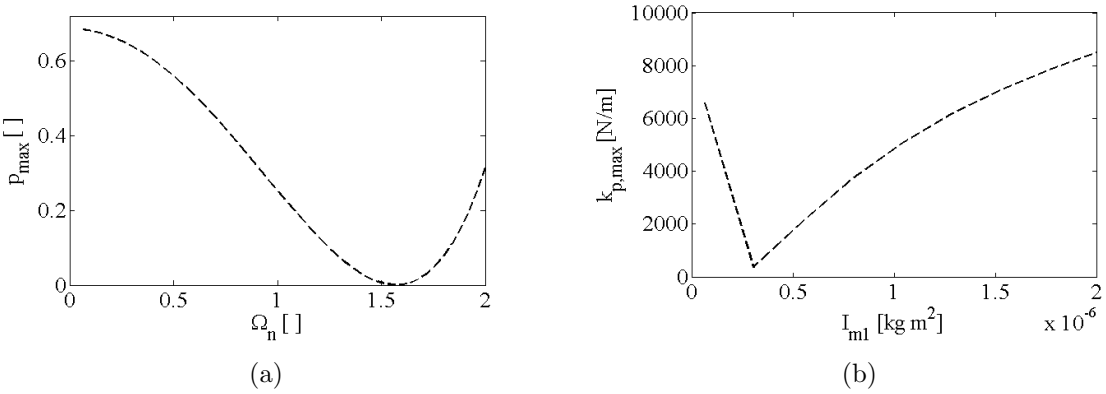

FIGURE 5.9. Maximum dimensionless virtual stiffness, p_{max}, versus dimensionless natural frequency, Ω_n, (a), and maximum virtual stiffness, $k_{p,max}$, versus motor inertia, I_{m1}, for flexible model in elbow up configuration

in (3.2). The behaviour of this model was studded in Chapter 3 and compared to experimental results (Fig. 3.1). Parameters of this model are listed in Table 3.4. The structural damping was modelled with the addition of 5% modal damping, and modal decomposition was used for the analysis. The analysis in Chapter 3 indicates that the stability of this model can be studied via a five dimensional discrete transition matrix. The resulting numerical and experimental stability charts are shown in Fig. 5.10, where the boundaries obtained using the model are shown by solid lines for different spectral radii, and the experimental measurement points along the stability boundary are shown by crosses (see also Chapter 3).

As described in Chapter 2, the eigenvalues of the transition matrix of the discrete mapping should lie within the unit circle in the complex plane. It is interesting to see how these eigenvalues change in the complex plane for different values of virtual stiffness and damping. As an example, we consider the stability boundary in Fig. 5.10. The trajectory of the eigenvalues in the complex plane associated with $k_p = 4000$ N/m are plotted in the right hand side of Fig. 5.10 for different values of k_d from the lower to the higher virtual damping range of this stability boundary. It can be seen from these trajectories that the eigenvalues leave the unit circle crossing the imaginary axis. This shows that by increasing virtual damping, for a fixed virtual stiffness, the system

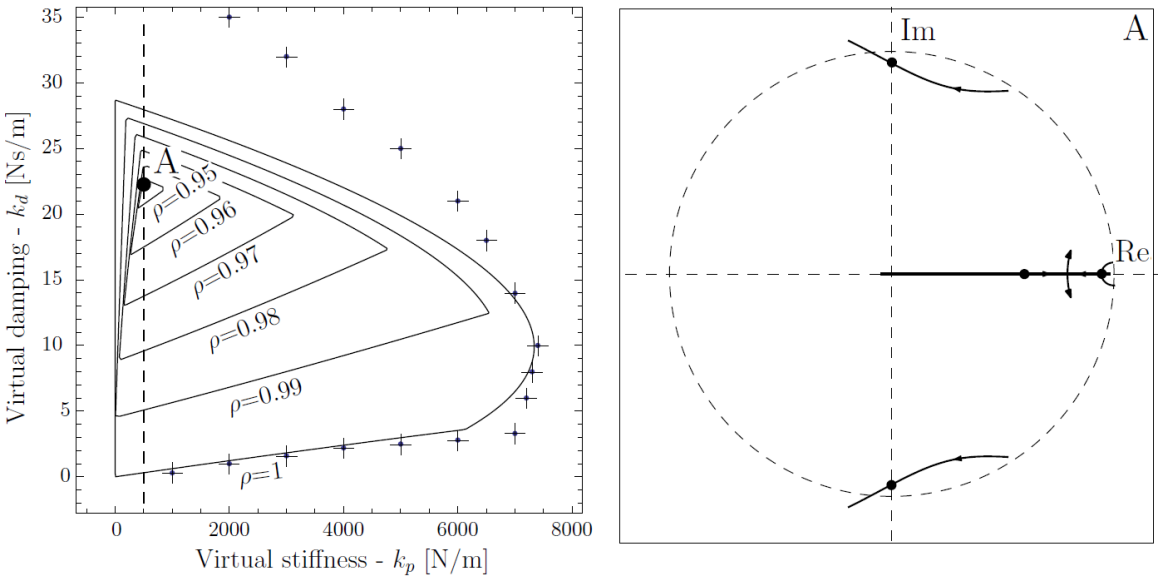

FIGURE 5.10. Left: Experimentally validated stability chart of the two-DoF flexible model with different spectral radii, Right: The eigenvalue trajectory in complex plane for $k_p = 4000$ N/m and $k_d \in [-2, 35]$

gets unstable when the complex eigenvalues with higher frequencies leave the unit circle. These high frequency eigenvalues mainly originated from the flexible elements characterized by the smaller effective mass m_{e2} in the model. The other eigenvalues remain inside the unite circle and experience very small changes for different virtual environment parameters.

For further analysis, the point associated with the optimal spectral radius is considered here, which is displayed as point A in Fig. 5.10. The five eigenvalues corresponding to this point are indicated by dots in the figure; where two of the real eigenvalues are collocated. The three eigenvalues on the real axis mainly characterize the dynamics of the rigid-body mode (characterized by m_{e1}). By looking at the stability domain corresponding to the rigid-body model in Fig. 3.9, it can be seen that point A is located well inside the stable domain of this model. This explains why the variation of parameter k_d has little effect on these three eigenvalues, and the system loses its stability due to oscillations originating from the effects of the smaller effective mass m_{e2}. This also illustrates the usability of the single-DoF flexible model in (2.44) that contains only the smaller effective mass m_{e2}.

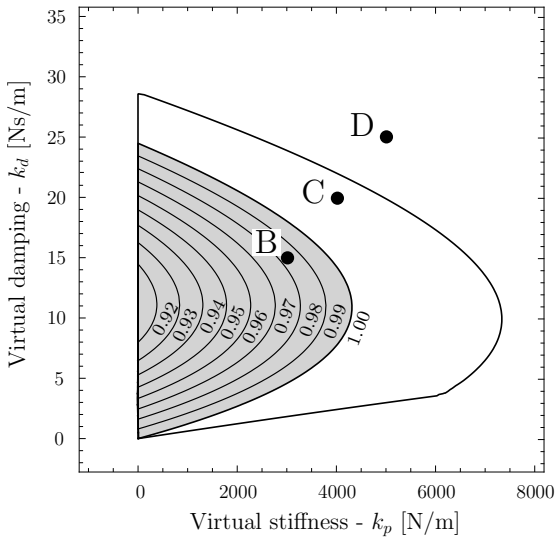

FIGURE 5.11. Stability charts corresponding to the two-DoF flexible model (white area) and the single-DoF flexible model (gray area) with different spectral radii

Stability analysis of the single-DoF flexible model was studied in detail in Chapter 4. The boundaries corresponding to this model for different spectral radii are shown in Fig. 5.11 together with the stability domain of the two-DoF flexible model with white and gray domains, respectively. Here points B, C and D are selected for further analysis. Point B, where $k_p = 3000$ N/m and $k_d = 15$ Ns/m, is located inside both stability boundaries. The associated eigenvalue trajectories at this point for different values of smaller effective mass, m_{e2}, are shown in Fig. 5.12 for the two-DoF and single-DoF flexible models by solid and dashed lines, respectively.

For further investigation, the behaviour of the two-DoF flexible model is simulated, considering the values of virtual stiffness and damping corresponding to point B. The resulting behaviour of this model in terms of $(x_1 - x_2)$ is shown in the right hand side of Fig. 5.12 by the thin solid line. The variable $(x_1 - x_2)$ corresponds to the superimposed vibrations, which can have important influence on the fidelity of haptic rendering. The goal here is to decrease the high frequency content in the feedback force. This can be achieved for example by considering the smaller effective mass, m_{e2}, as a design variable, and changing the mechanical properties of the system such that the high frequency oscillations dampen out as fast as possible. For this purpose,

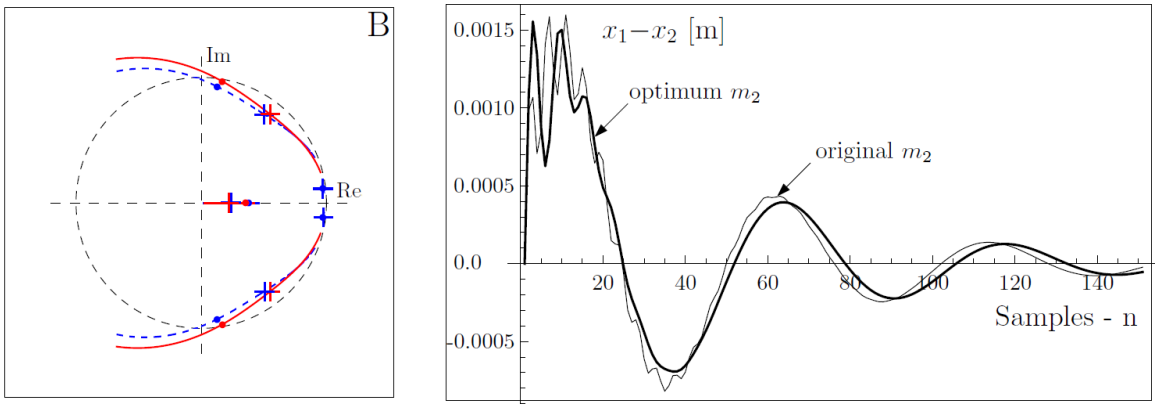

FIGURE 5.12. Left: Eigenvalue trajectories of the two-Dof flexible model (dashed line) and the single-DoF flexible model (solid line) at $k_p = 3000$ N/m, $k_d = 15$ Ns/m, Right: Simulation of the dynamics behaviour associated with the original and optimized values of m_{e2}

in this case the minimum spectral radius can be obtained by (5.15) as $\rho_{opt} = 0.8729$. This can be substituted in (5.14), which results in the optimum effective mass as $m_{e2,opt} = 0.0603$ kg. The corresponding eigenvalues are shown with crosses in the complex plane in the left hand side of Fig. 5.12. The resulting dynamic behaviour of the system with $m_{e2,opt}$ is shown by the thick solid line in Fig. 5.12. It can be seen that the system response becomes smoother and the vibrations due to structural flexibility decay much faster.

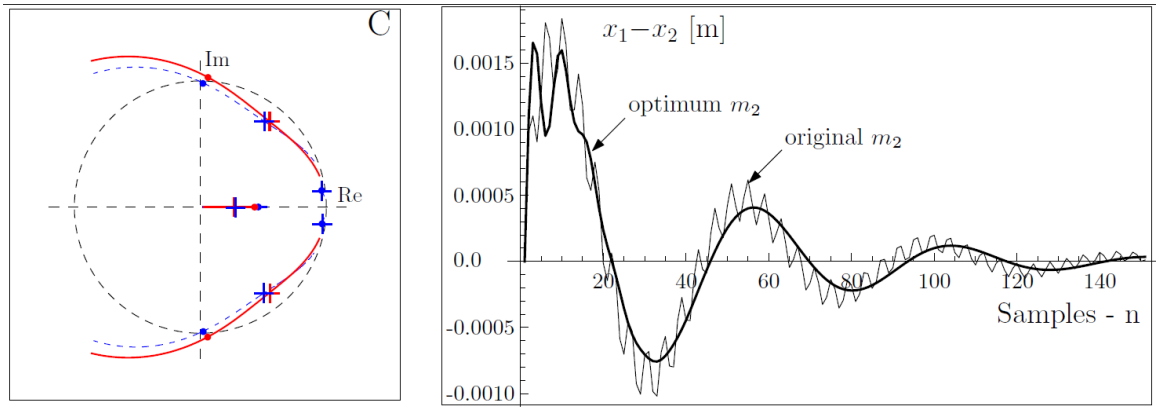

FIGURE 5.13. Left: Eigenvalue trajectories of the two-Dof flexible model (dashed line) and the single DoF flexible model (solid line) at $k_p = 4000$ N/m, $k_d = 20$ Ns/m, Right: Simulation of the dynamics behaviour associated with the original and optimized values of m_{e2}

The same analysis is repeated for the virtual stiffness and damping values at points C (k_p=4000 N/m, k_d=20 Ns/m) and D (k_p=5000 N/m, k_d=25 Ns/m) (see Fig. 5.11). Point C is located outside of the stability domain of the single-DoF flexible model, and Point D is outside of the stability domains corresponding to both models. The optimum effective masse and spectral radius are obtained as $m_{e2,opt}$=0.0510 kg and ρ_{opt} = 0.8956 for the parameters at point C, and $m_{e2,opt}$=0.1315 kg and ρ_{opt} = 0.71627 for point D.

The eigenvalue trajectory in the complex plane and the behaviour of the model with the original and optimum smaller effective mass are shown in Fig. 5.13 for virtual parameters at point C. It can be seen that the high frequency vibrations associated with the smaller effective mass, m_{e2}, decays in case of optimum m_{e2}, and the behaviour of the system improves considerably.

The result of the analysis corresponding to parameters at point D is shown in Fig. 5.14. The dynamic behaviour of the system with the original parameters in this case is unstable and is not shown in this figure. For such a set of virtual parameters, in order to make the system stable, the smaller effective mass of the system m_{e2} must be increased. It can be seen in Fig. 5.14 that the system with optimum parameters becomes stable and the oscillations decay much faster than the other two cases at points B and C. This is because point D is located outside of the stable domains, and the parameters of the system have to be changed more than in the other two cases (points B and D). The previously unstable point D is now moved to well inside the stable domain due to the change in mechanical system parameters. Therefore, the resulting stability chart of the system with the optimum effective mass, $m_{2,opt}$, becomes much larger. In this case point D is located well inside the stability domain corresponding to the optimum parameters of the system.

These analyses show that an optimum selection of mechanical design parameters of haptic systems can significantly influence the closed-loop performance of these systems.

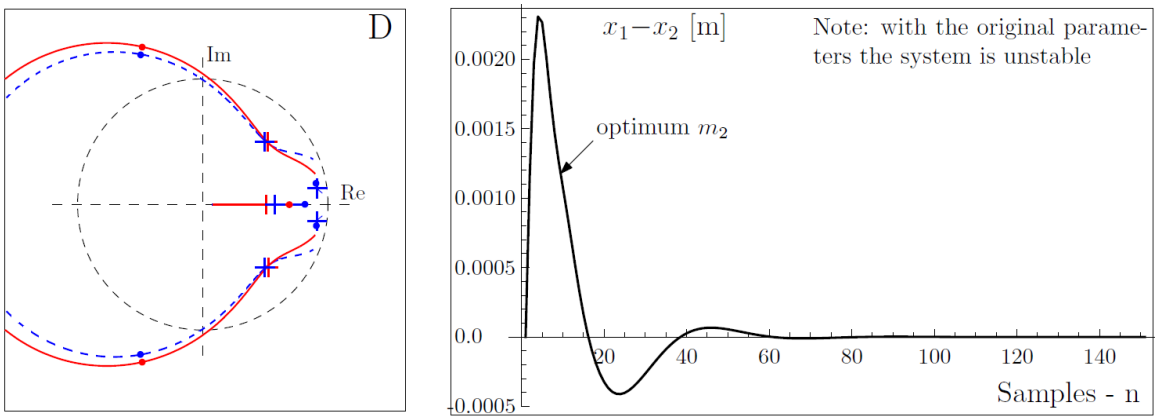

FIGURE 5.14. Left: Eigenvalue trajectories of the two-Dof flexible model (dashed line) and the single-DoF flexible model (solid line) at $k_p = 5000$ N/m, $k_d = 25$ Ns/m, Right: Simulation of the dynamics behaviour associated with the original and optimized values of m_{e2}

CHAPTER 6

Conclusions and Recommendations for Future Research

Haptic systems can exhibit complex dynamics behaviours due to the coupling of the physical and virtual domains. This thesis particularly investigated the effects of mechanical systems on haptic dynamics. A general model formulation was developed in Chapter 2 considering multi-degrees of freedom representation for the system consisting of the articulated haptic device and the human operator. The concept of haptic equilibrium was introduced to develop simplified, linearized models to reflect the aforementioned effects of mechanical system dynamics. Two types of models are considered primarily. In the first, the haptic device was considered as an articulated system of rigid bodies; while in the second type the structural flexibility was also taken into account. It was shown that in both cases, if the operator primarily develops forces/moments associated with the virtual interaction inrection, the rendered directions, then the entire system behaviour can be governed by the dynamics of the subspace defined by the rendered directions. An important point of the formulation is the decomposition of the dynamics of the system into the rendered and admissible subspaces. In the case of a single rendered direction, this analysis resulted in the derivation of a single-DoF model in the case of the rigid-body representation, and a

two-DoF model if the structural flexibility is considered. Effective parameters of these models were derived as analytical functions of the mechanical system parameters.

The simplified flexible model was developed via two effective generalized inertia representations connected with an effective stiffness of the system. This model can be further simplified to a single-DoF flexible model, in case when the characteristic vibrations of the system at high virtual wall impedances is primarily influenced by the inertia of the flexible parts of the device and the structural properties.

The usability of these models in haptic applications was investigated in Chapter 3 using a five-bar linkage based haptic device. In this chapter, the behaviour of the experimental haptic device was compared with those achieved using the proposed models. Two types of experiments were carried out; the first type was without the human operator's sustained touch, and the second type was when the human operator holds the reference element of the device and develops sustained interaction with the virtual environment. In the first set of experiments, it was shown that for the case of single rendered direction, the two-DoF flexible model appeared to represent well the stability behaviour for a broad range of the virtual environment parameters. However, it was illustrated that in the case of incorporating filters, the single-DoF rigid-body model can represent well the stability behaviour in the entire domain of virtual environment parameters. As a result of this investigation, it was shown that the space of virtual environment parameters can be divided into two regions. In each region, a different simplified single-DoF model of the haptic system can capture the characteristic dynamics.

The second set of experiments were conducted to study the effects of the human operator on haptic system dynamics. It was shown that the human operator is able to compensate for the unwanted dynamic effects, in the region of virtual environment parameters where rigid-body model is represented. However, when structural dynamics of the device has to be considered, dynamics of the human operator has small effect on stability of the haptic systems.

Both the analytical results and the experiments also confirm that structural flexibility can be the dominant factor to limit system stability, and can play a role more important than that of quantization in the development of oscillatory behaviours.

More detailed parametric analysis was conducted in Chapter 4 using the simplified models. Closed-form stability conditions were developed in this chapter. These extend the linear stability conditions that are commonly used in the literature. It was shown that in cases when the single-DoF rigid-body model with damping is representative, the maximum achievable virtual stiffness is limited by the physical and virtual damping, and the actuator saturation. However, in the presence of delays, such that can come from filtering, the maximum virtual stiffness is governed by the effective mass of the device associated with the rendered directions. To achieve high values of virtual stiffness and damping the structural properties of the mechanical system have to be considered. In those cases, the single-DoF model, derived based on considering structural flexibility and with damping, may be representative. If damping is neglected then the resulting single-DoF mass-spring model can provide a conservative basis for the design. In this case, the maximum renderable virtual stiffness can be quantified by the effective dimensionless natural frequency of the model.

This was then discussed in more detail in Chapter 5, where performance measures for the range of stable virtual environment parameters and for the fidelity of the virtual interaction force were developed. It was illustrated that mechanical system parameters can significantly influence both the range of renderable virtual environment parameters and the fidelity of the force feedback. It was shown that the design requirements for improving haptic performance do not necessarily satisfy the conditions for improving dexterity of the mechanism. Therefore, a compromise should normally be developed between these design requirements depending on the application.

6.1 Recommendations for Future Work

The focus of this thesis was to investigate effects of mechanical system parameters on virtual contact dynamics. However, dynamics of such systems can be influenced

by other factors such as the realization of the virtual environment. In this thesis the case of a virtual wall representation was considered. However, the analysis can be extended for more detailed virtual environment models.

In this thesis, the effect of computational delay was studied via considering a time-delay equal to an integer multiple of the sampling time in the virtual interaction force representation. However, more elaborated consideration of such effect can be important in the virtual contact dynamics.

In addition, more detailed investigation of the effects of the human operator dynamics on the virtual contact behaviour can provide more insight for improving the haptic performance.

In the development of parametric mechanical models for haptic systems, physical dissipation was approximated in this work by considering modal damping or linear viscous models. However, as was discussed in this thesis, the behaviour of a haptic system, and consequently the dissipation properties of the system can significantly change while interacting with virtual environments of low or high virtual stiffness and damping. This may require more elaborated dissipation models.

Closed-loop performance of haptic interfacing was quantified by considering the range of stable virtual impedance parameters. Also fidelity of the force feedback was represented by considering how fast the high-frequency oscillations of the system decay. These are only two examples for quantifying haptic performance. Other parametric performance measures may be developed using the proposed simplified models.

It was also discussed that the mechanical system parameters of a haptic device can have significant effects on haptic performance. Developing a design optimization algorithm for haptic applications can result in an optimum design for a haptic device before it is built.

BIBLIOGRAPHY

A. Frisoli, F. Simoncini, M. B. and Salsedo, F. (2007), 'Kinematic Design of a Two Contact Points Haptic Interface for the Thumb and Index Fingers of the Hand', *Journal of Mechanical Design* **129**(5), 520–529.

Adams, R. and Hannaford, B. (1999), 'Stable Haptic Interaction with Virtual Environments', *IEEE Transactions on Robotics and Automation* **15**(3), 465–473.

Adams, R. and Hannaford, B. (2002), 'Control Law Design for Haptic Interfaces to Virtual Reality', *IEEE Transactions on Control Systems Technology* **10**(1), 3 –13.

Adams, R. J., Moreyra, M. R. and Hannaford, B. (1998), Stability and performance of haptic displays: Theory and experiments, *in* 'Proceedings of the ASME International Mechanical Engineering Congress and Exhibition', pp. 27–34.

Angeles, J. (2012), *Dynamic Response of Linear Mechanical Systems: Modeling, Analysis and Simulation*, Springer.

Angeles, J. and Lopez-Cajun, C. (1992), 'Kinematic Isotropy and the Conditioning Index of Serial Robotic Manipulators', *International Journal of Robotics Research* **11**(6), 560–571.

Book, W. (1984), 'Recursive lagrangian dynamics of fexible manipulator arms', *The International Journal of Robotics Research* **3**(3), 87–101.

Borro, D., Savall, J., Amundarain, A., Gil, J., García-Alonso, A. and Matey, L. (2004), 'A large haptic device for aircraft engine maintainability', *IEEE Computer Graphics and Applications* **24**(6), 70–74.

Chang, K. and Khatib, O. (2000), Operational space dynamics: Efficient algorithms for modeling and control of branching mechanisms, *in* 'Proceedings of the International Conference on Robotics and Automation', pp. 850–856.

Cleghorn, W., Fenton, R. and Tabarrok, B. (1981), 'Finite element analysis of hign-speed flexible mechanisms', *Journal of Mechanism and Machine Theory* **16**(4), 407–424.

Colgate, J. and Brown, J. (1994), Factors affecting the Z-width of a haptic display, *in* 'Proceedings of the IEEE International Conference on Robotics and Automation, Oct. 28-30', pp. 3205–3210.

Colgate, J. and Schenkel, G. (1997), 'Passivity of a Class of Sampled-Data Systems: Application to Haptic Interfaces', *Journal of Robotic Systems* **14**(1), 37–47.

Diolaiti, N., Neimeyer, G., Barbagli, F. and Salisbury, J. K. (2006), 'Stability of Haptic Rendering: Discretization, Quantization, Time-delay and Coulomb Effects', *IEEE Transactions on Robotics* **22**(2), 256–268.

Ellis, R. E., Ismaeil, O. M. and Lipsett, M. G. (1996), 'Design and Evaluation of a High-Performance Haptic Interface', *Robotica* **14**, 321–327.

Faulring, E. L., Colgate, J. E. and Peshkin, M. A. (2006), 'The Cobotic Hand Controller: Design, Control and Performance of a Novel Haptic Display.', *International Journal of Robotic Research* **25**(11), 1099–1119.

Fu, M. and Cavusoglu, M. (2012), 'Human Arm-and-Hand Dynamic Model with Variability Analyses for a Stylus-Based Haptic Interface', *IEEE Transactions on Systems, Man, and Cybernetics* **42**(6), 1633–1644.

Gassert, R., Moser, R., Burdet, E. and Bleuler, H. (2006), 'Mri/Fmri-Compatible Robotic System with Force Feedback for Interaction with Human Motion', *IEEE/ASME Transactions on Mechatronics* **11**(2), 216 –224.

Gil, J., Avello, A., Rubio, A. and Florez, J. (2004), 'Stability Analysis of a 1DoF Haptic Interface Using the Routh-Hurwitz Criterion', *IEEE Transactions on Control Systems Technology* **12**(4), 583–588.

Gil, J., Avello, A., Rubio, A. and Florez, J. (2012), 'Mechanical Design Optimization for Multi-Finger Haptic Devices Applied to Virtual Grasping Manipulation', *Journal of Mechanical Engineering* **58**(7–8), 431–443.

Gil, J. and Diaz, I. (2010), 'Influence of Vibration Modes and Human Operator on the Stability of Haptic Rendering', *IEEE Transactions on Robotics* **26**(1), 160–165.

Gosline, A., Campion, G. and Hayward, V. (2006), On the use of eddy current brakes as tunable, fast turn-on viscous dampers for haptic rendering, *in* 'Proceedings of the the Eurohaptics Conference', pp. 229–234.

Gosselin, C. and Angeles, J. (1991), 'A Global Performance Index for the Kinematic Optimization of Robot Manipulators', *Transaction of the ASME, Journal of Mechanical Design* **113**, 220–226.

Greenwood, D. T. (2003), *Advanced Dynamics*, Cambridge University Press.

Haddadi, A. (2011), Stability, Performance, and Implementation Issues in Bilateral Teleoperation Control and Haptic Simulation Systems, PhD thesis, Queen's University Kingston (Canada).

Hannaford, B. and Ryu, J. H. (2002), 'Time-domain Passivity Control of Haptic Interfaces', *IEEE Transactions on Robotics and Automation* **18**(1), 1–10.

Haykin, S. (1970), *Active Network Theory*, Addison-Wesley.

Hayward, V. and Astley, O. R. (1996), Performance measures for haptic interfaces, *in* 'Proceedings of the Robotics Research: The 7th International Symposium, Oct. 28-30', pp. 195–207.

Hayward, V., Choksi, J., Lanvin, G. and Ramstein, C. (1994), Design and multi-objective optimization of a linkage for a haptic interface, *in* 'Proceedings of the International Symposium on Experimental Robotics', pp. 352–359.

Hogan, N. (1989), Controlling impedance at the man/machine interface, *in* 'Proceedings of the 1989 IEEE International Conference on Robotics and Automation', Vol. 3, pp. 1626–1631.

Hulin, T., Preusche, C. and Hirzinger, G. (2008), Stability boundary for haptic rendering: Influence of human operator, *in* 'Proceedings of the IEEE/RSJ International

Conference on Intelligent Robots and Systems, Oct. 28-30', pp. 3483–3488.

Ilic, D., Moix, T., Fracheboud, B., Bleuler, H. and Vecerina, M. (2005), A haptic interface for interventional radiology, *in* 'Proceedings of the 2005 IEEE International Conference on Robotics and Automation, April. 18-22', pp. 2933–2937.

Janabi-Sharifi, F., Hayward, V. and Chen, C.-S. J. (2000), 'Discrete-time Adaptive Windowing for Velocity Estimation', *IEEE Transactions on Control Systems Technology* **8**(6), 1003–1009.

Khan, S., ahmad, A. and Andersson, K. (2011), Design optimization of the tau haptic device, *in* 'Proceedings of the 3rd International Congress on Ultra Modern Telecommunications and Control Systems and Workshops', pp. 1–8.

Khatib, O. (1987), 'A Unified Approach for Motion and Force Control of Robot Manipulators: The Operational Space Formulation', *IEEE Journal of Robotics and Automation* **3**(1), 43–53.

Khatib, O. (1990), Motion/force redundancy of manipulators, *in* 'Proceedings of the 1990 Japan-USA Symposium on Flexible Automation - A Pacific Rim Conference', pp. 337–342.

Kovecses, J. (2008), 'Dynamics of Mechanical Systems and the Generalized Freebody Diagram, Part 1: General Formulation', *ASME Jornal of Applied Mechanics* **75**(6), 061012.

Kuo, B. (1981), *Digital Control systems*, SRL Publishing, Berlin.

Kurtz, R. and Hayward, V. (1992), Multiplegoal kinematic optimization of a parallel spherical mechanism with actuator redundancy, *in* 'Proceedings of IEEE International Conferene on Robotics and Automation', Vol. 8, pp. 644–651.

Luca, A. D. (1998), 'Decoupling and Feedback Linearization of Robots with Mixed Rigid/Elastic Joints', *International Journal of Robust and Nonlinear Control* **8**, 965–977.

M. Ueberle, N. M. and Buss, M. (2004), Vishard10, a novel hyperredundant haptic interface, *in* 'Proceedings of International Symposium on Haptic Interfaces for Virtual Environment and Teleoperator Systems', pp. 58–65.

Ma, O. and Angeles, J. (1993), Optimum design of manipulators under dynamic isotropy conditions, *in* 'Proceedings of the IEEE International Conference on Robotics and Automation', pp. 470–475.

Massie, T. and Salisbury, J. (1994), The phantomhaptic interface: A device for probing virtual objects, *in* 'Proceedings of the ASME Winter Annual Meeting: Dynamic Systems and Control', pp. 295–301.

McJunkin, S. T. (2007), Transparency improvement for haptic interfaces, PhD thesis.

Mehling, J., Colgate, J. and Peshkin, M. (2005), Increasing the impedance range of a haptic display by adding electrical damping, *in* 'Proceedings of the First Joint Eurohaptics Conference and Symposium on Haptic Interfaces for Virtual Environment and Teleoperator Systems', pp. 257–262.

Mendez, V. and Tavakoli, M. (2010), A passivity criterion for n-port multilateral haptic systems, *in* 'Proceedings of the 49th IEEE Conference on Decision and Control, Dec. 15-17', pp. 274–279.

Metzger, J.-C., Lambercy, O. and Gassert, R. (2012), High-fidelity rendering of virtual objects with the rehapticknob - novel avenues in robot-assisted rehabilitation of hand function, *in* 'Proceedings of the Haptics Symposium (HAPTICS), 2012 IEEE', pp. 51 –56.

Millman, P. and Colgate, E. (1991), Design of a four degree-of-freedom forcereflecting manipulandum with a specified force/torque workspace, *in* 'Proceedings of IEEE International Conferene on Robotics and Automation', Vol. 2, pp. 1488–1493.

Minsky, M. and Lederman, S. (1996), Simulated haptic textures: Roughness, *in* 'Proceedings of the ASME Dynamic Systems and Control Division', pp. 421–426.

Minsky, M., Ouh-young, M., Steele, O., Frederick P. Brooks, J. and Behensky, M. (1990), Feeling and seeing: issues in force display, *in* 'Proceedings of the 1990 Symposium on Interactive 3D Graphics', Vol. 24, pp. 235–243.

Moix, T. (2005), Mechatronic elements and haptic rendering for computer-assisted minimally invasive surgery training, PhD thesis.

Moreyra, M. and Hannaford, B. (1998), A practical measure of dynamic response of haptic devices, *in* 'Proceedings of the 1998 IEEE International Conference on Robotics and Automation Leuven', Vol. 1, pp. 369–374.

Okamura, A., Dennerlein, J. and Howe, R. (1998), Vibration feedback models for virtual environments, *in* 'Proceedings of the IEEE International Conference on Robotics and Automation', pp. 674–679.

Panait, L., Akkary, E., Bell, R. L., Roberts, K. E., Dudrick, S. J. and Duffy, A. J. (2009), 'The Role of Haptic Feedback in Laparoscopic Simulation Training', *Journal of Surgical Research* **156**(2), 312–316.

Papastavridis, J. G. (2002), *Analytical Mechanics*, Oxford University Press.

Peer, A. and Buss, M. (2008), 'A New Admittance-Type Haptic Interface for Bimanual Manipulations', *IEEE/ASME Transactions on Mechatronics* **13**(4).

Perez-Gonzalez, A., Vergara, M. and Sancho-Bru, J. (2013), 'Stiffness Map of the Grasping Contact Areas of the Human Hand', *Journal of Biomechanics* **46**, 2644–2650.

S. Li, A. Frisoli, M. S. and Bergamasco, M. (2010), Mechanical design and optimization of a novel fmri compatible haptic manipulator, *in* 'Proceedings of IEEE International Symposium on Robot and Human Interactive Communication', pp. 44–49.

Salcudean, S. E. and Stocco, L. (2000), Isotropy and actuator optimization in haptic interface design, *in* 'Proceedings of the IEEE International Conference on Robotics and Automation, Apr. 24-28', pp. 763–769.

Salisbury, C., Gillespie, R., Tan, H., Barbagli, F. and Salisbury, J. (2011), 'What You Cant Feel Wont Hurt You: Evaluating Haptic Hardware Using a Haptic Contrast Sensitivity Function', *IEEE Transactions on Haptics* **4**(2), 134–146.

Salisbury, J. and Craig, J. (1982), 'Articulated Hands: Force Control and Kinematic Issues', *International Journal of Robotics Research* **1**(1), 4–12.

Samur, E., Flaction, L. and Bleuler, H. (2011), 'Design and Evaluation of a Novel Haptic Interface for Endoscopic Simulation', *IEEE Transactions on Haptics* **5**(4), 301–311.

Siciliano, B. and Khatib, O. (2008), *Springer Handbook of Robotics*, Springer.

Speich, J., Shao, L. and Goldfarb, M. (2005), 'Modeling the Human Hand as It Interacts with a Telemanipulation System', *Mechatronics* **15**, 1127–1142.

Spong, M. (1987), 'Modeling and Control of Elastic Joint Robots', *Journal of Dynamic Systems, Measurement and Control* **109**, 310–319.

Stepan, G. (2001), 'Vibrations of machines subjected to digital force control', *International Journal of Solids and Structures* **38**(10–13), 2149–2159.

Stepan, G., Steven, A. and Maunder, L. (1990), 'Design principles of digitally controlled robots', *Mechanism and Machine Theory* **25**(6), 515–527.

Stocco, L. J. (2000), Robot design optimization with haptic interface applications, PhD thesis, The University of British Columbia (Canada).

Stocco, L., Salcudean, S. and Sassani, F. (1997), Mechanism design for global isotropy with applications to haptic interfaces, *in* 'Proceedings of the ASME Winter Annual Meeting (Dallas, Texas)', Vol. 61, pp. 115–122.

Stocco, L., Salcudean, S. and Sassani, F. (1998), 'Fast Constrained Global Minimax Optimization of Robot Parameters', *Robotica* **16**, 595–605.

Tavakoli, M. and Howe, R. (2007), The effect of joint elasticity on bilateral teleoperation, *in* 'Proceedingsof the 2007 IEEE/RSJ International Conference on Intelligent Robots and Systems (IROS 2007)', pp. 1618–1623.

Tavakoli, M. and Howe, R. D. (2008), Haptic implications of tool flexibility in surgical teleoperation, *in* 'Proceedings of the 2008 Haptics Symposium, March', pp. 377–378.

Tognetti, L. (2005), Improved Design and Performance of Haptic Two-Port Networks through Force Feedback and Passive Actuators, PhD thesis, School of Mechanical Engineering, Georgia Institute of Technology.

Tognetti, L. and Book, W. (2006), Effects of increased device dissipation on haptic two-port network performance, *in* 'Proceedings of the IEEE International Conference on Robotics and Automation', pp. 3304–3311.

Ueberle, M. and Buss, M. (2002), Design, control, and evaluation of a new 6 DoF haptic device, *in* 'Proceedings of the 2002 IEEE/RSJ International Conference on Intelligent Robots and Systems', pp. 2949–2954.

Ueberle, M. W. (2006), Design, control, and evaluation of a family of kinesthetic haptic interfaces, PhD thesis, Technische Universitat Munchen.

van der Linde, R., Lammerste, P., Frederiksen, E. and Ruiter, B. (2002), The haptic-master, a new high-performance haptic interface, *in* 'Proceedings of the Eurohaptics Conference', pp. 1–5.

Vlachos, K. and Papadopoulos, E. (2006), 'Transparency Maximization Methodology for Haptic Devices', *IEEE/ASME Transactions on Mechatronics* **11**(3), 249–255.

Vlachos, K., Papadopoulos, E. and Mitropoulos, D. N. (2004), Mass/inertia and joint friction minimization for a lowforce fivedof haptic device, *in* 'Proceedings of IEEE International Conferene on Robotics and Automation', Vol. 1, pp. 286–291.

Weir, D., Colgate, J. and Peshkin, M. (2008), Measuring and increasing z-width with active electrical damping, *in* 'Proceedings of the Haptic interfaces for virtual environment and teleoperator systems', pp. 169–175.

Willaert, B., Corteville, B., Bruyninckx, H., Brussel, H. V. and Poorten, E. V. (2010), Mechatronic design optimization of a teleoperation system based on bounded environment passivity, *in* 'Proceedings of the 2010 international conference on Haptics: generating and perceiving tangible sensations', pp. 161–168.

Yoshikawa, T. (1985), 'Manipulability of Robotic Mechanisms', *International Journal of Robotics Research* **4**, 3–9.

Zanganeh, K. and Angeles, J. (1997), 'The Optimum Design of Parallel Manipulators', *International Journal of Robotics Research* **6**(2), 185–197.

Zhang, X., Mills, J. and Cleghorn, W. (2007), 'Dynamic modeling and experimental validation of a 3-prr parallel manipulator with flexible intermediate links', *Journal of Intelligent Robot Systems* **50**, 323–340.

Zhu, G., Ge, S. and Lee, T. (1999), 'Simulation studies of tip tracking control of a single-link flexible robot based on a lumped model', *Robotica* **17**, 71–78.

APPENDIX A

Routh-Hurwitz Criterion

Suppose the characteristic equation of the nth order system is:

$$a_0 s^n + a_1 s^{n-1} + ... + a_{n-1} s + a_n = 0 \tag{A.1}$$

The Hurwitz determinant is:

$$\begin{vmatrix} a_1 & a_0 & 0 & 0 & 0 & 0 & \dots & 0 & 0 \\ a_3 & a_2 & a_1 & a_0 & 0 & 0 & ... & 0 & 0 \\ a_5 & a_4 & a_3 & a_2 & a_1 & a_0 & ... & 0 & 0 \\ \vdots & \vdots & \vdots & \vdots & \vdots & \vdots & \vdots & \vdots & \vdots \\ a_{2n-1} & a_{2n-2} & a_{2n-3} & \dots & \dots & \dots & \dots & a_{n+1} & a_n \end{vmatrix} \tag{A.2}$$

Here the coefficients with indices larger than n are taken zero. Similarly, the coefficients with negative indices are replaced with zero.

The conditions of the stability is that the n determinants formed from the principal minors of the Hurwitz determinant will be greater than zero. That is,

$$\Delta_1 = a_1 > 0 \quad \Delta_2 = \begin{vmatrix} a_1 & a_0 \\ a_3 & a_2 \end{vmatrix} > 0 \quad \Delta_3 = \begin{vmatrix} a_1 & a_0 & 0 \\ a_3 & a_2 & a_1 \\ a_5 & a_4 & a3 \end{vmatrix} > 0 \quad \dots (> 0) \tag{A.3}$$

APPENDIX B

Kinematic and Dynamic modelling of the Five-bar Linkage Based Haptic Device

B.1 Kinematic Analysis

The two-DoF planar haptic device in Fig. B.1 is based on a five-bar mechanism with two actuated DoF at the base.

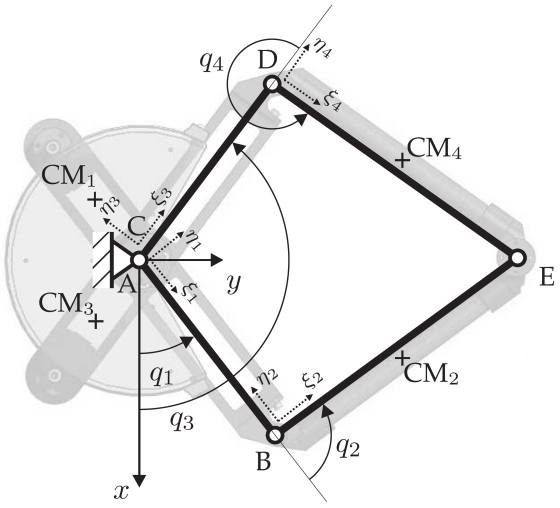

FIGURE B.1. Five-bar linkage, modelling of haptic device

By using the dependent set of relative joint coordinates, $\mathbf{q} = [q_1, q_2, q_3, q_4]^{\mathrm{T}}$, the tip position of the five-bar mechanism can be calculated via two chains E_1 formed by

Link 1 and 2, and and E_2 formed by Link 3 and 4. This position for chain E_1, can be written as

$$\begin{aligned} x_{E1} &= L_1 cos(q_1) + L_2 cos(q_1 + q_2) \\ y_{E1} &= L_1 sin(q_1) + L_2 sin(q_1 + q_2) \end{aligned} \tag{B.1}$$

and for chain E_2 as

$$\begin{aligned} x_{E2} &= L_3 cos(q_3) + L_4 cos(q_3 + q_4) \\ y_{E2} &= L_3 sin(q_3) + L_4 sin(q_3 + q_4) \end{aligned} \tag{B.2}$$

Considering time derivative of Eqs. (B.1) and (B.2), the corresponding Jacobians ($\dot{\mathbf{x}} = \mathbf{J}_1 \dot{\mathbf{q}}_{12}$ and $\dot{\mathbf{x}} = \mathbf{J}_2 \dot{\mathbf{q}}_{34}$) are defined as

$$\mathbf{J}_1 = \begin{bmatrix} -L_1 sin(q_1) - L_2 sin(q_1 + q_2) & -L_2 sin(q_1 + q_2) \\ L_1 cos(q_1) + L_2 cos(q_1 + q_2) & L_2 cos(q_1 + q_2) \end{bmatrix} \tag{B.3}$$

and

$$\mathbf{J}_2 = \begin{bmatrix} -L_3 sin(q_3) - L_4 sin(q_3 + q_4) & -L_4 sin(q_3 + q_4) \\ L_3 cos(q_3) + L_4 cos(q_3 + q_4) & L_4 cos(q_3 + q_4) \end{bmatrix} \tag{B.4}$$

where $\dot{\mathbf{q}}_{12} = [\dot{q}_1, \dot{q}_2]^{\mathrm{T}}$ and $\dot{\mathbf{q}}_{34} = [\dot{q}_3, \dot{q}_4]^{\mathrm{T}}$. The Minimum set of generalized coordinate can be defined as $\mathbf{p} = [q_1, q_3]$. The corresponding Jacobian ($\dot{\mathbf{x}} = \mathbf{J}\dot{\mathbf{p}}$), can be achieved by considering the constrained equation of the manipulator. The two constrained equations can be formed by considering $x_{E1} = x_{E2}$ and $y_{E1} = y_{E2}$, which results in

$$\begin{aligned} \Phi_1 &= L_1 cos(q_1) + L_2 cos(q_1 + q_2) - L_3 cos(q_3) - L_4 cos(q_3 + q_4) \\ \Phi_2 &= L_1 sin(q_1) + L_2 sin(q_1 + q_2) - L_3 sin(q_3) - L_4 sin(q_3 + q_4) \end{aligned} \tag{B.5}$$

and using these equations, the constrained Jacobian of the linkage can be obtained as

$$\mathbf{A} = \frac{\partial \Phi}{\partial q} = [\mathbf{J}_1 \ -\mathbf{J}_2] \tag{B.6}$$

Considering the constrained equations in (B.5) at the velocity level, one can obtain the minimum set Jacobian matrix as

$$\mathbf{J} = \frac{1}{sin(q_1+q_2+q_3+q_4)} \begin{bmatrix} -L_1 sin(q_2) sin(q_3+q_4) & L_3 sin(q_1+q_2) sin(q_4) \\ L_1 cos(q_3+q_4) sin(q_2) & -L_3 cos(q_1+q_2) sin(q_4) \end{bmatrix} \tag{B.7}$$

where q_2 and q_4 can also be replaced with the minimum set of coordinates as

$$\begin{aligned} q_2 &= asin(\frac{L_1}{L_2} sin(\frac{q_3-q_1}{2}) \\ q_4 &= 2\pi - (asin(\frac{L_1}{L_2} sin(\frac{q_3-q_1}{2}) + \frac{q_3-q_1}{2})) \end{aligned} \tag{B.8}$$

B.2 Inverse Displacement

The goal of the analysis here is to find the joint angles, given the end effector position and orientation. Consider the E_1 chain and the end point location in (B.1). These equations can be rearranged as

$$\begin{aligned} x_{E1} - L_1 cos(q_1) &= L_2 cos(q_1+q_2) \\ y_{E1} - L_1 sin(q_1) &= L_2 sin(q_1+q_2) \end{aligned} \tag{B.9}$$

where the sum of the square of both sides of these equations results in

$$x_{E1}^2 + y_{E1}^2 + L_1^2 - L_2^2 = 2x_{E1} L_1 \cos(q_1) + 2y_{E1} \sin(q_1) \tag{B.10}$$

Via trigonometric relations, this leads ro development of a quadratic equation as

$$a_2 t^2 + a_1 t + a_3 = 0 \tag{B.11}$$

where $t = \tan(\frac{q_1}{2})$, and

$$\begin{aligned} a_1 &= x_{E1}^2 + y_{E1}^2 + L_1^2 - L_2^2 + 2x_{E1} L_1 \\ a_2 &= -4y_{E1} L_1 \\ a_3 &= x_{E1}^2 + y_{E1}^2 + L_1^2 - L_2^2 - 2x_{E1} L_1 \end{aligned} \tag{B.12}$$

which results in derivation of $q_1 = 2\arctan(t)$, and by substituting it to (B.9), q_2 can be obtained. The same process can leads to derivation of q_3 and q_4. Note that the resulting joint angles are not unique.

B.3 Dynamic Analysis

Lagrange's equations of motion for the a minimum set of generalized coordinates, $\mathbf{p} = [q_1, q_3]^{\mathrm{T}}$, of the five-bar mechanism in Fig. 3.2 can be obtained as

$$\frac{d}{dt}(\frac{\partial L}{\partial \dot{p}_k}) - \frac{\partial L}{\partial p_k} = Q_k^{ppl,nc} \tag{B.13}$$

where $L = T_{total} - V_{total}$ is the Lagrangian, T and V are the total kinematic and potential energies of the system. The intension here is the dynamic analysis of the five-bar mechanism with rigid links and ideal joints. The plane of this mechanism is perpendicular to the filled of the gravity. Therefore, the potential energy is equal to zero, it means that the Lagrange function is equivalent with the kinetic energy ($L = T$). Due to symmetric geometry of the system, we consider half of the device to calculate the kinematic energy, where the total energy can be obtained as

$$T_{total} = T_1 + T_2 \tag{B.14}$$

while

$$\begin{aligned} T1 =& \frac{1}{2}(I_{CM1} + m_1 L_{CM1}^2 + m_2 L_1^2 + m_2 L_{CM2}^2 + 2m_2 L_1 L_{CM2}\cos(q_2) + \frac{1}{12}m_2 L_2^2)\dot{q}_1^2 \\ & \frac{1}{2}(m_2 L_{CM2}^2 + \frac{1}{12}m_2 L_2^2)\dot{q}_2^2 \\ & (m_2 L_{CM2}^2 + m_2 L_1 L_{CM2}\cos(q_2) + \frac{1}{12}m_2 L_2^2)\dot{q}_1\dot{q}_2 \end{aligned} \tag{B.15}$$

where I_{CM1} is the center of mass moment of inertia of the first link with the motor connected to it at one end, m_1, m_2 L_1, L_2, L_{CM1}, and L_{CM2} are the mass, length, and center of mass length of links 1 and 2. The kinetic energy corresponding to the second change composed of links 3 and 4 has the same structure. Considering the total

kinematic energy, the mass matrix of the systems can be achieved via $\mathbf{M} = \frac{d}{dt}(\frac{\partial T}{\partial \dot{p}_k})$. By introducing the notations $\cos(q_i) = c_i$ and $\sin(q_i) = s_i$ the 4×4 mass matrix corresponding to the non minimum set of generalized coordinates can be written in the block diagonal form

$$\mathbf{M} = \begin{bmatrix} \mathbf{M}_1 & \mathbf{0} \\ \mathbf{0} & \mathbf{M}_2 \end{bmatrix} \tag{B.16}$$

where

$\mathbf{M}_1 =$

$$\begin{bmatrix} I_{CM1} + m_1 L_{CM1}^2 + m_2(L_1^2 + L_{CM2}^2 + 2L_1 L_{CM2} & m_2(L_{CM2}^2 + L_1 L_{CM2} cos(q_2) + \frac{1}{12}L_2^2) \\ \cos(q_2) + \frac{1}{12}L_2^2) & \\ m_2(L_{CM2}^2 + L_1 L_{CM2} cos(q_2) + \frac{1}{12}L_2^2) & m_2(L_{CM2}^2 + \frac{1}{12}L_2^2) \end{bmatrix}$$

$\mathbf{M}_2 =$

$$\begin{bmatrix} I_{CM3} + m_3 L_{CM3}^2 + m_4(L_3^2 + L_{CM4}^2 + 2L_3 L_{CM4} & m_4(L_{CM4}^2 + L_3 L_{CM4} cos(q_4) + \frac{1}{12}L_4^2) \\ cos(q_4) + \frac{1}{12}L_4^2) & \\ m_4(L_{CM4}^2 + L_3 L_{CM4} cos(q_4) + \frac{1}{12}L_4^2) & m_4(L_{CM4}^2 + \frac{1}{12}L_4^2) \end{bmatrix}$$

And the nonlinear inertial term can be obtained as $\mathbf{c} = -\frac{\partial T}{\partial p_k}$ which results in

$$\mathbf{c}_2 = \begin{bmatrix} 0 \\ -2m_2 L_1 L_{CM2} \sin q_2 (\dot{q_1}(\dot{q_1} + \dot{q_2}) \\ 0 \\ -2m_4 L_3 L_{CM4} \sin q_4 (\dot{q_3}(\dot{q_3} + \dot{q_4}) \end{bmatrix} \tag{B.17}$$

The equations of motion in terms of minimum set of generalized coordinates can be obtained by the transformation $\dot{\mathbf{q}} = \mathbf{B}\dot{\mathbf{p}}$, while the transformation matrix $\mathbf{B}$ can be obtained as

$$\mathbf{B} = \begin{bmatrix} 1 & 0 \\ \frac{-L_1 sin(q_3+q_4-q_1)}{L_2 sin(q_3+q_4-q_1-q_2)} - 1 & \frac{L_3 sin(q_4)}{L_2 sin(q_3+q_4-q_1-q_2)} \\ 0 & 1 \\ \frac{-L_1 sin(q_2)}{L_4 sin(q_3+q_4-q_1-q_2)} & \frac{-L_3 sin(q_3-q_1-q_2)}{L_4 sin(q_3+q_4-q_1-q_2)} - 1 \end{bmatrix} \tag{B.18}$$

And the equation of motion in terms of the minimum set of coordinates can be obtained as

$$\mathbf{B}^T \mathbf{M} \mathbf{B} \ddot{\mathbf{p}} + \mathbf{B}^T (\mathbf{c} + \mathbf{M} \dot{\mathbf{B}} \dot{\mathbf{p}}) = \mathbf{B}^T \mathbf{Q} \tag{B.19}$$

Document Log:

Manuscript Version 0

Typeset by $\mathcal{AMS}$-LaTeX — 13 August 2014

Sara Shayan Amin

Centre for Intelligent Machines, McGill University, 3480 University St., Montreal (Québec), H3A 2A7, Canada

E-mail address: Sara@cim.mcgill.ca

Typeset by $\mathcal{AMS}$-LaTeX